



# **Oxoanion Adlayers on Au(111): an *in-situ* Scanning Tunneling Microscopy Study**

Dissertation

to obtain the academic degree

*Doctor rerum naturalium* (Dr. rer. nat.)

submitted to

The Faculty of Natural Sciences of Ulm University

by

Areeg Emam Mohamed Abdelrazek Abdelrahman

born in Yanbu, Saudi Arabia

2019











# **Oxoanion Adlayers on Au(111): an *in-situ* Scanning Tunneling Microscopy Study**

Dissertation

to obtain the academic degree

*Doctor rerum naturalium* (Dr. rer. nat.)

submitted to

The Faculty of Natural Sciences of Ulm University

by

Areeg Emam Mohamed Abdelrazek Abdelrahman

born in Yanbu, Saudi Arabia

2019

The experimental part of this work has been carried out in the period between October 2014 and July 2019, under the supervision of Prof. Dr. Timo Jacob, at the Institute of Electrochemistry of Ulm University.

Dean of the Faculty of Natural Sciences at Ulm University:  
Prof. Dr. Thorsten M. Bernhardt  
Institute of Surface Chemistry and Catalysis, Ulm University

First Reviewer:  
Prof. Dr. Timo Jacob  
Institute of Electrochemistry, Ulm University  
Helmholtz-Institute Ulm (HIU)

Second Reviewer:  
Prof. Dr. Carsten Streb  
Institute of Inorganic Chemistry I, Ulm University  
Helmholtz-Institute Ulm (HIU)

Third Reviewer:  
Prof. Dr. Peter Broekmann  
Department of Chemistry and Biochemistry  
University of Bern

Defence Date: 04.12.2019

## Declaration of Authorship

I hereby declare that I have written the present dissertation independently and without unauthorized external help. I have not used any sources or resources other than those indicated, and that any phrases taken from published or unpublished texts, as well as statements based on oral information, have been identified as such. All services and measurements provided by other persons have been marked and acknowledged.

Parts of the results in this dissertation have already been published in the following articles:

- [1] L. A. Kibler, J. M. Hermann, A. Abdelrahman, A. A. El-Aziz, T. Jacob, *Curr. Opin. Electrochem.* **2018**, *9*, 265–270. Permission not required according to Copyright Transfer Agreement.
- [2] A. Abdelrahman, J. M. Hermann, T. Jacob, L. A. Kibler, *ChemPhysChem* **2019**, *20*, 1–9. Permission aquired from John Wiley and Sons, Inc., ChemPhysChem.

Ulm,

Areeg Abdelrahman



# *Acknowledgements*

First and foremost, I am grateful to Almighty Allah (*Subhanahu wa Ta'ala*) for providing me with the strength and determination to complete my research. I would like to thank Him for His continuous blessings throughout my life and ever more during my research, without which I would have not been able to succeed.

This work would not be possible without the encouragement, support and blessings from a number of people. I take this opportunity to express my heartfelt appreciation and genuine gratitude to all of them. I am very much grateful to my advisor, Prof. Dr. Timo Jacob for giving me this opportunity and believing in my abilities, even though I have no chemistry background, to carry out my doctorate at the Institute of Electrochemistry in Ulm University. I would also like to express my deep and sincere gratitude to Dr. Ludwig Kibler for his guidance and stimulating discussions, which directed me throughout my research and decisively contributed to the successful completion of the present work. He has been a wonderful guide and a role model for the past five years.

I would also like to thank Prof. Dr. Carsten Streb for taking the time and effort to be my second supervisor and for revising this work.

To all the current and previous members of the institute, I would like to say thank you for the favourable working conditions and friendly atmosphere. I wish to extend my warmest thanks to all the *Mädels*, Layal, Svenja, Sabine, Martin and Annchristin who have been there during all the ups and downs. Thank you for the comforting warm hugs and endless reassuring talks. I would also like to thank Maximilian Eckl, for the positive atmosphere in the basement while we both measured for hours in the dark. Johannes M. Hermann deserves special thanks for his tireless assistance. His wide knowledge and his logical way of thinking have been of great value for me. His understanding, encouraging and personal guidance have provided a good basis for this work.

To all the friends I made here in Germany who became more-like family, I would like to thank you for all the unforgettable memories we had. Hany, Mona, Shawki, Youmna, Bakkar, Sherine, Omar, Karim and Salam, you supported me throughout this journey. We have been through a lot together and only you have made my stay abroad feel like home. I would also like to offer my sincerest gratitude to Auntie Dalia, for her untiring prayers which have undoubtedly meant so much to me and helped me throughout my difficult times.

Most importantly, I would like to thank my family. To my parents for their continuous help and support which has brought me where I am today. Mama and Baba, without you I would not have come this far. To my sister Hadeer, I am deeply thankful to you. Your untiring encouragement has helped me throughout my journey. No words can explain how much I am grateful to you. I owe my loving gratitude to my husband, best friend and colleague Yasser, for giving me untiring help during my difficult moments and for his continuous patience and understanding. Without his moral support, it would have been impossible for me to finish this work. I am so grateful for having you by my side.

اهداء إلى ماما وبابا





# Table of Contents

<b>Table of Contents</b>	<b>i</b>
<b>1 Introduction</b>	<b>1</b>
<b>2 Theoretical Background</b>	<b>5</b>
2.1 Single-crystal Electrodes .....	5
2.1.1 Structure of <i>fcc</i> (hkl) Surfaces.....	5
2.1.2 Surface Structure of Au(111) Electrodes.....	6
2.1.3 Surface Reconstruction of Au(111) Electrodes.....	7
2.1.4 Surface Defects.....	9
2.2 Adsorption of Ions on Metal Electrodes.....	11
2.2.1 The Metal-Electrolyte Interface .....	11
2.2.2 Fundamental Principles of Adsorption.....	13
2.2.3 Structures of Commensurate Adlayers on Single-crystal Surfaces .....	16
2.2.4 Adsorption of Sulfate on Au(111): The Benchmark.....	18
2.2.5 Adsorption of Other Oxoanions on Au(111) .....	21
2.2.6 Competitive Adsorption of Oxoanions for Formic Acid Oxidation.....	23
2.3 Scanning Tunneling Microscopy .....	24
2.3.1 Operating Principle of Scanning Tunneling Microscopy .....	24
2.3.2 <i>In-situ</i> Scanning Tunneling Microscopy .....	26
<b>3 Experimental Methods</b>	<b>29</b>
3.1 Cleaning Equipment and Cells.....	29
3.2 Gold Sample Preparation.....	30

3.3	Cyclic Voltammetry .....	32
3.4	<i>In-situ</i> Scanning Tunneling Microscopy .....	33
3.4.1	Instrumentation Set Up and Calibration .....	34
3.4.2	<i>In-situ</i> STM Cell .....	35
3.4.3	STM Tips Preparation .....	37
3.5	Materials and Chemicals.....	40
<b>4</b>	<b>Electrochemical Behaviour of Au(111) in 0.1 M H<sub>2</sub>SO<sub>4</sub>: New Insights</b>	<b>43</b>
4.1	Potential Dependence on Surface Reconstruction.....	43
4.2	Distinct Adsorbed Sulfate Structures (S-I, S-II and S-III) .....	46
<b>5</b>	<b>Adsorption of Carboxylates</b>	<b>51</b>
5.1	Au(111) in Acetic Acid .....	51
5.1.1	Electrochemical Behaviour .....	51
5.1.2	<i>In-situ</i> STM Imaging.....	53
5.1.3	Transition of Adsorbed Acetate Structures with Time .....	55
5.1.4	Acetate Structures A-I and A-II: STM Images and Proposed Models ....	57
5.2	Au(111) in Formic Acid.....	62
5.2.1	Electrochemical Behaviour .....	62
5.2.2	<i>In-situ</i> STM Imaging.....	64
5.2.3	Formate Structure F-I.....	65
5.2.4	Influence of the Presence of HClO <sub>4</sub> on the Adsorption of Formate .....	68
5.3	Acetate <i>vs.</i> Formate Adsorption .....	71
<b>6</b>	<b>Adsorption of Phosphate Oxoanions</b>	<b>73</b>
6.1	Au(111) in Sodium Phosphate Buffer Solutions .....	73
6.1.1	Electrochemical Behaviour .....	74
6.1.2	Potential Dependence on Phosphate Structure P-I.....	76
6.1.3	Phosphate Structure P-II .....	81
6.2	Au(111) in a Lithium Phosphate Buffer Solution .....	87
6.3	Influence of Alkali Metal Cations (K <sup>+</sup> , Na <sup>+</sup> and Li <sup>+</sup> ).....	90

<b>7</b>	<b>Conclusions and Outlook</b>	<b>91</b>
	<b>Bibliography</b>	<b>95</b>
	<b>List of Abbreviations</b>	<b>105</b>
	<b>List of Symbols</b>	<b>107</b>
	<b>List of Figures</b>	<b>109</b>
	<b>List of Tables</b>	<b>115</b>
	<b>Publications</b>	<b>117</b>
	<b>Curriculum Vitae</b>	<b>119</b>



# 1 Introduction

A major topic in the field of interfacial electrochemistry and electrocatalysis is the electrosorption of ions, particularly oxoanions on surfaces of noble metal electrodes.<sup>[1,2]</sup> The presence of adsorbed anions on a catalyst’s surface can strongly affect reaction kinetics, activity and selectivity.<sup>[3-6]</sup> Adsorption processes strongly depend on the structure and the chemical nature of the electrode surfaces’ basal planes. Well-ordered model systems, particularly single-crystal electrode surfaces, have been efficiently established to study processes of adsorption at a fundamental level.<sup>[1,7-10]</sup> Electrocatalytic reactions are often affected by the presence of nonreactive specifically adsorbed anions (spectator species), resulting in changes in the composition and structure of the electrical double-layer and altering the electronic properties of a catalyst’s surface. On the one hand, electrosorbed anions can promote reactions by directly participating in the reaction or by stabilizing its reaction intermediates.<sup>[11-13]</sup> On the other hand, the coadsorption of ions can provoke an inhibiting effect on an electrocatalytic process by blocking active surface sites.<sup>[4,14,15]</sup> Therefore, studying the electrochemical behaviour of adlayers of adsorbed anionic species at the metal-electrolyte interface can help to understand reaction conditions and hence the overall electrocatalytic activity of a certain reaction.<sup>[16,17]</sup>

An important aspect in electrocatalysis is identifying relationships between the microscopic properties of adsorbed reactants and intermediates and the macroscopic kinetic rates of electrochemical reactions.<sup>[18,19]</sup> This knowledge may help to create tailor-made surfaces with the microscopic structure required to achieve the desired catalytic properties.<sup>[12]</sup> *In-situ* microscopic imaging of ordered structures helps reveal the structural properties of adlayers on surface on an atomic level in real space, to compare with results from macroscopic techniques. Considerable progress has been made in studying ordered adlayer structures of oxoanions on electrode surfaces on an atomic scale using *in-situ* scanning tunneling microscopy (STM).<sup>[1,3,7-9,20-23]</sup> The Au(111) in H<sub>2</sub>SO<sub>4</sub> system has been used as a benchmark for years to identify key surface processes, to determine the quality

of a single-crystal electrode surface and, to understand the fundamentals of adsorption on electrified metallic surfaces.<sup>[8,10,24–27]</sup> One of the first accomplishments of the *in-situ* STM imaging of this system was observing the reconstructed and unreconstructed Au(111) surface.<sup>[9,28]</sup> Nonetheless, kinetic studies on the formation of reconstruction lines in the double-layer region remain scarce.<sup>[29–32]</sup> This is most likely due to the fact that, for studies where the electrochemical behaviour depends on the surface structure, it is commonly argued that limited information can be provided using STM since only an infinitesimal part of the surface is probed. In this work, the progress of changes in the surface structure of the model Au(111) system, as a function of potential, is monitored using *in-situ* STM and a structure-sensitive electrocatalytic reaction (HER). Compared to the kinetics of surface reconstruction, the phase transition within the adsorbed sulfate layer on the Au(111) surface is extensively studied using a number of *in-situ* techniques, however, the nature of the adsorbed species at the Au(111)/0.1 M H<sub>2</sub>SO<sub>4</sub> interface has been a matter of strong debate for years.<sup>[7,8,33–37]</sup>

It is remarkable that only a few studies are found on the adsorption of two-oxygen oxoanions,<sup>[38–40]</sup> in contrast to those found for three- and for four-oxygen oxoanions.<sup>[8,9,20,41–43]</sup> Formate and acetate represent examples of simple carboxylates which are a major group of molecular species that strongly adsorb on catalytically active noble metal surfaces and can therefore influence electrocatalytic reactions.<sup>[4,44–46]</sup> In the case of a model electrocatalytic system such as formic acid oxidation, adsorption plays a major role on oxidation kinetics. Strongly bound formate, HCOO<sub>ad</sub>, in the bidentate configuration was observed to act as an intermediate (spectator species) in the indirect mechanism pathway where it can easily block active sites of a Au(111) surface.<sup>[47–50]</sup> A structure of parallel chains has recently been imaged for HCOO<sub>ad</sub> on Au(111) in the potential region where the electrooxidation of formic acid/formate takes place.<sup>[50]</sup> Adsorption studies of formate on gold surfaces are however, hampered by its electrocatalytic reaction<sup>[50]</sup> since both the strong adsorption and the electrooxidation of formate, in a stable and reactive configuration, respectively, occur simultaneously. Such conditions make it extremely challenging to image formate adlayers by *in-situ* STM.

Unlike formate, acetate is unreactive on gold.<sup>[51]</sup> Nonetheless, similar to formate, acetate can influence electrocatalytic reactions. By blocking active sites and by inhibiting the formation of key intermediates, acetate suppresses catalytic reactions such as the oxidation of ethanol and the reduction of molecular oxygen.<sup>[45]</sup> In addition, a blocking effect of formic acid oxidation with increasing acetic acid concentration has also been

identified for a Au(111) electrode in mixtures of formic and acetic acid.<sup>[52]</sup> This is a strong indication for the possible coadsorption of acetate and formate. Since acetate and formate are alike in terms of geometry, similar adsorption behaviour is expected. More specifically, that acetate would also form parallel chains of an ordered structure where it adsorbs through the two oxygen atoms of the carboxylate group in a bidentate configuration.<sup>[47,50,51,53-55]</sup> However, the specific adsorption site for the acetate adsorbate cannot be determined from spectroscopic data. The study of other simple carboxylates with similar geometries to formate, such as acetate, is therefore ideal to determine whether the formation of an ordered structure on metallic surfaces is unique for formate or a characteristic feature for carboxylates. In addition, more insight on formate adsorption can be acquired to help aid in the *in-situ* imaging of a structure.

Very few surface science studies have compared the adsorption of sulfate to another oxoanion of similar size and geometry, such as phosphate, for example. Phosphate buffers are commonly used to control the solution pH in both chemical and electrochemical systems.<sup>[56-62]</sup> They are especially essential for electrocatalysis which involves proton-coupled electron transfer. Recent studies have shown that the specific adsorption of phosphate anions at metal surfaces influences electrocatalysis.<sup>[5,63,64]</sup> Particularly important for this study is the blocking effect which has been observed for the electrocatalytic oxidation of formic acid due to adsorption of phosphate anions.<sup>[5,63]</sup> Using several techniques, efforts have been made to help understand the adsorption of phosphate at the electrochemical interface.<sup>[20,65-70]</sup> Nonetheless, due to the polyprotic nature of phosphate species,<sup>[71]</sup> the geometry and state of adsorbed phosphate remains till this day a matter of great debate.

Nowadays, most STM adsorption studies on noble and non-noble metal surface are performed under ultra-high vacuum (UHV) conditions.<sup>[38-40,72-75]</sup> Under electrochemical conditions however, the interactions between surface atoms are altered.<sup>[76]</sup> The potential of the electrode controls the surface's excess charge thus affecting the surface coverage and structural order of adsorbents. Therefore, *in-situ* STM is a powerful technique to locally characterize metallic surfaces and visualize adsorbed structures on an electrified interface at atomic scale, which is not possible with other spectroscopic techniques. This is achieved by determining the size and arrangement of molecules on the surface as well as the lattice parameters of the ordered structures that they form.

Gold single-crystal surfaces are of fundamental interest in many fields of electrochemistry<sup>[77,78]</sup> because they are (i) structurally well-defined, (ii) clean and easy to

prepare,<sup>[77]</sup> (iii) stable, have a large double-layer region and due to their noble character, are not attacked by either air or acid. Gold can only be dissolved by strongly oxidizing acids (*e.g.* aqua regia) or by complexing agents.<sup>[79]</sup> Unlike platinum, gold surfaces are not poisoned during the electrooxidation of formic acid, making them primary candidates from the fundamental understanding of formate adsorption on an electrified interface. Among the different single-crystal surfaces of Au, the densely packed (111) orientation is the most fundamentally investigated and shows the highest activity of formic acid oxidation, for example.

The aim of this work is to investigate the adsorption of formate at a molecular level under electrochemical conditions. Before doing so however, high-resolution *in-situ* STM images of the well-established Au(111) in 0.1 M H<sub>2</sub>SO<sub>4</sub> system should first be acquired to ensure the possibility of studying a more complicated system. Interestingly, during those measurements, new findings into the potential dependence on the kinetics of surface reconstruction and into the adsorbed sulfate structure were observed. Next, since acetate compared to formate, is not active on the Au(111) surface, the adsorption of acetate will first be studied to help gain more insight on formate adsorption. Both findings will later be compared to one another. Finally, the adsorption of phosphate anions will be investigated as an example of a four-oxygen oxoanion which strongly blocks formic acid oxidation at higher pH values. In the course of phosphate adsorption study, insight into the impact of the coadsorption of additional spectator species like alkali metal cations (K<sup>+</sup>, Na<sup>+</sup>, Li<sup>+</sup>), which are widely used components of supporting electrolytes, will be given. Cyclic voltammetry is preliminarily used to characterize an electrochemical system.<sup>[80-82]</sup> With the help of this method, it is possible to acquire information about electrochemical processes and to determine the potentials at which they occur. Cyclic voltammetry and *in-situ* STM are used to characterize the configuration and bonding of sulfate, phosphate, acetate and formate anions to a Au(111) substrate.



## 2 Theoretical Background

### 2.1 Single-crystal Electrodes

One of the main goals in surface science is to identify relations between the surface structure of an electrode and certain electrochemical reactions, examples are the deposition of metal, the adsorption of ions, atoms or molecules, and the oxidation of organic molecules.<sup>[1,83-86]</sup> For such studies, single-crystal surfaces rather than polycrystalline surfaces are used as electrode substrates. Due to the well-defined periodic arrangement of metal atoms in a single-crystal, the influence of the substrate geometry on an adsorbate adlayer can more easily be investigated.<sup>[77]</sup> In this work, studies on a gold single-crystal electrode with the densely packed (111) orientation are carried out. Therefore, a fundamental understanding of its surface structure is necessary and will be explained in detail below.

#### 2.1.1 Structure of *fcc*(hkl) Surfaces

A single-crystal is made of a small symmetric repeating unit known as the unit cell. The unit cell completely defines the symmetry and structure of the crystal lattice structure. The gold electrode used in this work crystallizes in a face-centred-cubic (*fcc*) lattice, with its corresponding unit cell schematically shown in Figure 2.1a. It consists of 4 atoms, with each atom surrounded by 12 nearest neighbours (coordination number = 12).<sup>[79]</sup> The three lattice vectors have the same length, and their angles are all 90°.<sup>[87,88]</sup> The crystal lattice is built up by the repetitive translation of the unit cell along its principal axes as shown in Figure 2.1b.

By cutting the crystal along different directions and depending on the angles of intersection with unit cell's axes, different crystal planes with specific crystallographic orientation can be generated. The orientation of the planes of a single-crystal are usually represented by Miller indices (hkl).<sup>[87,88]</sup> The (hkl) values are obtained by taking the

reciprocal of the intercepts of a certain plane with the lattice vectors of the unit cell (namely the x-, y- and z-axes). By convention, smallest possible integers are used.

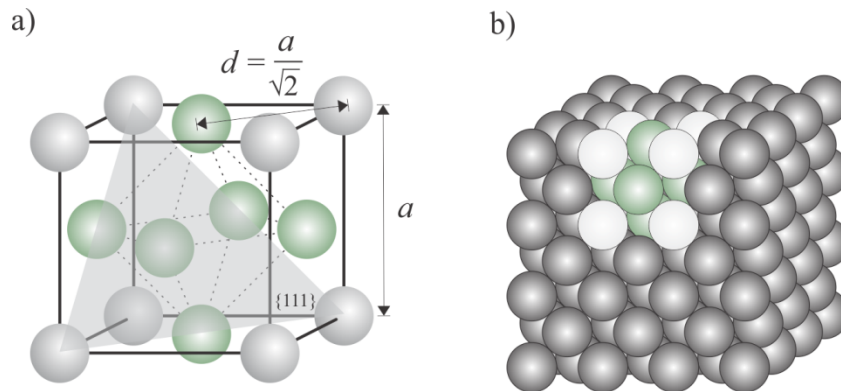


**Figure 2.1:** (a) Unit cell of with a face-centred-cubic (*fcc*) lattice. (b) Single-crystal model of an *fcc*(*hkl*) metal.

### 2.1.2 Surface Structure of Au(111) Electrodes

The (111) plane of a gold single-crystal is achieved by slicing the unit cell along its spatial diagonal at the three vertices. This results in a close packed hexagonal arrangement of surface atoms as depicted in Figure 2.2a.<sup>[89]</sup>

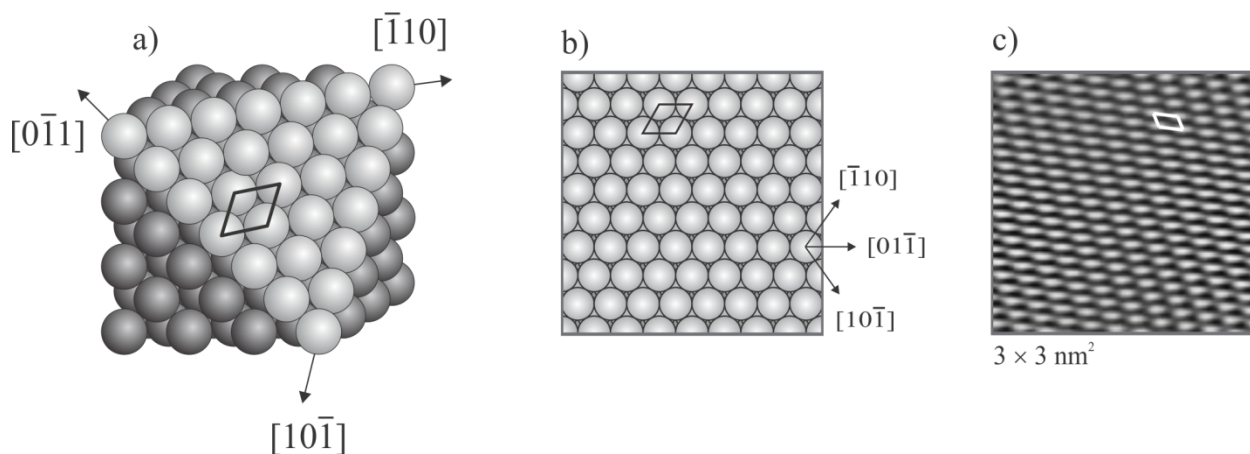


**Figure 2.2:** Model of a single-crystal with an *fcc* lattice, based on<sup>[90]</sup> (a) highlighting the {111} plane. (b) Plane view of the {111} plane along with its base vectors. (c) STM image of a Au(111)-(1×1) unreconstructed surface.

The rhombus drawn in Figure 2.2b, represents the unit cell of the gold surface atoms, having an interatomic distance of  $2.89 \text{ \AA}$ <sup>[91]</sup> and an enclosing angle (between the unit vectors) of  $60^\circ$ .<sup>[88]</sup> The lattice constant for the Au(111) surface is  $4.08 \text{ \AA}$ .<sup>[91]</sup> Figure 2.2c shows an STM image of the surface structure of a Au(111) electrode, where the interatomic distance is  $2.8 \pm 0.2 \text{ \AA}$ . The arrangement of the surface atoms in this figure is known as a  $(1 \times 1)$ -structure, which will later be used to describe structures of adsorbed adlayers on the electrified Au(111) surface. In addition, the vectors shown in Figure 2.2b, which are derived from the crystal volume,<sup>[92]</sup> will be used to describe respective surface structures. These vectors play a major role in discussing the surface reconstruction phenomena as well as in interpreting adsorbate structures and will be addressed in greater detail in the upcoming chapters.

### 2.1.3 Surface Reconstruction of Au(111) Electrodes

The environment of surface atoms is asymmetrical compared to that of bulk atoms. The lack of binding-partners results in an imbalance of forces. For some metals, this could cause a lateral shift of the upper surface atoms towards energetically more favoured structures.<sup>[93-95]</sup> This phenomenon is known as surface reconstruction. Surface reconstruction is unique for clean (*i.e.* adsorbate-free) surfaces of  $5d$  transition metals, such as iridium, platinum and gold. In an electrochemical environment, these surfaces can be stable at potentials negative of the potential of zero charge (*pzc*). The reconstructed surface structure can greatly differ in terms of morphology and thermodynamic stability, from the unreconstructed  $(1 \times 1)$  surface structure. The reconstruction is associated with a change in the bond angle, the rotational symmetry, and the number of nearest neighbours. This leads to more densely packed upper surface atoms and thus to a lowering of the surface energy,<sup>[78]</sup> which can directly be identified by electrochemical methods.<sup>[78,96]</sup>

Although the reconstructed surface (*rec*) is thermodynamically stable, a high activation energy barrier prevents the spontaneous reconstruction of a surface from taking place at room temperature.<sup>[97]</sup> The less compressed and hence thermodynamically unstable  $(1 \times 1)$ -structure is therefore in a metastable state. To overcome the activation barrier of the  $(1 \times 1) \rightarrow (rec)$ -structure transition, enough energy needs to be supplied to the surface atoms, either thermally or electrochemically.

For thermal-induced reconstruction, the crystal can be flame annealed and cooled down slowly in an atmosphere of  $N_2$  (see Section 3.2).<sup>[77,98]</sup> A fast cooling of the crystal,

like quenching with water, is avoided as it would freeze non favoured and/or unordered structures of surface atoms. This rather simple method yields high quality and smooth reconstructed surfaces.<sup>[10,78,99,100]</sup> In the case of a Au(111) electrode for example, the (1×1)-structure at higher temperatures, transitions into a densely packed reconstructed surface and exhibits a  $(\sqrt{3} \times 22)$  structure which occurs due to the compression of surface atoms by 4.4% along one of three [110]-directions.<sup>[100–103]</sup> The atoms of the uppermost layer can no longer lay in the hollow-sites of the underlying layers. This stacking mismatch between the first and second atomic layers results in a double-striped structure which alternately occupies areas with *fcc* and *hcp* stacking, is also known as the *herringbone* structure (Figure 2.3). The spacing between each corresponding double row is around 6.2 nm<sup>[78,96]</sup> which makes up around 22 Au atomic distances.

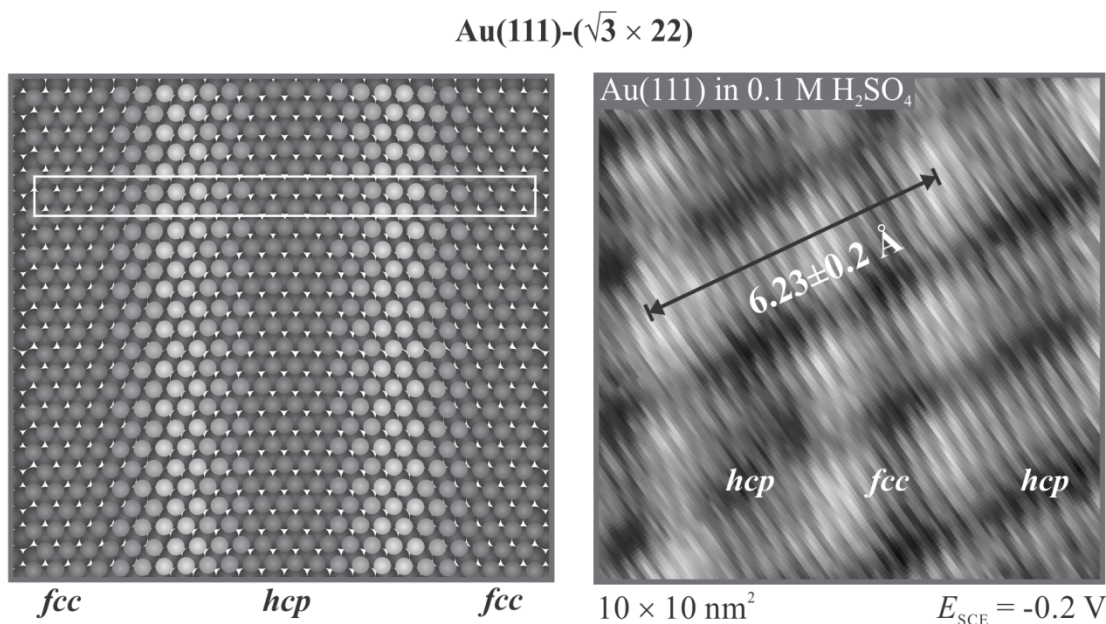


**Figure 2.3:** Schematic representation (left)<sup>[90]</sup> and *in-situ* STM image (right) of the Au(111)-( $\sqrt{3} \times 22$ ) surface reconstruction.

Since the surface tension also depends on the surface charge, the state of charge also influences the reconstruction of a surface.<sup>[104,105]</sup> A negative surface charge favours the reconstruction of a surface while a positive surface charge promotes the unreconstructed state. When applying a potential negative of the *pzc* to an already unreconstructed surface, a potential-induced surface reconstruction can be observed.<sup>[100]</sup> This is due to the

lowering of the activation energy again towards a more thermodynamically stable structure. In comparison to the thermally reconstructed surfaces described above, this method creates smaller domains of the herringbone structure. At negative potentials where no anions are adsorbed on the surface, the reconstructed surface is also stable.

The adsorption of oxoanions can *lift* the reconstruction. This is indicated by the fact that adsorption on the  $(1\times 1)$ -structure surface is energetically more favourable than adsorption on the more densely packed reconstructed surface.<sup>[78]</sup> The increase in the coordination number of the upper surface atoms by the adsorbates additionally favours the  $(1\times 1)$ -structure. The fact that a reconstructed upper surface should also be present in an electrochemical environment (in electrolyte) was a matter of controversy for a long time until a large number of electrochemical investigations have proven its existence<sup>[99,106-111]</sup> as shown in Figure 2.3. The reconstructed surface under electrochemical conditions is very similar to the one observed under UHV conditions. This provides a great deal of insight on the details of the  $(rec) \rightarrow (1\times 1)$ -structure transition.<sup>[10]</sup>

During the lifting of the reconstruction, the additional atoms are pushed out of the surface. Those atoms can then diffuse on the surface and form numerous small monoatomic high gold islands. The islands are observed to coalesce and grow with time. After about 30 min. of imaging an unreconstructed surface, the islands reach their maximum size. For unreconstructed Au(111) surfaces, the monoatomic high islands cover 4.4% of the surface. Islands could grow via two different mechanisms.<sup>[112]</sup> The first and more frequently observed mechanism is a two-dimensional Ostwald ripening where small islands in the vicinity of larger ones (or of steps) break down and disappear, while the larger islands grow.<sup>[112]</sup> The second involves the islands migrating as a whole. STM studies have shown that, for anion covered single-crystal electrodes, a change in the mobility of gold atoms is observed. The mobility of atoms and the final size of a gold island could depend on the nature of anion in solution.<sup>[1,2,112]</sup> In general (i) the mobility of atoms on the surface is inversely proportional to the diameter of the islands, and (ii) the average distance between islands is around twice the diameter. Surface defects such as monoatomic high islands or monoatomic deep holes could form or disappear rather quickly on a smooth, clean surface Au surface.

#### 2.1.4 Surface Defects

An ideal single-crystal electrode surface is defect-free. However, the crystal electrodes used in experiments are usually inhomogeneous and contain defects.<sup>[77,113]</sup> Figure 2.4 presents

the so-called Kossel crystal<sup>[114]</sup> which is commonly used as a model for ‘real’ crystal surfaces, depicting a number of different defects which are represented by STM images.

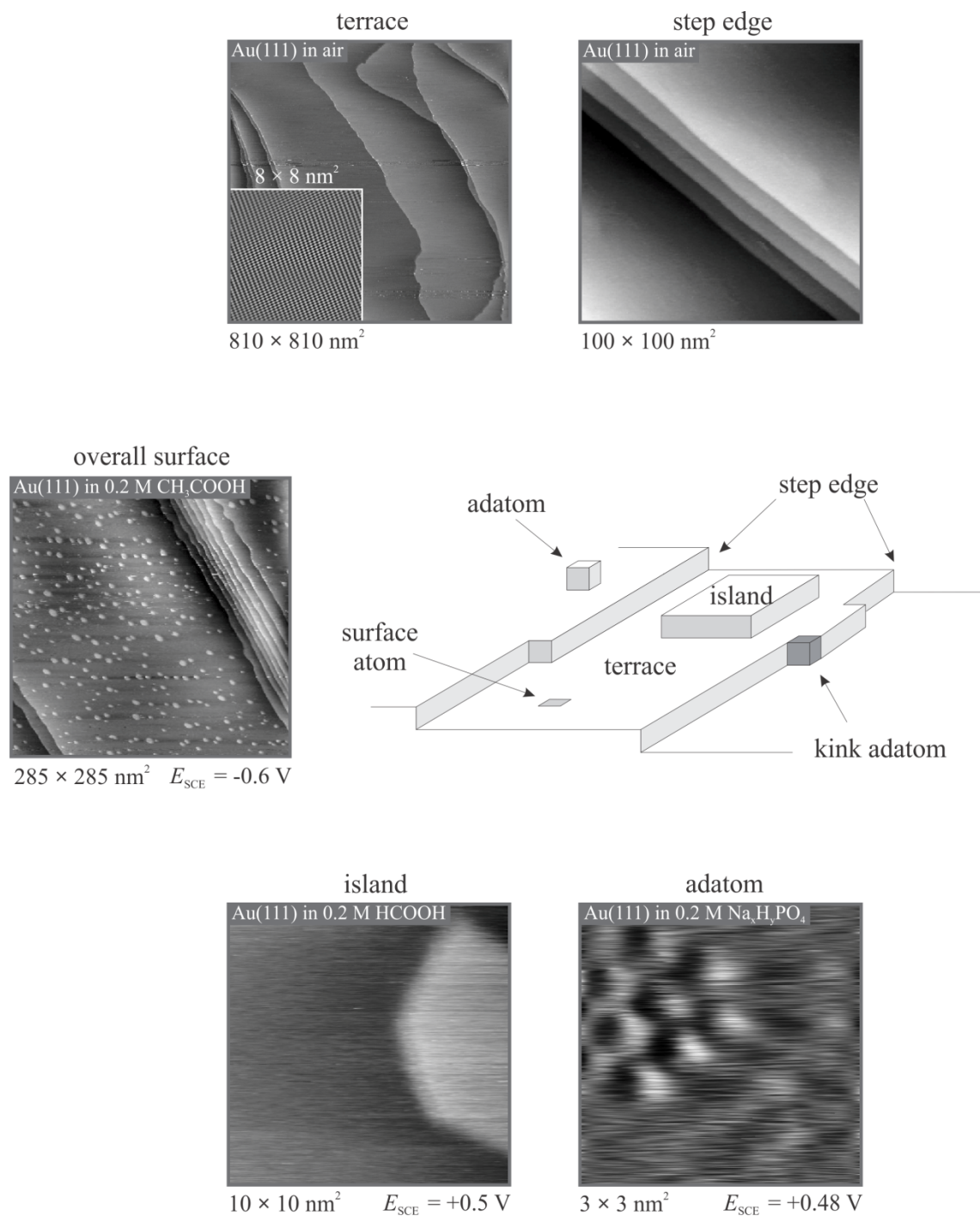


**Figure 2.4:** Structure of a crystal surface represented by Kossel's Model<sup>[114]</sup> and *(in-situ)* STM images of a Au(111) surface, displaying important surface morphologies and defects.

The most common surface defects on single-crystal surfaces are step edges, islands, adatoms, vacancies and dislocations. These defects can be caused by cutting and polishing<sup>[115]</sup> or by inappropriate crystal preparation.<sup>[77]</sup> The electrochemical properties of an electrode depend on its surface structure which is determined not only by the crystallographic orientation of smooth terraces but also by surface defects. Defects represent energetically inhomogeneous sites on the crystal surface and can influence the adsorption behaviour of ionic species.<sup>[116,117]</sup> Therefore, the adsorption at surface defects can be favoured over the adsorption on terraces or vice versa, depending on the chemical and geometric properties of the adsorbing species. For electrochemical adsorption measurements, the single-crystal electrode used should have large terraces, where the surface atoms are arranged as those of the underlying Miller plane. For that reason, the careful preparation of the electrode is necessary to obtain terraces that are wide enough, to aid in the formation of ordered adsorbed structures, making it easier to image the adsorbates.

## **2.2 Adsorption of Ions on Metal Electrodes**

### **2.2.1 The Metal-Electrolyte Interface**

The central concept of electrochemistry revolves around the interfacial boundary between a charged surface and an ionic solution (Figure 2.5) which governs the external observations of electrochemical reactions.<sup>[118]</sup> In this work, the charged surface is a metal that is in contact with an aqueous electrolyte. Since the metal surface is charged, there must be a balancing counter charge which occurs in the electrolyte.<sup>[119]</sup> The charge separation leads to the formation of the so-called *electric double-layer* which can simply be described as a plate capacitor with the electrode on one side and the adsorbed ions on the other side.<sup>[120,121]</sup> This arrangement corresponds to the fixed (rigid) Helmholtz double-layer model.<sup>[122]</sup>

Nonetheless, the charges will not uniformly be distributed throughout the aqueous phase but will be concentrated near the electrode surface. Due to their dipole moments, water molecules will compete with ions for sites on the surface. If the ions strip off their solvation shell and alter their dielectric constant during adsorption, this is known as *specific adsorption*.<sup>[121]</sup> The adsorption of ions at the electrode surface occurs if electron transfer reactions do not take place. This compensates for the excess charge on the

electrode and helps maintain electroneutrality. The plane where the charge centres of the specifically adsorbed ions are located forms the inner Helmholtz plane (IHP). On the other hand, the layer which contains the heavily charged solvated ions is called the outer Helmholtz plane (OHP).<sup>[119]</sup>

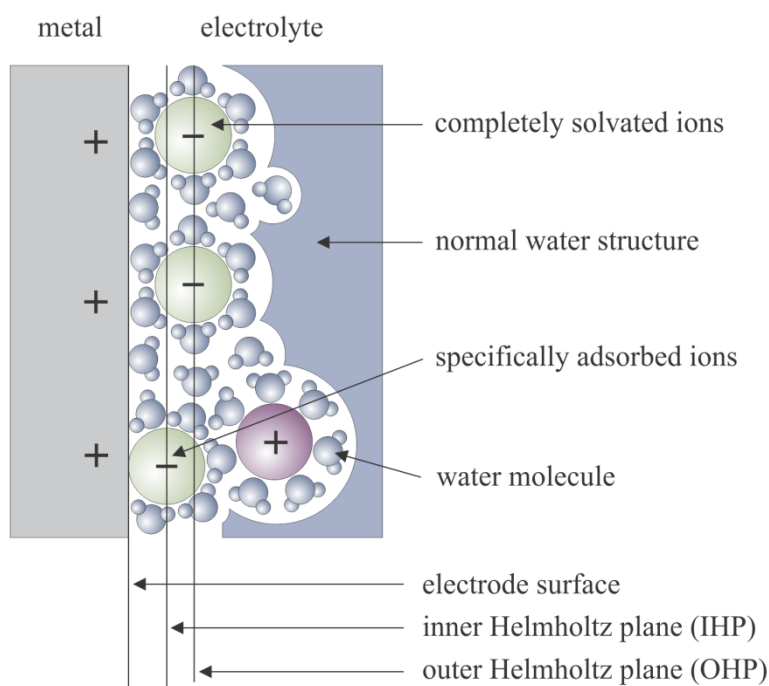


**Figure 2.5:** Model of the metal-electrolyte interface where the metal is positively charged.<sup>[123]</sup>

Anions are prone to specific adsorption and therefore may be adsorbed on the electrode surface. Cations usually retain their solvation shell and remain outside the layer of strongly oriented and adsorbed solvent molecules. This concept gave rise to an extended electrical double-layer model that was proposed by Gouy-Chapman known as the diffuse double-layer model comprising ions and solvent molecules extending some distance from the solid surface. The diffuse layer extends from the OHP to the bulk solution where the ionic distribution is influenced by the ordering due to columbic forces and the disorder caused by random thermal motion, resulting in an exponential drop in the potential.<sup>[124]</sup> The Stern model combines both models; Helmholtz and Gouy-Chapman, in series (see Figure 2.5). A more detailed description of the electric double-layer can be found in numerous electrochemistry textbooks.<sup>[119,125–127]</sup>



### 2.2.2 Fundamental Principles of Adsorption

As mentioned above, adsorption describes the accumulation of particles (adsorbates) on a surface (electrode).<sup>[120,121]</sup> In turn, the detachment of the adsorbates from an electrode surface is called desorption. Adsorption is usually caused by chemical interactions, mainly covalent forces, between the adsorbate and the electrode and is then denoted as *chemisorption*. In some cases, however, adsorption is caused by weaker van der Waals forces, which is then called *physisorption*. The adsorption enthalpy of chemisorbed molecules is typically ten times higher than physisorbed molecules, resulting in much smaller distances between adsorbate and substrate, in case of chemisorption compared to physisorption.<sup>[120]</sup> Naturally, the solvent is always present at the interface; therefore, if a molecular species is to be adsorbed on the electrode surface, its interaction with the electrode must be higher than that of the solvent. Depending on the nature of the adsorbate and the electrode potential, adsorption can be favoured, weakened or completely suppressed.<sup>[119]</sup> As discussed above in Section 2.2.1, adsorption involves at least partial desolvation. Species tend to specifically adsorb when their concentration at the interface is greater than electrostatic forces can account for. Since cations compared to anions tend to have stronger solvation shells, they are less probable to be adsorbed specifically on an electrode surface. Specific adsorption can even occur for ions on an electrode of the same state of charge.<sup>[119,121]</sup> In this case, the sign of charge moves from the inner Helmholtz plane towards the outer Helmholtz plane as the counter ions accumulate further away from the surface.

During adsorption, molecules can be distorted due to the interaction with the electrode surface. Molecular fragments are usually more reactive than an intact molecule, which is why chemisorption is important in catalytic processes. Adsorbed species on the surface are rather mobile.<sup>[121]</sup> Nonetheless, adsorbates can be statistically distributed over the whole surface or be arranged in an ordered structure that is aligned to the underlying substrate surface. The total amount of adsorbed species on an electrode surface is usually given in terms of coverage  $\theta$ , which is defined as the fraction of the surface covered with the adsorbate.<sup>[119]</sup> If the adsorbate forms a complete monolayer (ML),  $\theta$  will equal to one, which is the ratio of the amount of species adsorbed on the surface to the maximum amount which can be adsorbed. The area covered by a single adsorbed molecule could change with coverage. For instance, in a few electrochemical systems, some organic molecules, lie flat at low coverage and stand up at higher coverage.<sup>[11]</sup> In this case, the configuration of the molecule to which the coverage relates must be specified. For this

work, the studied molecules are quite small, making it difficult from the STM images, alone to interpret the orientation of an adsorbed species. Therefore, the calculated coverages are not assumed to change with changing the configuration of the adsorbate.

The adsorption of species takes place at characteristic sites of the electrode, for instance on top of atoms or in the bridge position between two atoms. Most adsorption studies are therefore performed on well-defined surfaces, *e.g.* the surface plane of a single-crystal electrode. Among the different single-crystal surfaces, the densely packed (111) orientation of *fcc* metals is the most fundamentally investigated since its hexagonal surface makes it a prime candidate for adsorption studies.

A *potential sweep*, also known as *cyclic voltammetry*, is a simple way of studying the potential dependence of an adsorption process.<sup>[80–82]</sup> It is sensitive to electrochemical processes taking place at the interface and can therefore identify changes at an electrode surface. In this procedure, the electrode is first in contact with the electrolyte and held at an initial potential that demonstrates purely capacitive behaviour. At this potential, ideally no reactions take place and adsorption is negligible. In this work, this region is referred to as the commonly known *double-layer region*. The electrode potential is then linearly swept between two limiting potential values ( $E_1$  and  $E_2$ ) at a constant scan rate ( $v = dE/dt$ ), as shown in Figure 2.6. At the limit potential, the direction of the potential sweep is reversed and the current (current density) is recorded against the potential to obtain a voltammogram.

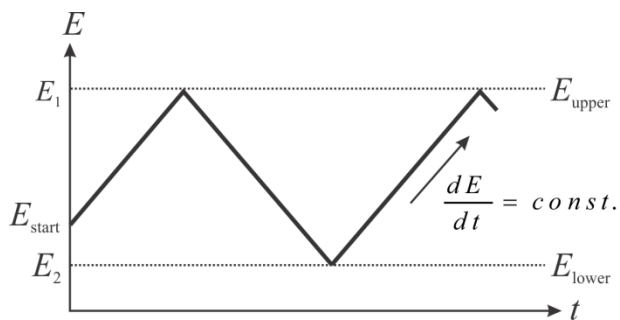


**Figure 2.6:** Triangular voltage of the limiting potentials ( $E_1$  and  $E_2$ ) used for cyclic voltammetry.

As long as potentials are in a range where no reactions take place, no current will flow over the metal-electrolyte interface. The current however, directly depends on the double-layer capacity. By altering the scan rate, the double-layer will be charged or

discharged like a capacitor. Once electrochemical reactions that are related to charge transfer through the interface take place, Faradaic currents flow and overlay onto the capacitive currents. The current depends on the nature and concentration of electrochemically active species which take part in different reactions at the interface. Thus, the scan rate  $v$  must be chosen with care, *i.e.* it should not only allow the reaction to be in equilibrium with negligible double-layer charging but also allow enough current to flow. Sweep rates of around 1–100 mV s<sup>-1</sup> are commonly used for adsorption studies.

If the mechanism of a reaction is to some extent established and hence, the number of the electrons involved in the reaction is known, conclusions can be drawn about the adsorbate coverage on an electrode. In the simplest case, the current is proportional to the change of coverage with time. The peaks in the current-potential curves provide information about the nature of the adsorbate interaction and the total charge  $Q$  of an electrochemical process. For instance, a repulsive adsorbate interaction will broaden the peak while an attractive interaction will lead to narrower (sharp) peaks, which in this case are called current *spikes*. These spikes are commonly related to a phase formation or *phase transition* within an adlayer of specifically adsorbed anions on well-ordered electrode surfaces.<sup>[7]</sup> Anodic and cathodic spikes are related to adsorption and desorption processes, respectively. If the peak boundaries of the adsorption/desorption spikes (peaks) are well-resolved, the coverage of the adsorbed anions can be estimated by a simple integration of a current-potential curve. Of course, using a different integration method or limit could result in slightly different coverages. However, the amount of error which may arise is usually not significant. First, the amount of  $Q$  can be calculated by integrating the curves as shown in Equation 2.1.

$$Q = \int_{E_1}^{E_2} \frac{I}{v} dE \quad (2.1)$$

However, as mentioned above, the calculated charge contains a Faradaic component ( $Q_F$ ) (*i.e.* due to current passing through the interface) in addition to a capacitive component that depends on whether or not an electrode surface is covered. The capacitive part ( $\Delta Q$ ) is calculated according to Equation 2.2 and must be subtracted from the measured total charge ( $Q$ ) to separate both components from one another.

$$Q_F = Q - \Delta Q \quad (2.2)$$

Approximate experimental isotherms are determined from charge density *vs.* potential plots. Since it is difficult to determine the true amount of capacitance in the double-layer region, assumptions are made. The first assumption is that the double-layer capacity of Au(111) is the same with and without the electrochemically active species in solution. This is done by subtracting charge density values for Au(111) in the absence of specifically adsorbing species from the total charge density values (in the presence of the species). The second assumption is that the charge per adsorbed species is constant. Under those conditions, it is possible to determine the coverage  $\theta$  at a given electrode potential by measuring the charge which flows:

$$\theta(E) = \frac{Q(E)}{Q_o} = \frac{1}{Q_o} \int_{E_1}^{E_2} \frac{I}{v} dE \quad (2.3)$$

where  $Q_o$  is the charge required to form a monolayer of the adsorbate and potential  $E_1$  must be in a region where no species are adsorbed. Of course, the charge density  $q$ , instead of charge  $Q$ , should always be used in order to relate the values to the electrochemical active surface area. To determine the total coverage of anions on the Au(111) surface, a charge density of 222.45  $\mu\text{C cm}^{-2}$  is used (for the transfer of one electron per Au surface atom).<sup>[128]</sup>

### 2.2.3 Structures of Commensurate Adlayers on Single-crystal Surfaces

The adlayer structure resulting from the adsorption of a species on a single-crystal surface depends on different factors, such as the relative size of the adsorbate and substrate atoms as well as the interactions between the particles involved. The adsorption of ions on an electrified interface could involve repulsive interactions between the adsorbed species, which results in a homogenous distribution of species on the surface. As discussed above in Section 2.2.2, there are preferential sites (on-top, bridge, threefold sites, *etc.*) for the adsorption of species. Since this work focuses on imaging ordered structures of adsorbed oxoanions on a Au(111) electrode surface, an overview on the distribution of an adlayer with respect to the underlying substrate surface, is given.

The surface atoms of single-crystals are periodically arranged in a manner which is determined by the cutting direction of the crystal, as already mentioned in Section 2.1. The structure of a single-crystal surface can be described by its simplest periodically

repeating unit cell in a two-dimensional array. As shown in Figure 2.7, two vectors  $a_1$  and  $a_2$  are usually chosen to define the unit cell. Similarly, a unit cell of an ordered adlayer of adsorbates on a surface can be defined by means of  $b_1$  and  $b_2$ .<sup>[105]</sup> If a simple mathematical transformation relates the adsorbed structures and the substrate, a *commensurate* structure is defined.<sup>[129]</sup> Otherwise, the structure is *incommensurate*. In the case that the vectors form the same angle, *Woods notation* is used to describe the two separate unit cells corresponding to the adlayer and the substrate. The lengths of the two vectors  $b_1$  and  $b_2$  are described respectively in terms of  $a_1$  and  $a_2$ , as  $\left(\frac{|b_1|}{|a_1|} \times \frac{|b_2|}{|a_2|}\right)$ .<sup>[105]</sup>

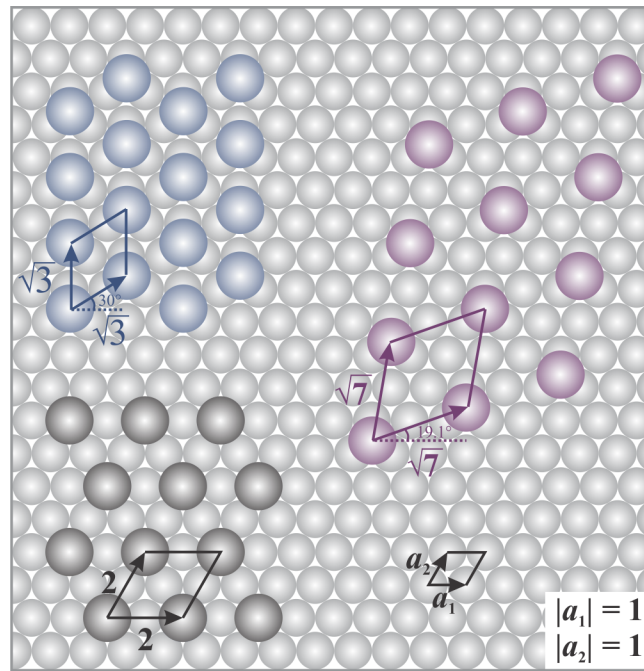


**Figure 2.7:** Model of a hexagonal  $fcc(111)$  substrate with different adsorbate structures, where a  $(2 \times 2)$ , a  $(\sqrt{3} \times \sqrt{3})R30^\circ$  and a  $(\sqrt{7} \times \sqrt{7})R19.1^\circ$  superstructure is represented in black, blue and pink, respectively.

As an example, Figure 2.7 shows a  $(2 \times 2)$  structure on the  $(111)$  plane of an  $fcc$  crystal. The distances between two adsorbates are twice the atom-atom distance in the  $fcc(111)$ - $(1 \times 1)$  unit cell. This results in a hexagonally close packed structure with a theoretical enclosing angle ( $\alpha$ ) of  $60^\circ$ . The enclosing angle is specified as the smallest measured angle separating two rows of an ordered structure and is commonly recognized to be  $< 90^\circ$ .<sup>[105]</sup> The adsorbate in this case adsorbs on a top site of the substrate atom;

nonetheless, the same concepts can be applied for other adsorption sites. Other typical adlayer structures that are often observed on the (111) surface are the  $(\sqrt{3} \times \sqrt{3})R30^\circ$  and the  $(\sqrt{7} \times \sqrt{7})R19.1^\circ$  structures, also shown in Figure 2.7. Here the structures are rotated ( $R$ ) by an angle, with respect to the substrate unit cell. It should be noted that the letter  $p$  often precedes the description of the structures and is represented as  $p(2 \times 2)$  for example, to specify that it is a primitive structure (the simplest unit cell possible). This denotation distinguishes the structure from the closely related  $c(2 \times 2)$  structure, where an additional species lies in the centre of the structure.

The unit cell of the adlayer structure is a function of the coverage.<sup>[93]</sup> Regardless of the size of the adsorbate in a model, if the adsorbate occupies all equivalent adsorption sites of a substrate surface, the coverage  $\theta$  amounts to  $\theta_{\max}$  and the unit cell of the adlayer structure is equivalent in size to that of the substrate. The coverage measured from current-potential curves is always compared to that calculated from the STM images.

#### **2.2.4 Adsorption of Sulfate on Au(111): The Benchmark**

Studying the adsorption of anions on electrified surfaces is significant in electrochemistry because electrocatalytic reactions involve at least one adsorption step. Besides this, adsorbed anions (i) alter the distribution of the electric charge at the metal/electrolyte interface, (ii) influence the voltammetry of single-crystal electrodes,<sup>[130]</sup> (iii) modify the electrode surface and thus, affect electrocatalytic activity, and (iv) change the structure of the underpotential deposition (UPD) of metals.<sup>[131]</sup> (An UPD process results in thin metal films of up to a few monolayers in thickness and takes place at an electrode potential range which is more positive than the Nernstian potential for bulk deposition.) Hence, to help optimize electrocatalytic reactions and develop realistic theories of the electrochemical interface, understanding the nature of anionic adsorption at metal surfaces is essential.

For years, a Au(111) electrode in 0.1 M  $\text{H}_2\text{SO}_4$  has been used to understand the basics of adsorbed adlayers on electrified metallic surfaces and to determine the quality of a single-crystal electrode surface.<sup>[1,8–10,24–27]</sup> As a benchmark measurement at the Institute of Electrochemistry, the acquisition of high-resolution *in-situ* STM images of this system is mandatory to ensure the possibility of studying more complex systems.<sup>[90,132,133]</sup> Figure 2.8 shows the current-potential curve of a freshly prepared Au(111) crystal in 0.1 M  $\text{H}_2\text{SO}_4$  at a scan rate of 10 mV s<sup>-1</sup>. The stability of the potential window is limited at negative

potentials by the onset of hydrogen evolution and at positive potentials by the onset of gold surface oxidation. Negative of around 0.2 V, a purely capacitive region is observed. At this potential region and negative of the *pzc* ( $\sim 0.32$  V),<sup>[106]</sup> a thermal-induced ( $\sqrt{3} \times 22$ ) reconstructed surface, very similar to that found under UHV conditions,<sup>[103,134]</sup> is imaged using *in-situ* STM. This is because no specific adsorption of anions takes place in this potential region.

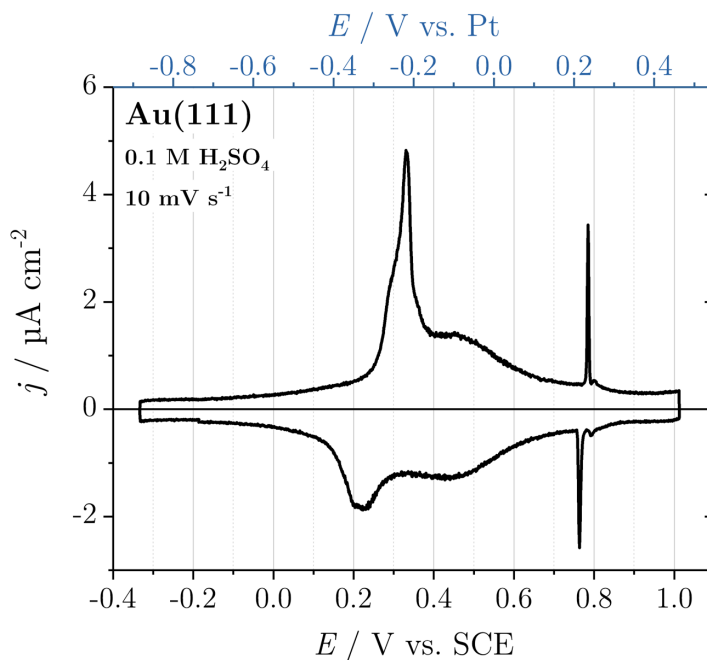


**Figure 2.8:** Current-potential curve of a freshly prepared Au(111) electrode in 0.1 M H<sub>2</sub>SO<sub>4</sub> at 20 °C. Scan rate: 10 mV s<sup>-1</sup>. Also shown, is the measured potential *vs.* Pt pseudo-reference electrode (blue scale).

The shape of the reconstruction lines does not only depend on the annealing temperature of the crystal<sup>[90,100]</sup> but also on the potential at which the electrode is immersed into the electrolyte.<sup>[30]</sup> Details regarding the potential dependence on the shape of the reconstruction lines will be discussed later in Chapter 0. As an example, the typical herringbone structure of the reconstructed surface is seen in Figure 2.9a at a potential close to the *pzc*. At more positive potentials, the reconstruction transforms to a (1×1) structure (peak in Figure 2.8) due to the onset of adsorption of sulfate anions at around 0.2 V.<sup>[96]</sup> Since the reconstructed surface atoms are compressed relative to the bulk atoms,

$\sim 4\%$  of islands form on the surface (Figure 2.9b). With increasing the potential, the sulfate coverage continues to increase until a phase transition (spike in Figure 2.8) within the adsorbed sulfate adlayer is observed at around 0.8 V. Sulfate adsorbs like a typical anion where the charge density increases constantly with increasing potential.<sup>[35]</sup>

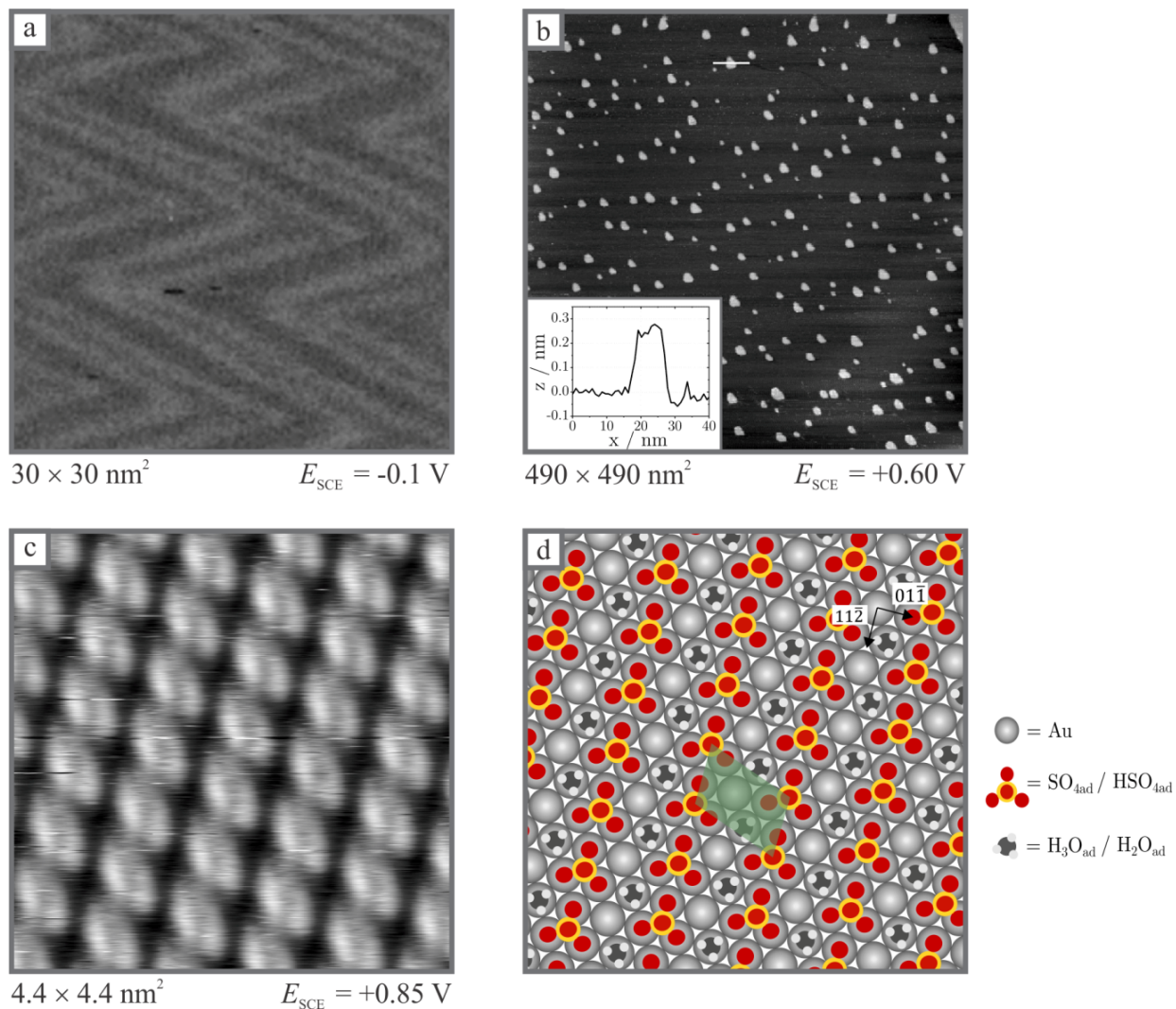


**Figure 2.9:** *In-situ* STM images of Au(111) in 0.1 M H<sub>2</sub>SO<sub>4</sub> showing the Au(111) (a) ( $\sqrt{3} \times 22$ ) surface reconstruction at a potential close to the *pzc*:  $30 \times 30 \text{ nm}^2$ ,  $E = -0.1 \text{ V}$ ,  $U_T = 0.2 \text{ V}$ ,  $I_T = 2 \text{ nA}$ , (b) ( $1 \times 1$ ) surface after lifting of reconstruction, before phase transition:  $490 \times 490 \text{ nm}^2$ ,  $E = 0.60 \text{ V}$ ,  $U_T = 0.4 \text{ V}$ ,  $I_T = 2 \text{ nA}$ , where the inset is the height profile of a monoatomic high Au island, (c) adsorbed sulfate structure, positive of the phase transition peak:  $4.4 \times 4.4 \text{ nm}^2$ ,  $E = 0.85 \text{ V}$ ,  $U_T = 0.5 \text{ V}$ ,  $I_T = 2 \text{ nA}$ , and (d) model of the ( $\sqrt{3} \times \sqrt{7}$ ) $R19.1^\circ$  structure of adsorbed SO<sub>4</sub><sup>2-</sup> or HSO<sub>4</sub><sup>-</sup> ions and, coadsorbed H<sub>3</sub>O<sup>+</sup> ions or H<sub>2</sub>O molecule, on the Au(111) surface.



Positive of the phase transition spike in the corresponding current-potential curve (Figure 2.8), the charge for sulfate adsorption on Au(111) is around  $45 \text{ } \mu\text{C cm}^{-2}$  which corresponds to a sulfate coverage  $\theta_{\text{sulfate}}$  of  $\sim 0.2 \text{ ML}^{[9,90]}$  (using a charge density of  $222 \text{ } \mu\text{C cm}^{-2}$  for the transfer of one electron per Au surface atom). In this potential region, parallel rows of adsorbed sulfate<sup>[7,8,33–37]</sup> with two kinds of maxima are observed in the STM image (Figure 2.9c). The main maxima are the brighter large ones which correspond to adsorbed  $\text{SO}_4^{2-}$  or  $\text{HSO}_4^-$ . The secondary smaller maxima are assigned to either coadsorbed  $\text{H}_3\text{O}^+$  ions in their non-solvated<sup>[33]</sup> or solvated states,<sup>[37]</sup> or to  $\text{H}_2\text{O}$  molecules which stabilize the structure. The measured  $\theta_{\text{sulfate}}$  could correspond to either  $\text{SO}_4^{2-} + \text{H}_3\text{O}^+$  or  $\text{HSO}_4^- + \text{H}_2\text{O}$ . It is more likely (and favourable) that upon adsorption, either a forced dissociation of the weaker  $\text{HSO}_4^-$  acid to its conjugate base seems to occur on the surface, or a selective adsorption of  $\text{SO}_4^{2-}$  takes place.<sup>[8]</sup> Sulfate is known to form the well-known  $(\sqrt{3} \times \sqrt{7})R19.1^\circ$  structure<sup>[1,9]</sup> on Au(111) electrodes in  $0.1 \text{ M H}_2\text{SO}_4$  (Figure 2.9d). In this work, *in-situ* STM imaging of the surface directly after a potential step to  $0.85 \text{ V}$ , has reproducibly (and surprisingly) revealed that not one, but rather three different structures appear on the surface. These structures will be discussed later in Chapter 0. Interestingly, very few electrochemical (experimental and theoretical) studies report a different  $(\sqrt{3} \times \sqrt{3})R30^\circ$  structure of adsorbed sulfate on Au(111) at a potential range close to the sulfate adsorption maximum.<sup>[135,136]</sup>

If the potential is again stepped to values negative of the lifting of surface reconstruction peak where no specific adsorption is expected, the reconstructed surface is potential-induced. The previously imaged herringbone structure in this case, forms a more random structure with smaller *herringbone-like* (kinks) domains and more parallel reconstruction lines instead. In addition, due to the recompression of surface atoms, small holes appear on the surface (not shown).

### 2.2.5 Adsorption of Other Oxoanions on Au(111)

In contrast to sulfate, very few structural studies are performed for other oxoanions with the same tetrahedral structure and similar size, *e.g.* phosphate, on metallic surfaces.<sup>[9,20]</sup> This is mainly because phosphate compared to sulfate, specifically adsorbs on surfaces which are in solutions of much higher pH values. This makes it extremely difficult to image an adsorbed structure since the experimental conditions change considerably. Details of the necessary experimental conditions are explained in Section 3.4. Of the few reported studies, *in-situ* STM imaging in acidic and neutral buffer solutions containing

potassium were carried out. So far, no ordered structures of phosphate like those observed for sulfate on an electrode surface have been reported.<sup>[9]</sup> Instead, only small patches of a partially ordered layer for phosphate anions on a Au(111) electrode surface in the presence of potassium cations were imaged.<sup>[20]</sup> The observed adlayer shows several defects but is described as parallel rows of phosphates with closest neighbouring distances that resemble a  $(\sqrt{3} \times \sqrt{7})R19.1^\circ$  structure and corresponds to  $\theta_{\text{phosphate}}$  of 0.20 ML. It is worth mentioning that the current-potential curve of the Au(111) surface in a  $\text{KH}_2\text{PO}_4 + \text{K}_2\text{HPO}_4$  (pH 6.9) electrolyte shows no indication (such as current spikes) for a phase transition within the adsorbed phosphate adlayer.<sup>[20]</sup> In comparison, other studies indicate that phase transition spikes are observed for phosphate buffers of a similar pH value but in the presence of sodium cations.<sup>[137]</sup> This is a strong indication of the influence of the nature of alkali metal cation ( $\text{K}^+$ ,  $\text{Na}^+$ ,  $\text{Li}^+$ ) on the electrochemical behaviour and the formation of ordered structures of adsorbed phosphate anions on the Au(111) surface.

In comparison to four-oxygen anions, the adsorption of two-oxygen anions is receiving much less attention. Formate and acetate are examples of simple carboxylates which makeup a significant group of species that adsorb strongly on catalytically active noble metal surfaces and can thus impact electrocatalytic reactions.<sup>[4,44–46]</sup> A structure of parallel chains has recently been imaged for  $\text{HCOO}_{\text{ad}}$  on Au(111) at a potential region where the electrooxidation of formic acid/formate takes place.<sup>[50]</sup> Electrosorption studies of formate on Au(111) surfaces are however, hampered by its electrocatalytic reaction.<sup>[50]</sup> Unlike formate, acetate is unreactive on gold.<sup>[51]</sup> This is because the C-H bond of formate is easier to split than the  $\text{H}_3\text{C-CO}_2$  bond of acetate. Similar adsorption behaviour is expected for all carboxylates. In other words, acetate is also expected to form parallel chains of an ordered structure where it adsorbs via the two oxygen atoms, in a bidentate configuration.<sup>[47,50,51,53–55]</sup> So far, only STM studies under UHV conditions was used to investigate the adsorption of acetic acid/acetate on noble and non-noble metal surfaces.<sup>[38–40,55,73]</sup> For a Au(110) surface, a dense  $c(2 \times 2)$  structure of acetate with a coverage of 0.25 ML was identified.<sup>[40]</sup> The same structure has been reported for Ni(110)<sup>[138,139]</sup> and for Cu(110).<sup>[39,140,141]</sup>

Strongly adsorbing anions show ordered structures that are interpreted as salt-like mixed structures of anions and cations.<sup>[1]</sup> Although the formation of an ordered adlayer depends on the adsorption strength of the anion, the adlayer spacing depends on the type and concentration of the cation.<sup>[142]</sup> With increasing potential, the adlayer becomes less dense due to the increase in cation-cation repulsion.<sup>[1,142]</sup> As ions in an aqueous solution are

normally solvated by water molecules, the solvation shell of the cations has to be considered. Alkali metal cations could influence the distribution of anions as a result of the electrostatic interactions between the solvated cations at the OHP and the adsorbed species having large dipole moments. Although the size of a cation does not necessary influence the spacing within an adlayer, an increase in cation size and concentration of cations at the OHP could affect the arrangement of anions on an electrified surface.<sup>[143]</sup>

### 2.2.6 Competitive Adsorption of Oxoanions for Formic Acid Oxidation

Electrocatalytic activities are usually affected by the presence of specifically adsorbing anions which act as spectator species in the reaction. Studies report that the presence of another oxoanion of similar geometry to formate such as acetate, partially blocks the oxidation of formic acid on Au(111).<sup>[52]</sup> In fact, in mixtures of formic and acetic acid, coadsorption of formate and acetate is expected. In comparison, sulfate and phosphate species, which most likely adsorb in a trigonal configuration on Au(111), have a much stronger blocking effect. Nonetheless, the presence of phosphate species is sometimes inevitable due to its strong buffering capacity which allows systematic pH dependence studies over a wide range.<sup>[63]</sup>

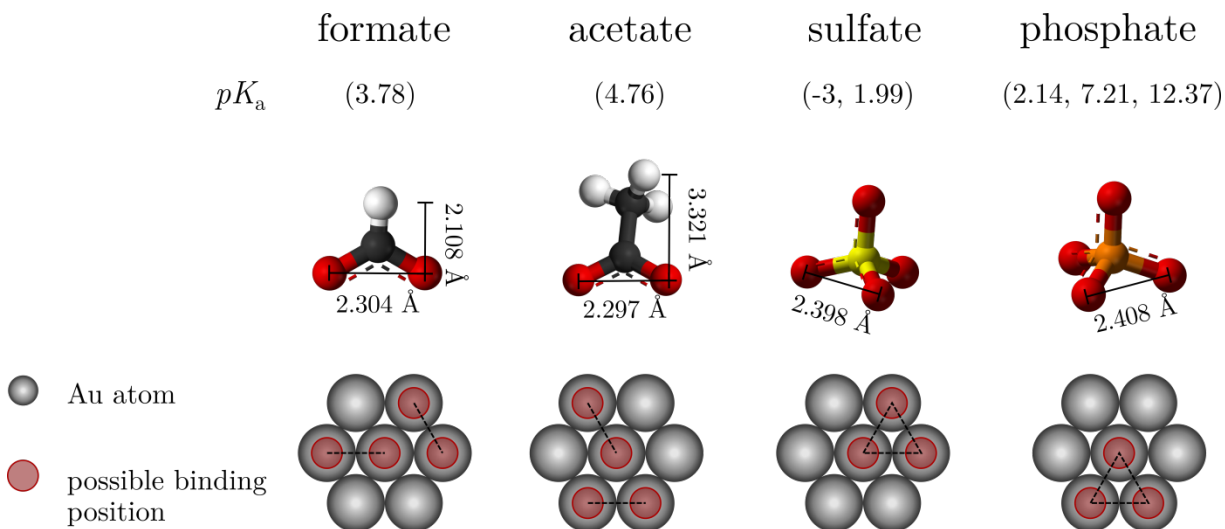


**Figure 2.10:** Model for the bidentate and tridentate configuration of formate and acetate, and sulfate and phosphate, respectively, adsorbed on Au(111). Similar  $pK_a$  values for deprotonation of formic and acetic acid in solution suggest comparable adsorption strength for formate and acetate on Au(111). Difference in  $pK_a$  values for sulfate and phosphate, compared to formate, suggest possible competition during adsorption.

It is possible that unreactive oxoanions and weakly bound formate compete with each other for free adsorption sites between rows of strongly bound formate species.<sup>[144]</sup> Clearly, the arrangement of adsorbed oxoanions on a metallic surface is expected to have important implications on the competition of active and spectator species for free active sites.<sup>[145]</sup> It is possible that different adsorbate configurations and surface  $pK_a$  values (Figure 2.10) influence the degree of competition and the possibility of forming mixed phases. A synergetic effect will depend on the (i) nature of the adsorbate, (ii) arrangement of the ordered structures, and (iii) relative ionic strength of adsorbed species.

## 2.3 Scanning Tunneling Microscopy

Scientists have been using *Scanning Tunneling Microscopy* (STM), since it was developed in the 1980s,<sup>[146,147]</sup> to represent the atomic structure of and the dynamic processes on metal surfaces, in real space.<sup>[21,83]</sup> Surface sensitive methods such as *Low Energy Electron Diffraction* (LEED) or surface X-ray diffraction on the other hand, provide structural information in reciprocal space which is averaged over the entire surface.<sup>[148]</sup> This aided in the rapid development of STM while extending its application to surfaces not only in vacuum but also in contact with air and electrolyte<sup>[149–151]</sup> making it possible to observe and understand initial stages of electrochemical processes in real space, down to the atomic scale. Since STM has become a standard method in surface science and the main tool of investigation in this work, a brief illustration of its operating principle and tunneling mechanism, is given below. Detailed theoretical or experimental concepts regarding the operating principle of scanning tunneling microscopy is found in literature.<sup>[129,152,153]</sup>

### 2.3.1 Operating Principle of Scanning Tunneling Microscopy

The operating principle of STM is based on the quantum mechanical tunneling phenomenon of an electron between an electrically conductive surface and a metallic tip. The fine tip is brought very close to the sample under investigation at a distance of around 0.5 to 1 nm. At this distance, the wave functions of the electrons of the tip and sample overlap without having mechanical contact. When a potential difference is applied, electrons tunnel between the tip and sample, overcoming a tunnel barrier ( $\Phi_T$ ). A representation of the energy relationship at the tunnel junction is given in Figure 2.11.<sup>[154]</sup>

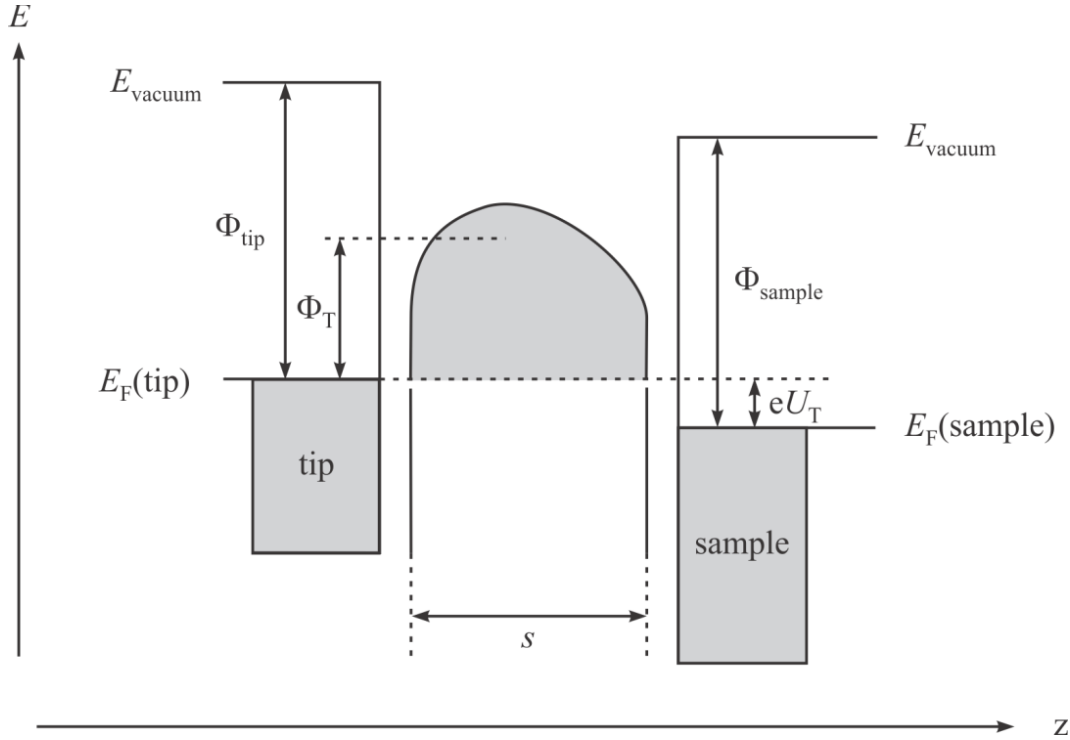


**Figure 2.11:** Schematic representation of the energy relationships at the tunnel barrier between an STM tip and a sample<sup>[155]</sup>, based on<sup>[154]</sup>, where  $s$ : distance between tip and sample,  $\Phi_{\text{tip}}$  and  $\Phi_{\text{sample}}$ : wave functions of tip or sample, respectively,  $\Phi_T$ : average tunnel barrier height and  $eU_T$ : energy difference between both corresponding Fermi levels.

In this simplified case, the electrons tunnel across the barrier from the tip to the sample in vacuum. The tunneling process occurs mainly with electrons of energies near the Fermi levels of the two electrodes. However, for this to occur there must be an empty level of the same energy as the electron on the other side of the barrier. Because of this restriction, the resulting current also known as the tunneling current can be related to the density of available or filled states in the sample. The lateral resolution on the other hand, strongly depends on the properties of the tip being used. A schematic representation of the functioning principle of a STM is shown in Figure 2.12. Energy relations, at the tunnel barrier, between an STM tip and a sample, are represented.

An atomically sharp tip is usually placed in a tube scanner consisting of a hollow piezoceramic cylinder that deflects due to its voltage dependence, in the sub nanometre range in each of the three special directions. With the help of the piezos, the tip is scanned line by line, across the surface in the  $x$ - and  $y$ - directions in order to map its topography. The tip movements are detected, and the measured data points are translated by a

computer to generate a topographic image of the surface in real space. There are two modes of operation when using STM.<sup>[156]</sup>

**Constant-height mode:** In this mode, the tip only moves in the x- and y- direction while the z-coordinates remain constant. Thus, the surface structure changes with varying the distance between the tip and sample and hence changes in the tunneling current. The exponential dependence between the tip to sample separation and the measured tunneling current provides information about the topography the substrate surface. The advantage of this mode is that the tip can scan the surface very fast since the STM is not hindered by the time response of the tip in the z-direction. However, this is only applicable for flat sample surfaces because otherwise there is a risk that the tip collides with surface and damages both itself and the sample.

**Constant-current mode:** In this mode, the tip scans the surface in the x- and y-directions while its vertical position, relative to the sample, is adjusted using an electronic feedback loop to maintain a constant tunneling current (setpoint). This is done by varying the voltage in the z-piezo to minimize the deviation between the given and actual setpoint values during the scanning process. The voltage at the z-piezo that is required to readjust the tunneling current to a constant value is recorded and recalculated to give a topographical image of the surface. Since the distance between tip and sample must be readjusted, low scan rates are required in this mode. However, rough surfaces can be imaged with minimum risk of destroying the tip or sample. This mode was used for all STM measurements in this work.

### **2.3.2 *In-situ* Scanning Tunneling Microscopy**

It has been recognized that scanning tunneling microscopy, unlike other spectroscopic methods like LEED, not only functions in ultra-high vacuum (UHV) but also in air or in solution. The reason for that is the absence of interactions of free electrons with the sample surface. Shortly after the STM was first established, high resolution images of the surface structure of graphite indicated that the atomic structure obtained in UHV<sup>[157]</sup> was comparable to those obtained in air<sup>[158]</sup> or in water.<sup>[149,150,159]</sup> Thereafter, several studies have elaborated the value of combining STM with an electrochemical cell (*in-situ* STM) to monitor electrochemical processes on and structural changes of the electrode surface under

potential control.<sup>[1,85,110,123,160,161]</sup> To perform such measurements however, some changes to the STM setup in vacuum are necessary.<sup>[162]</sup>

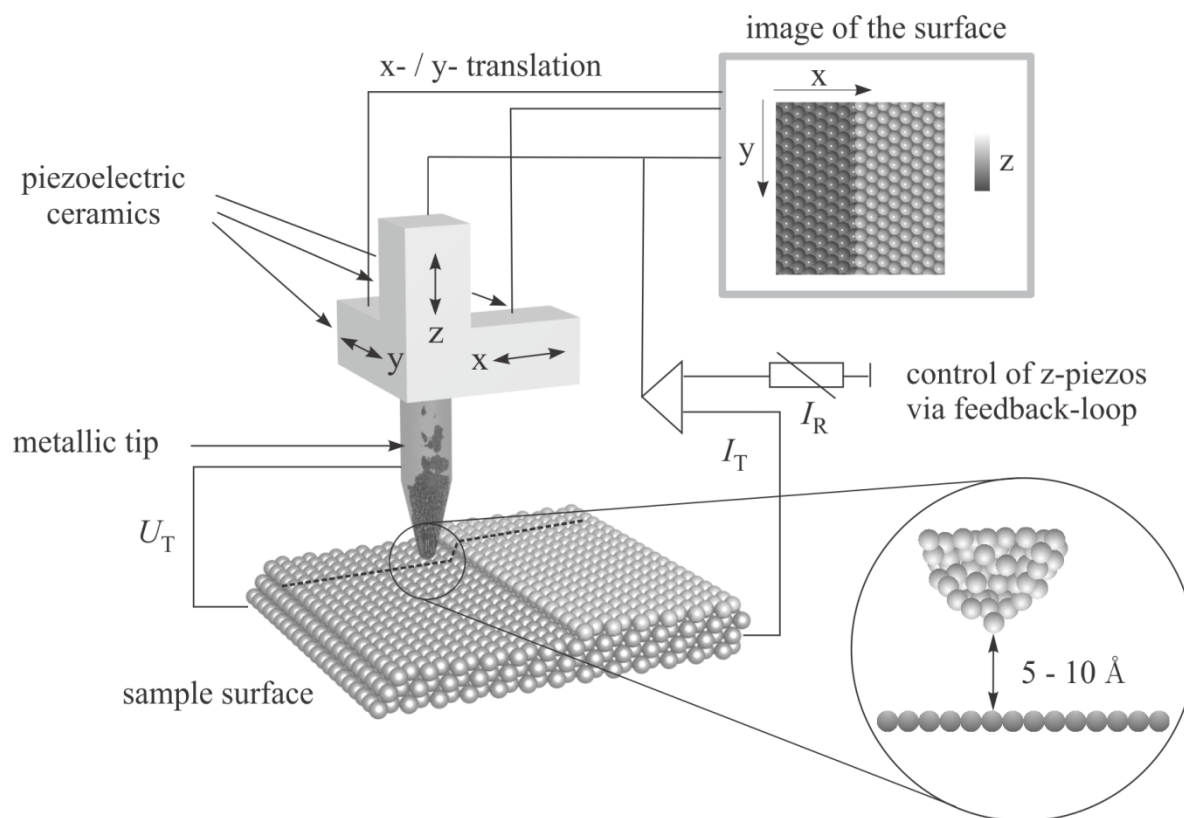


**Figure 2.12:** Functioning principle of scanning tunneling microscopy<sup>[155]</sup>, based on<sup>[163]</sup>.

Firstly, the tip that is immersed in the electrolyte acts like a fourth electrode in addition to the working, reference and counter electrodes. The basic four-electrode arrangement of an *in-situ* STM which has been used in this study is shown in Figure 2.13. Secondly, a bipotentiostat is used to ensure that the applied potentials at the tip and the sample are independently varied with respect to the reference potential. The difference between the applied tip potential ( $E_{\text{tip}}$ ) and sample potential ( $E_{\text{WE}}$ ), results in the tunneling voltage or bias ( $U_T$ ). The resulting tunneling current ( $I_T$ ) dissipates through the counter electrode. Thirdly, the tip must be isolated from the electrolytic environment to minimize leakage currents.<sup>[164]</sup> This is because at the tip/electrolyte interface, reactions may also occur that result in Faradaic currents that typically reach 1  $\mu\text{A}$ , which could mask the real tunneling current (around 1 nA). This is done by coating the tip with an

insulating material, leaving only the sharp end of the metal tip bare to allow tunneling current to flow (see Section 3.4.3). The Faradaic currents can thus be lowered to below 20 pA which is much lower than the electrical noise of the tunneling current, ensuring stable imaging of a surface structure.

In principle, the information obtained from the STM does not strictly map the topography of a sample but rather reflects the constant *Local Density Of States* (LDOS) at the Fermi level or very close to the surface of the sample.<sup>[156]</sup> For clean metal surfaces, the topography corresponds to the positions of atomic cores. For semiconductor or adsorbate-covered surfaces on the other hand, deviations may arise which make the interpretation of the STM image more difficult. In this work, the ‘maxima’ and ‘local maxima’ of an imaged ‘pattern’ in an *in-situ* STM image are ascribed to adsorbed anions and coadsorbed cations or molecules, which stabilize the structure. It should be noted that the close proximity of the tip to the sample surface may lead to an overlap of the electric double-layers of both the tip and sample which may result in local changes in the potential at the sample surface.<sup>[165,166]</sup>

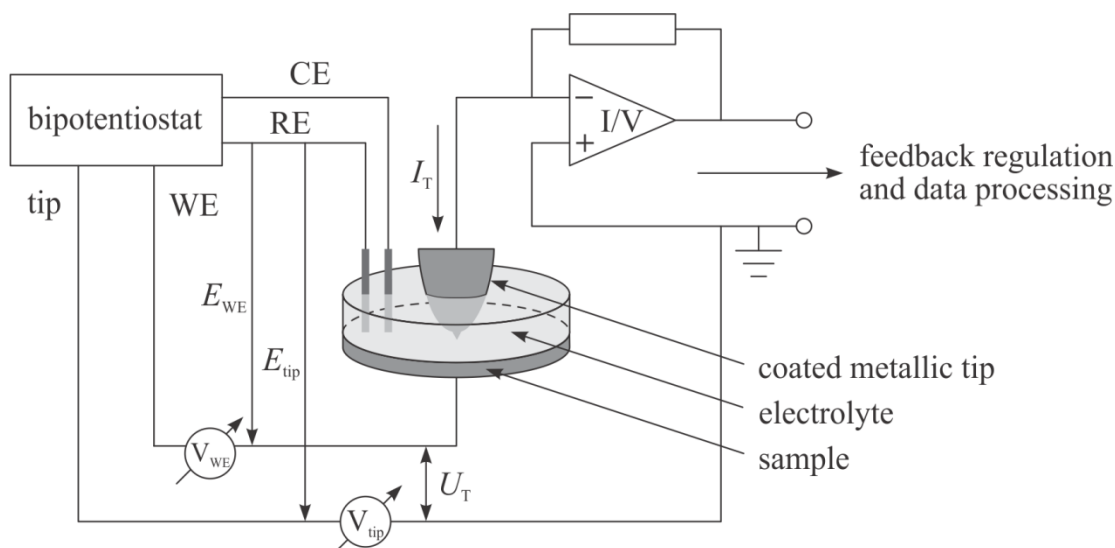


**Figure 2.13:** Schematic representation of the four-electrode arrangement of an *in-situ* STM<sup>[25]</sup> where RE: reference electrode, CE: counter electrode, WE: working electrode,  $U_T$ : tunneling voltage and  $I_T$ : tunneling current.



## 3 Experimental Methods

In order to obtain reproducible electrochemical and *in-situ* STM results, it is essential to have a contaminant-free system and prepare a clean and smooth metal surface. This chapter describes the details of the experiment which include cleaning procedures, sample and tip preparation methods, description of the electrochemical and *in-situ* STM cells, as well as of the STM setup, and finally a list of used chemicals.

### 3.1 Cleaning Equipment and Cells

Cleanliness plays a major role in electrochemical investigation methods as well as in scanning tunneling microscopy. Therefore, it is necessary to thoroughly clean all equipment, including cells, prior to each experiment. To do so, all glassware, plastic tweezers and STM cells were placed for at least 2 hours (preferably overnight) in a *piranha* (caroic acid) solution (conc.  $\text{H}_2\text{SO}_4$  and 30% aqueous  $\text{H}_2\text{O}_2$  in a 3:1 volume ratio). Because the bath is a strong oxidizing agent, it will remove most organic matter and will also hydroxylate most surfaces making them highly hydrophilic. Once removed from the bath, the glassware was thoroughly rinsed with ultra-pure water and then boiled out for 90 min. The water is replaced every 30 min. to ensure the removal of any remaining organic residue. Only then is the equipment free from contamination and ready for use. The tweezers and STM cell were blown dry using a nitrogen stream before assembling the cell for an experiment.

The electrochemical glass cell can also be submerged in caroic acid if needed. If the cell is clean, it is enough to thoroughly rinse it with ultra-pure water before each experiment and after the measurement, store it filled with water. The cleanliness of the cell was checked prior to each measurement by recording the current-potential curve of a well-established system, typically Au(111) in 0.1 M  $\text{H}_2\text{SO}_4$ . The extent of cleanliness was

determined by observing that certain features in the current-potential curve have the correct shape (and intensities) and occur at the expected potentials.

The ultra-pure water was acquired using a commercial water treatment machine (Sartorius Arium 611). The water used had a specific resistivity of  $18.2 \text{ M}\Omega \text{ cm}$  at  $25^\circ\text{C}$  and a residual amount of organic impurities (*Total Organic Carbon*, TOC) that is below 2 *ppb* (parts per billion). As mentioned above, the ultra-pure water was used to clean the glassware and STM cells as well as to prepare the electrolytes.

## 3.2 Gold Sample Preparation

For structural studies on metal surfaces, it is essential that single-crystal surfaces are prepared in a reproducible manner.<sup>[77,123,167]</sup> Prior to each experiment, the surface must be prepared to have a clear and similar starting point. For all the experiments shown in this study, commercially available single-sided polished single-crystal Au(111) electrodes with an orientation of  $< 1^\circ$  and a surface roughness of  $\leq 0.03 \text{ }\mu\text{m}$  were used. A simple flame annealing method was sufficient to remove surface carbon and organic impurities from the electrode surface<sup>[2,96,98]</sup> and produce the thermally reconstructed Au(111) surface (See Section 2.1.3).<sup>[10,99]</sup> The relatively simple annealing technique is also able to heal relatively minor surface defects because of the higher mobility of atoms at such high temperatures. Different crystal dimensions and annealing parameters were used for the electrochemical (EC) and the *in-situ* STM measurements:

**EC sample:** A small crystal with a diameter of 4 mm, connected to a gold wire loop for easier handling, was used in the electrochemical measurements (See Section 3.3). The crystal was annealed for 2 min. at a reasonably high temperature (red crystal glow) using a Bunsen burner flame. The crystal should continuously be moved through the flame to avoid excessive heating and its successive melting. The crystal was then directly transferred to the electrochemical glass cell where it was cooled above the electrolyte surface in an atmosphere of  $\text{N}_2$  for about 1 minute.<sup>[77,168]</sup>

***In-situ* STM sample:** A larger crystal with a diameter of 12 mm and a height of 2 mm served as the sample for *in-situ* STM measurements. Prior to each measurement, the crystal was initially annealed in a muffle furnace at  $960^\circ\text{C}$  for 2 hours then

cooled down slowly in the furnace (in air) overnight. This leads to a significant increase in width of the gold terraces. Terraces with a width of around 400 nm were usually observed using STM. The crystal was later annealed to an orange colour in a hydrogen or a butane flame for 5 min. and then cooled to room temperature in a stream of  $N_2$  for 7 min., as shown in Figure 3.1. Again, one must prevent the crystal from melting by moving slowly through the oxidizing zone of the flame and back again. In addition, one should avoid immersing a hot crystal in a relatively cooler electrolyte as the large temperature gradient could quench the sample and destroy its crystalline structure.<sup>[90]</sup>

It should be noted that while imaging the surface at positive potentials, the oxidation of the gold surface must be avoided by continuously compensating for the potential shift of the pseudo-reference electrode (especially with measurements of higher pH values. For a Au(111) electrode, the onset of gold surface oxidation takes place at around 1.2 V in 0.1 M  $H_2SO_4$  (not shown in Figure 2.8). The surface of an oxidized gold electrode contains monoatomic high islands and monoatomic deep holes which cover the whole surface.

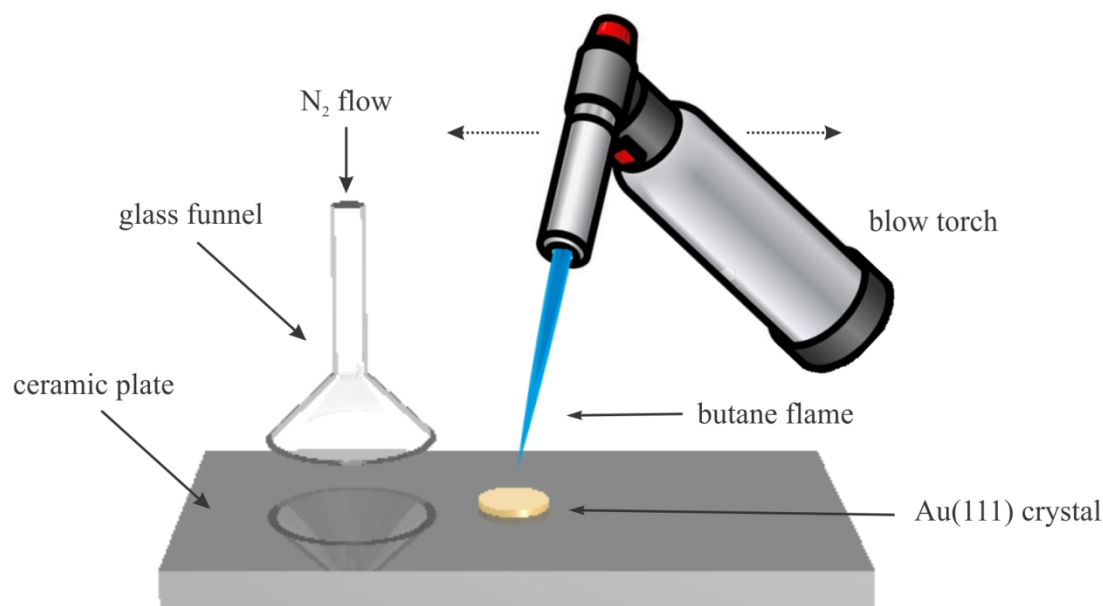


**Figure 3.1:** Schematic representation of the flame annealing, using a butane blow torch, of an STM gold single-crystal.

### 3.3 Cyclic Voltammetry

The potential of a single electrode cannot be measured. Therefore, the potential of the working electrode is applied using a potentiostat and measured against a stable reference electrode. The resulting current dissipates to the counter electrode. As shown in Figure 3.2, a conventional three-electrode glass cell was used to perform cyclic voltammetry measurements at 20 °C. The three distinct compartments accommodated the working, counter and reference electrodes, respectively.

The working electrode was a small Au(111) single-crystal which was prepared using a flame-annealing treatment (see Section 3.2). The quality of the crystal was checked, prior to each measurement by cyclic voltammetry in 0.1 M H<sub>2</sub>SO<sub>4</sub>. The freshly prepared crystal was then thoroughly rinsed and transferred to another electrochemical cell under potential control in a hanging-meniscus configuration.<sup>[169]</sup> This configuration ensures that only current from the polished and oriented upper surface of the electrode is detected.

The counter electrode was either a graphite rod or platinum wire with a surface area that is at least twice that of the working electrode.<sup>[80]</sup> The working and the counter electrodes were separated by means of sintered glass or a frit to avoid the diffusion of undesirable reaction products towards the working electrode. It should be noted that the electrolyte resistance remains unaffected by the frit. A commercially available saturated mercury sulfate electrode (MSE, Schott Instruments) served as the reference electrode. Unless otherwise stated, all the indicated potentials in this work were converted and are referred to the saturated calomel electrode (SCE) scale (SCE = +0.42 V *vs.* MSE)<sup>[126]</sup> for the ease of comparison with literature. In order to minimize the uncompensated ohmic drop across the electrolyte and to prevent any current flow over the reference electrode, the reference electrode was placed in a Luggin-Haber capillary that ended a few millimetres away from the surface of the working electrode.<sup>[170]</sup>

In aqueous systems, the reduction of atmospheric oxygen occurs as a side reaction during electrochemical processes. To prevent this, the electrolyte is usually purged with nitrogen for at least 30 min. before the measurement as well as during the measurement. For all measurements, the negative and positive potential limits were chosen to lie between the hydrogen and oxygen evolution potentials, respectively. The potential was controlled using an *Autolab PG128N* or *HEKA* potentiostat-galvanostat. The detailed method of operation of a potentiostat can be found in literature.<sup>[171]</sup> Basically, the reference electrode is energized so that only the current flow between the working and

counter electrode is detected and plotted against the electrode potential. The digitalized data is stored as an ASCII file for evaluation using the commercially available software *Origin 2017*.

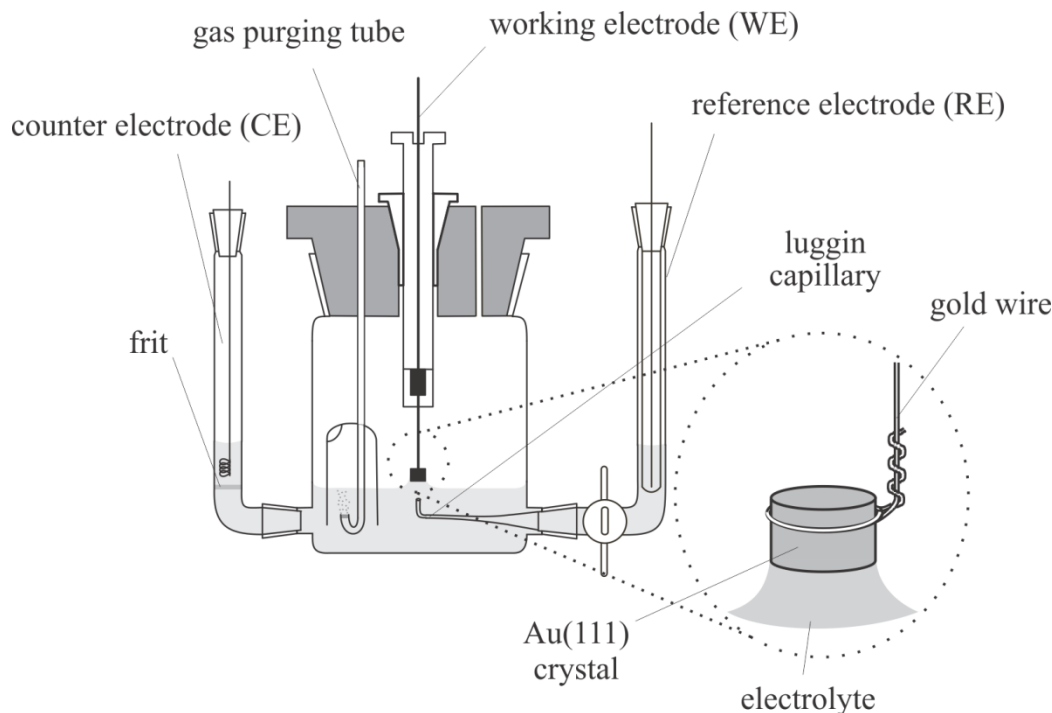


**Figure 3.2:** Schematic representation of a three-electrode glass electrochemical cell with the *hanging-meniscus* set up.<sup>[172]</sup>

### 3.4 *In-situ* Scanning Tunneling Microscopy

In this work, a commercial *Topometrix, Discoverer TMX 2010* STM (Santa Clara, USA) equipped with an electronic controller from *Anfatec* (Oelsnitz, Germany) was used to acquire the *in-situ* STM images. All measurements were performed in the constant-current mode where the resulting images display the topography of the surface, with the brightest areas or spots being the highest. The obtained STM images were analysed using the software *Gwyddion 2.48* and the software *Present* from *Anfatec*. It should be noted that a distance given as that ‘between adjacent rows’ corresponds to the closest *anion-anion* distance between of an imaged adsorbate and not to the perpendicular distances between two adjacent rows. In addition, all mentioned dimensions correspond to the statistical

average of several images which are reproducibly acquired during several measurements. The margin of error is represented as a standard deviation.

### **3.4.1 Instrumentation Set Up and Calibration**

The system is composed of several components: the STM stage, the bipotentiostat and the electronic control unit, which are all connected to one another. The stage contains the sample plate, the STM head with the piezo tube scanner and, optics to aid in the manual approach of the tip to the sample. The sample plate which can be moved using a stepper motor in the x- and y-direction, is found under the scanner head (tube scanner with max. (x, y) scan range:  $810 \times 810 \text{ nm}^2$ , z-deflection:  $0.5 \text{ }\mu\text{m}$ ). Care must be taken when inserting the metallic tip into the tube scanner, otherwise the piezo could break due to excess force and not be able to move continuously anymore. The manual (far/fast) approach of the tip to the sample surface is reached by two setscrews which move in the z-direction and can be monitored using a camera and screen visualization. The electronic (close/slow) approach on the other hand, is controlled by the stepper motor to bring the tip close to the surface until the pre-set tunneling current value is reached.

The bipotentiostat helps set the tip and sample potentials independently from one another, against a pseudo-reference electrode. The electronic control unit controls both the STM stage, including the tip towards the sample, and the bipotentiostat. The control unit is connected to a commercial PC where all necessary parameters are set, and images of the scanned surface are visualized via a user interface (*Anfatec Scan*). The parameters include the tunneling current, the tip and sample potentials, the scan area and the so-called feed-back loop (*Proportional Integral Derivative* (PID)) values. For *in-situ* STM experiments, it can be concluded that successful imaging of large scan ranges requires relatively high voltage bias ( $U_T \geq 250 \text{ mV}$ ) and small tunneling currents ( $I_T \leq 2 \text{ nA}$ ). For atomic resolution imaging on the other hand, smaller voltage bias ( $U_T \leq 50 \text{ mV}$ ) and larger tunneling currents ( $I_T \geq 5 \text{ nA}$ ) are required.

Before starting a set of measurements, it is necessary to calibrate the STM in order to confirm that the atomic distances within an image are correct. This can be done by acquiring atomic resolution images of a relatively well-known electrochemical system such as the adsorption of sulfate on Au(111),<sup>[90]</sup> which is a benchmark measurement as discussed in Section 2.2.4. However, such a measurement is quite time consuming since the surface is more sensitive to contamination. Instead, the internal calibration of the STM in the lateral (x-/y-) direction is often performed by acquiring an atomically

resolved image (Figure 3.3) of a highly oriented pyrolytic graphite (HOPG) sample. The theoretical distance between the bright ‘hills’ of an HOPG substrate in an STM image is  $2.46 \text{ \AA}$ .<sup>[166]</sup> On the other hand, the internal calibration in the vertical (z-) direction is done by measuring the step heights of a metallic substrate in air. For example, the height of a monoatomic step of a Au(111) substrate is around  $0.25 \text{ nm}$  which is slightly smaller than the atomic distance of Au. An acceptable calibration value would lie within a 3-5% error margin, with respect to the theoretical values mentioned above.

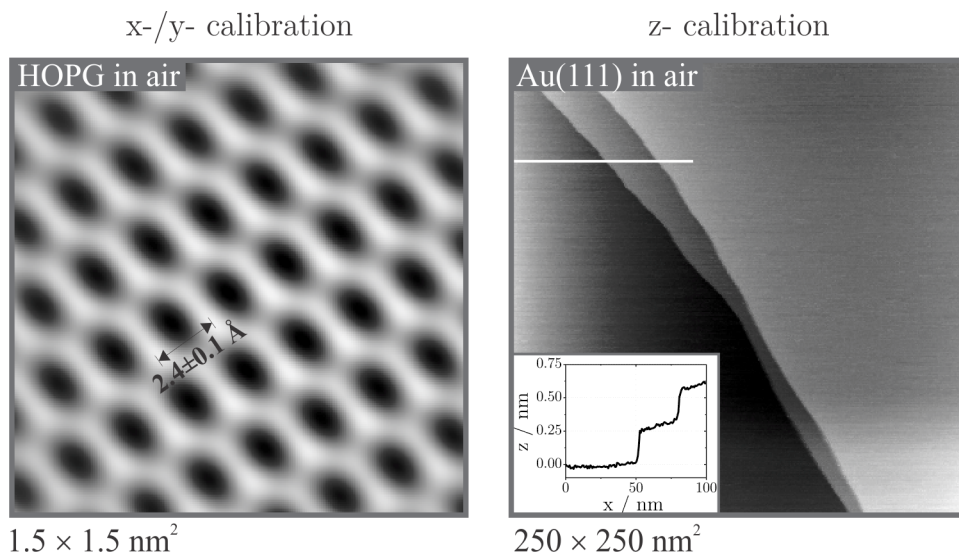


**Figure 3.3:** *In-situ* STM scanner head calibration in the x-/y- and z- directions by performing measurements with HOPG and Au(111) substrates in air, respectively.

STM measurements are very sensitive to electric noise and mechanical vibrations. Therefore, the STM stage is grounded and topped with a cylindrical cover that shields it from electromagnetic influences. In addition, the microscopy unit is isolated from the building vibrations by the means of a triple spring damping set up.<sup>[173–175]</sup> It is recommended that after installing the tip and sample, one tries to reduce the amount of drift in the STM by waiting for around 15 min. before starting the measurement.

### 3.4.2 *In-situ* STM Cell

In order to perform *in-situ* STM measurements, an electrochemical setup should be combined with the basic STM cell setup. Figure 3.4 shows a schematic representation of

the *in-situ* STM cell assembly. The cell was developed and manufactured at Ulm University<sup>[90]</sup> and was made from Kel-F (polytetrafluorethylene) and contained a chemically resistant Kalrez O-ring which acted as a seal to prevent the electrolyte from leaking during a measurement. The working electrode was a cylindrical single-crystal. The freshly prepared sample (see Section 3.2) was placed on a stainless-steel base plate and covered with the cell body.

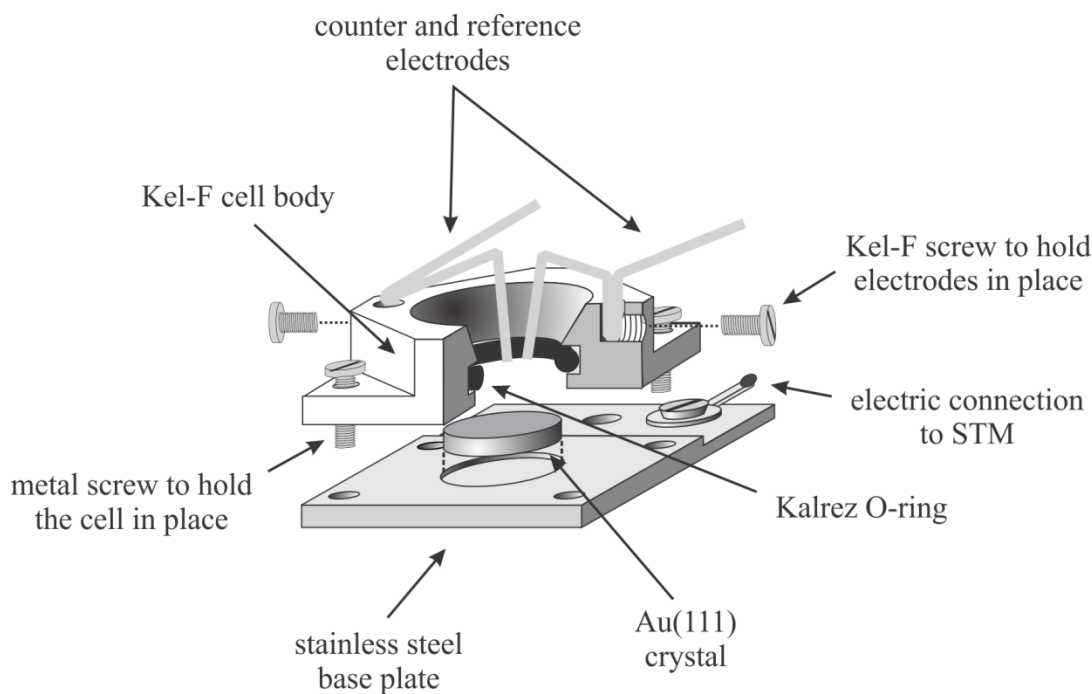


**Figure 3.4:** Schematic representation of an *in-situ* STM cell.<sup>[132]</sup>

Depending on the measurement, a platinum or a gold wire (in the case of formate adsorption) with large surface area served as the counter electrode. A platinum wire served as the pseudo-reference electrode. The ability to image a structure is strongly dependent on the experimental setup and choice of reference electrode. All the potentials at which the STM images were acquired are converted and referred to against the SCE potential. The shift in potential between the pseudo-reference and the standard reference electrode varies with changing the electrolyte (for example,  $E_{\text{Pt}} = +0.55 \text{ V vs. } E_{\text{SCE}}$  in 0.1 M  $\text{H}_2\text{SO}_4$ ). For each electrolyte, the potential shift was measured before and after a measurement. This shift was also compensated during a measurement in order to verify



that the potential region of interest at which an image is acquired, is indeed correct. Both the reference and counter electrodes were annealed in a butane flame and cooled down under a nitrogen stream before being attached to the cell. The assembled cell is then placed on the sample holder and connected to the bipotentiostat where only then, under potential control, the electrolyte was added using a pipette to avoid contamination.

### 3.4.3 STM Tips Preparation

As mentioned in Section 2.3, the quality and resolution of an STM image is strongly dependent on the chemical and physical properties of the scanning tip. Tungsten and platinum/iridium alloys ( $\text{Pt}_{80}\text{Ir}_{20}$  and  $\text{Pt}_{70}\text{Ir}_{30}$ ) were used as tip materials for the measurements. Both materials differ from one another in terms of electrochemical and mechanical stability. The potential stability window of W tips ( $E_{\text{Pt}} = -0.75 \text{ V}$  to  $-0.55 \text{ V}$  in  $0.1 \text{ M H}_2\text{SO}_4$ ) compared to that of Pt/Ir tips ( $E_{\text{Pt}} = -0.75 \text{ V}$  to  $0.25 \text{ V}$  in  $0.1 \text{ M H}_2\text{SO}_4$ ) is rather small. Nevertheless, W tips result in sharper STM images due to their enhanced mechanical stability. Pt/Ir tips are usually used when a large potential range is to be investigated or when long measurements are expected since W tips oxidize after less than 10 hours of being exposed to air. The geometry of the tip will thus be affected, which significantly influences the measurement.

### Tip Etching

The (atomically) sharp STM tips were obtained by electrochemical anodic etching in an electrolyte lamella.<sup>[176]</sup> A similar apparatus as that shown in Figure 3.5 was used to etch both the W and Pt/Ir tips from polycrystalline wire ( $\varnothing = 0.25 \text{ mm}$ ) of around 4 cm in length. In the case of the W tips, the wire was placed in the centre of an O-ring of Au wire. A lamella from  $2 \text{ M NaOH}$  was then formed and a direct current (DC) voltage of  $2.0\text{--}3.5 \text{ V}$  (depending on the diameter of the Au ring and age of the electrolyte) was applied between the O-ring (cathode) and the wire (anode). As a result, the W wire was electrochemically oxidized where it was in contact with the lamella. After around 15 min., two sharp tips, an upper and a lower one, were completely etched. The lower tip fell in a holder due to gravity and an automatic cut off interrupted the circuit immediately and prevented the additional etching of the upper tip. Both tips were then thoroughly rinsed with water to remove any residual NaOH and stored in isopropanol to hinder their oxidation, until further preparation steps.

In the case of Pt/Ir tips, the wire was placed in the centre of an O-ring of Pt wire and a lamella of 3.4 M NaCN. An alternating current (AC) voltage (50 Hz) of 4.5 V and 4.0 V for Pt<sub>80</sub>Ir<sub>20</sub> and Pt<sub>70</sub>Ir<sub>30</sub> wires was applied, respectively. In addition, the electrolyte lamella was renewed every 2 min. since the resulting Cyano complexes in the electrolyte increase, which slows down the etching process. Again, an upper and a lower etched tip was obtained after around 12 min. of etching time. The lamella was then manually and quickly ‘broken’ in order to avoid excessively etching the upper tip, which could result in a ‘round’ tip. Until the next preparation step, both tips were rinsed with water and stored in a clean beaker filled with water to dilute any adhering CN<sup>-</sup> to the tip.

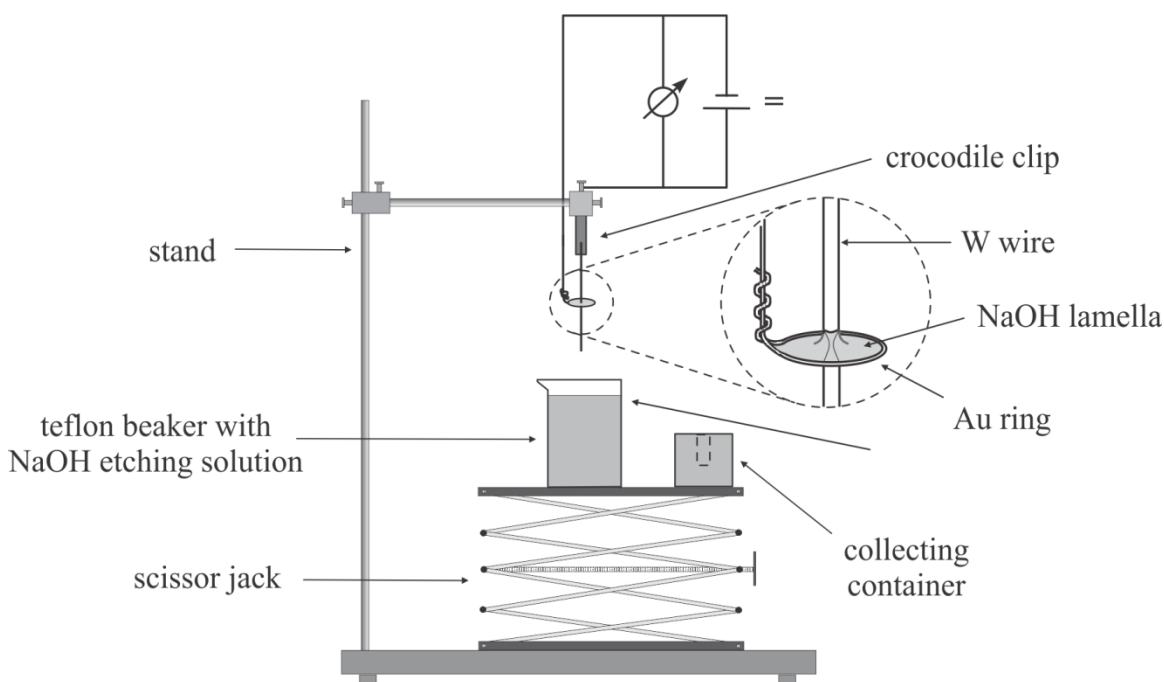


**Figure 3.5:** Schematic representation of the anodic etching apparatus of W tips.<sup>[90]</sup>

## Tip Coating

In order to minimize the Faradaic currents at the STM tip in the electrochemical cell, all but the top most end of the tip must be coated. To do so, an anodic electrophoretic paint that was diluted in ultra-pure water (paint: H<sub>2</sub>O  $\approx$  1:3) was used.<sup>[164]</sup> The tip was attached to a crocodile clip and immersed approximately 4 mm deep in the paint. As shown in the apparatus in Figure 3.6, the etched tip and the platinum plate served as the working and

the counter electrode, respectively. The paint was deposited on the tip by applying a DC voltage between both electrodes. For W tips, a voltage of 80 V for 6 min. was used. For Pt/Ir tips, the voltage was initially 80 V for 4 min. then was reduced step-wise during the coating to 60 V and 40 V for 30 sec. and 90 sec., respectively. The tips were later placed, pointing upwards in a holder and polymerized in a convection oven at 200 °C for 10 min. During this process, the paint contracts slightly and cracks open at the top exposing all but the sharp end of the metallic tip through which the tunneling current could flow (see Section 3.4.3).

With these preparation steps, the leakage currents during the experiment can be reduced to  $< 20$  pA. The final produced tips are highly pure, as well as mechanically and chemically stable, which allows for reproducible sharp imaging quality. It should be noted that unlike recent *in-situ* STM studies which are usually performed in acidic environments,<sup>[177,178]</sup> this work includes measurements performed at  $\text{pH} > 7$ , making it more difficult to image the surface. For such measurements, a well-insulated STM tip, and a contaminant-free cell are paramount.

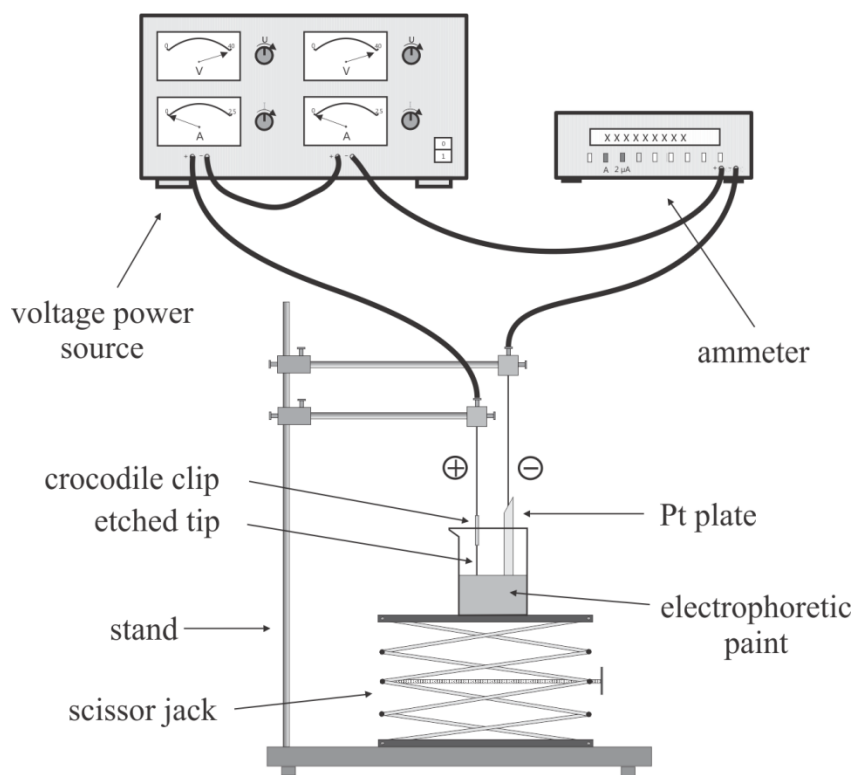


**Figure 3.6:** Schematic representation of the electrochemical coating of the STM tips using an anodic electrophoretic paint.<sup>[90]</sup>

### 3.5 Materials and Chemicals

As mentioned in Section 3.1, all electrolytes were prepared using ultra-pure water. To ensure the cleanliness of the investigated systems and to minimize the influence of unknown contaminants, the purest commercially available chemicals were used. When possible, voltammetric profiles (characteristic potentials and peak/spike heights) of the individual systems were compared to those found in literature. All chemicals were used as they are without additional purification steps. Table 3.1 and Table 3.2 respectively show a list of all the chemicals and the materials that were used in this work.

**Table 3.1:** List of the used chemicals.

Chemical	Producer	Purity	Usage
H <sub>2</sub> SO <sub>4</sub>	Merck, Darmstadt	commercial, 95%	caroic acid
H <sub>2</sub> O <sub>2</sub>	Merck, Darmstadt	30%	caroic acid
NaOH	Merck, Darmstadt	>99%	STM tip etching
NaCN	Sigma-Aldrich, Seelze	>97%	STM tip etching
Lacquer ZQ 84-3225	BASF, Ludwigshafen	-	STM tip coating
CH <sub>3</sub> COOH	Sigma-Aldrich, Seelze	99.999%	electrolyte
H <sub>2</sub> SO <sub>4</sub>	Merck, Darmstadt	96% Suprapur	electrolyte
H <sub>3</sub> PO <sub>4</sub>	Merck, Darmstadt	95% Suprapur	electrolyte
HClO <sub>4</sub>	Merck, Darmstadt	70% Suprapur	electrolyte
HCOOH	Merck, Darmstadt	98-100% Suprapur	electrolyte
LiOH	Sigma-Aldrich, Seelze	≥99.995%	electrolyte
NaH <sub>2</sub> O <sub>4</sub>	Sigma-Aldrich, Seelze	≥ 99.999%	electrolyte
Na <sub>2</sub> HPO <sub>4</sub>	Sigma-Aldrich, Seelze	≥ 99.999%	electrolyte
Butane C <sub>4</sub> H <sub>10</sub>	EDCO, Eindhoven	Comm. Highest Purity	crystal annealing
Nitrogen N <sub>2</sub>	MTI Industrial Gases, Neu-Ulm	N 6.0	purgung, crystal cooling

**Table 3.2:** List of the used materials.

Material	Producer	Purity	Usage
W wire	MaTecK, Jülich	99.95%	tip etching
Au wire	MaTecK, Jülich	99.995%	tip etching
Pt <sub>80</sub> Ir <sub>20</sub> wire	MaTecK, Jülich	99.99%	STM tip material
Pt <sub>70</sub> Ir <sub>30</sub> wire	MaTecK, Jülich	99.99%	STM tip material
Pt plate	MaTecK, Jülich	99.99%	tip etching
Pt wire, 1.0 mm	MaTecK, Jülich	99.99%	tip coating
Pt wire, 0.5 mm	MaTecK, Jülich	99.99%	RE & CE
Au wire	MaTecK, Jülich	99.99%	CE
Kel-F	Polytetra GmbH, Mönchengladbach	Comm. Highest Purity	STM cell material
Kalrez O-ring	Isolast GmbH	-	STM cell seal
Au(111) crystals	MaTecK, SPL	99.99%	WE



## 4 Electrochemical Behaviour of Au(111) in 0.1 M H<sub>2</sub>SO<sub>4</sub>: New Insights

Although the current-potential curve of a Au(111) electrode in sulfuric acid can provide information about the structure of a surface, it does not properly monitor the continuous progress of surface reconstruction. It is possible to use electrocatalytic reactions to establish relations between electrocatalytic activity and structural changes. The hydrogen evolution reaction (HER) is chosen to probe the progress of changes in potential-induced surface reconstruction, since it (i) is one the simplest structure sensitive reactions, (ii) takes place in the negative potential region, and (iii) involves H<sub>ad</sub> as an intermediate, which is essentially not stable and hence does not accumulate on the Au surface.

### 4.1 Potential Dependence on Surface Reconstruction

The electrocatalytic activity of the thermally reconstructed Au(111) surface for the HER at a constant potential (-0.485 V) is fairly constant (Figure 4.1, brown curve). After stepping the potential to values positive of the *pzc*, for example 0.415 V where the surface reconstruction is lifted due to the specific adsorption of (bi)sulfate anions, and later stepping to -0.185 V (Figure 4.1, blue curve) or 0.115 V (Figure 4.1, green curve) where potential-induced surface reconstruction takes place, the current densities are again stable. Due to the increase in defect density however, the activity is slightly higher (Figure 4.1, blue and green curves) than that of the thermally reconstructed surface.

The HER currents directly after stepping the potential from positive values, where the Au(111)-(1×1)-structure is stable, to -0.485 V, were used to monitor the process of potential-induced surface reconstruction. Compared to the activity of the reconstructed surface, the unreconstructed surface (Figure 4.1, pink curve) shows roughly double the activity. Unexpectedly, a constant HER activity is observed indicating that the typical

potential-induced reconstruction does not take place in the course of one hour. Otherwise, the current ought to have halved. The activity shows however, that the (1×1)-structure is markedly more active than the reconstructed ( $\sqrt{3} \times 22$ ) structure. Additionally, structural changes in the HER region at -0.485 V are observed to be frozen or rather slowed down.<sup>[30]</sup>

To study the potential-induced surface reconstruction of Au(111), a simple potential step program (experiments performed by J. M. Hermann) at two different reconstruction potentials (-0.185 and 0.115 V) was used, where the probing potential was -0.485 V in the HER regime (Figure 4.1, blue and green curves). In this way, the process of potential-induced reconstruction was probed as a function of time and potential, by the HER.

For both reconstruction potentials, an exponential decay with time in the HER currents at -0.485 V is observed (Figure 4.1). The current values do not reach those of the thermally reconstructed surface. Most likely, this is due to the increase in order and hence, the decrease in defect density of the thermal-induced reconstruction compared to the potential-induced reconstruction. Interestingly, the kinetics of surface reconstruction were observed to be strongly influenced by the electrode potential. The process is much faster ( $\sim 30$  times) at 0.115 V compared to that at -0.185 V. Although the physical reason for this behaviour is still unclear, the potential difference relative to the *pzc* seems to play a role. This is in agreement with previously reported *in-situ* STM studies which stated that reconstruction lines instantaneously appear at potentials close to the lifting of the surface reconstruction.<sup>[30]</sup> The reconstruction phenomenon of surface atoms is observed to be potential-dependent.<sup>[104,179]</sup>

Noticeably, at the different potentials, the stable structures formed after long waiting times vary in terms of morphology (STM images in Figure 4.1) yet have very similar HER activities.<sup>[30]</sup> At more negative potentials, parallel lines (with fewer elbows) are observed, whereas at more positive potentials, a herringbone structure is observed. It is worth mentioning that distinct types of reconstruction structures, herringbone-like or parallel rows, have previously been reported for different thermal annealing temperatures.<sup>[96]</sup> Although elbows serve as one type of defect which is commonly known to act as nucleation centres for metal deposition for example, the similar activity with the significant difference in the number of elbows indicates that elbows compared to other defect sites, are not significantly more active for the HER. These findings show that combining electrocatalysis with *in-situ* STM imaging is an efficient way to study the potential dependence of surface reconstruction.



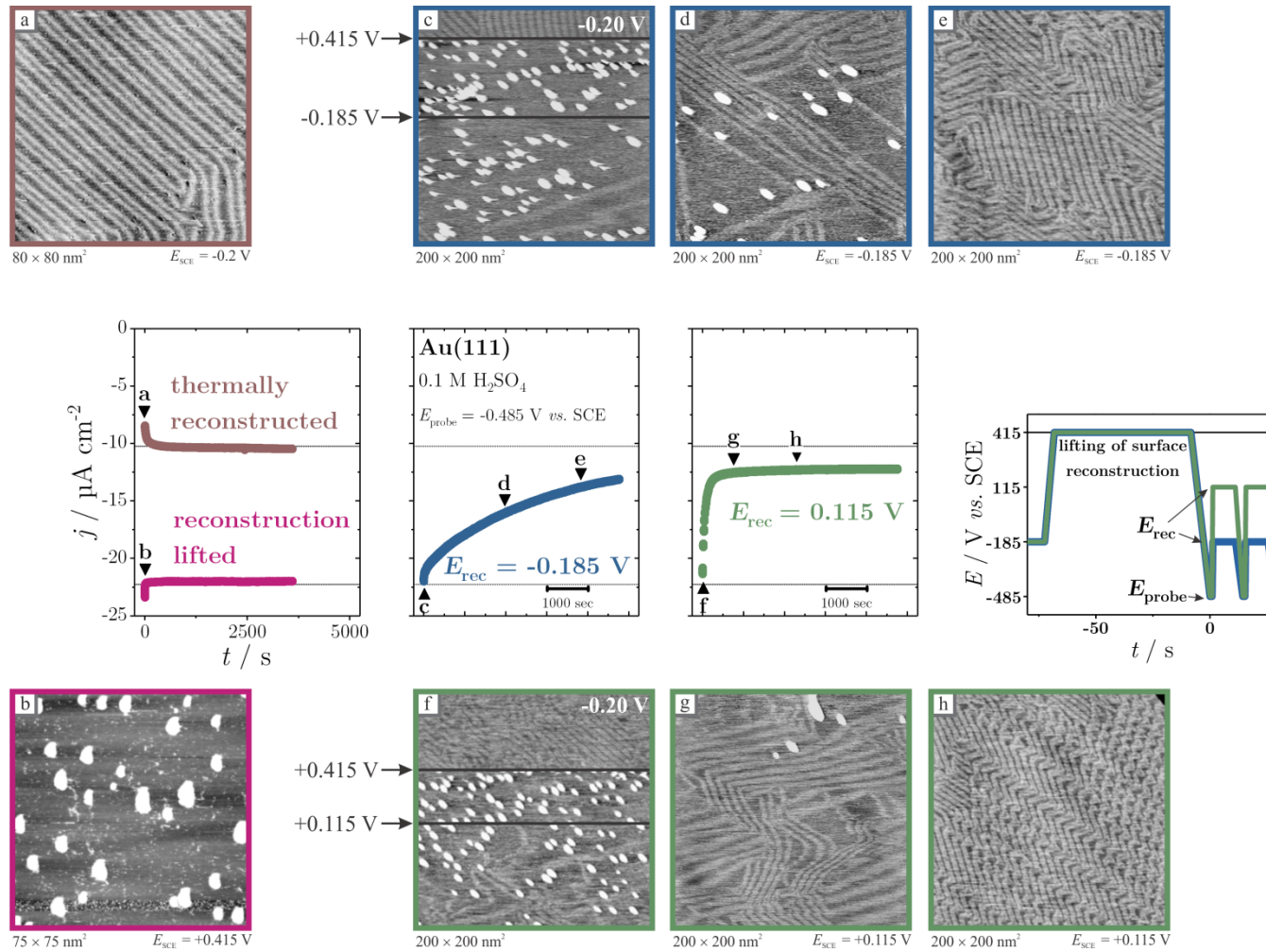


**Figure 4.1:** Potential-step time series of the HER activity for Au(111) in 0.1 M H<sub>2</sub>SO<sub>4</sub> at -0.485 V. The *in-situ* STM images illustrate surface structures: (a) thermally reconstructed Au(111) surface recorded after flame-annealing upon immersion at -0.2 V, 80×80 nm<sup>2</sup> (b) Au(111)-(1×1) right after stepping to 0.415 V, 75×75 nm<sup>2</sup>, (c-e) potential-induced formation of the reconstructed surface after lifting the reconstruction and stepping back to -0.185 V, 200×200 nm<sup>2</sup>, and (f-h) 0.115 V, 200×200 nm<sup>2</sup>. Here, the HER is used to monitor structural changes of the Au(111) surface.<sup>[30]</sup>

## 4.2 Distinct Adsorbed Sulfate Structures (S-I, S-II and S-III)

Positive of the phase transition spike in the current-potential curve of a Au(111) electrode in 0.1 M H<sub>2</sub>SO<sub>4</sub> (Figure 2.8), a structure of parallel rows of adsorbed sulfate with a  $(\sqrt{3} \times \sqrt{7})R19.1^\circ$  structure is known to form.<sup>[1,7-9]</sup> Unexpectedly, it is observed that directly after a potential step to 0.85 V not only one, but rather three different structures appear on the surface. Figure 4.2 shows an *in-situ* STM image (scan direction top to bottom) of the three distinct ordered sulfate structures (S-I, S-II and S-III) which consist of parallel rows that form on the terraces of the unreconstructed Au(111) surface.

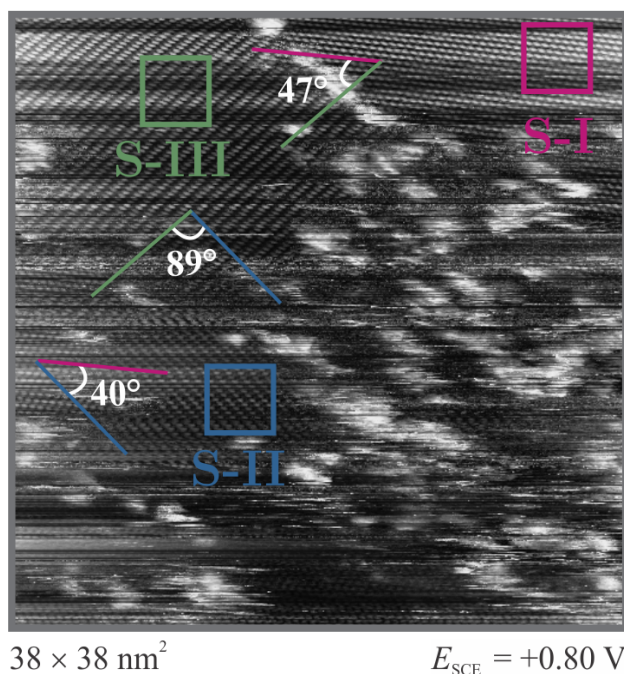


**Figure 4.2:** *In-situ* STM image of Au(111) in 0.1 M H<sub>2</sub>SO<sub>4</sub> showing the appearance of three distinct sulfate structures S-I, S-II and S-III: 38×38 nm<sup>2</sup>,  $E = 0.85$  V,  $U_T = 0.5$  V,  $I_T = 3$  nA.

Initially, all three structures appear to be of short range. Structures S-I and S-III are first observed at the top of the STM image. Interestingly, the final structural order of sulfate on the surface differs from its structural rearrangement right after the potential jump (not shown). The first two structures (S-I and S-II) transform into structure S-III, which seems to be the most favourable and stable structure. This was observed after zooming into one of the structures and zooming out again to image the larger scan area.

Unfortunately, the time dependence of the structural transitions has not been recorded since the initial aim of these experiments was to (i) check the quality of the Au(111) crystal, (ii) check the cleanliness of the system and (iii) calibrate the STM. Nevertheless, it is worth mentioning that the observed behaviour is reproducible and has been imaged in several measurements.

High-resolution *in-situ* STM images of the three distinct structures S-I, S-II, and S-III of adsorbed sulfate on Au(111) are shown in Figure 4.3a, b and c, respectively. For the sake of clarity, the dimensions of the structures are given in Table 4.1 as follows: the nearest distances separating two sulfates along a row ( $d_1$ ) and between the adjacent rows ( $d_2$ ), the enclosing angles ( $\alpha$ ), and the coverage  $\theta_{\text{sulfate}}$ . The *in-situ* STM images indicate that for all three structures, one type of maxima which can be ascribed to sulfate is clearly seen. Based on the experimental data, structural models are proposed where the oxygen atoms of the  $\text{SO}_{4\text{ad}}$  are bound in a tridentate configuration to the top sites of the Au(111) surface atoms.

In the case of structure S-I (Figure 4.3a), the sulfate-sulfate distances are  $\sim \sqrt{3}$  times the Au-Au distance of 2.89 Å in the Au(111)-(1×1) unit cell.<sup>[91]</sup> The enclosing angle is an indication of the underlying Au(111) substrate's symmetry direction and a strong hint towards a commensurate structure. A hexagonally close packed ( $\sqrt{3} \times \sqrt{3}$ ) structure where the sulfate species are situated in the  $[11\bar{2}]$  direction of the Au(111) unit cell, is proposed. The structure correlates with  $\theta_{\text{sulfate}}$  of 0.33 ML where the coverage is defined on the basis of the number of bare Au atoms within the unreconstructed Au(111)-(1×1) surface unit cell. At the electrode potential where the maximum adsorption of sulfate takes place, theoretical studies have also reported a  $(\sqrt{3} \times \sqrt{3})R30^\circ$  structure of sulfate on a Au(111) surface,<sup>[136]</sup> which was later verified by LEED under electrochemical conditions in 0.5 mM  $\text{H}_2\text{SO}_4$ .<sup>[135]</sup>

In the case of structure S-II (Figure 4.3b), the sulfate-sulfate distances and enclosing angle do not quite fit characteristic Au-Au distances. Therefore, in order to resemble a commensurate structure where every  $\text{SO}_{4\text{ad}}$  adsorbs on a top site of Au, the unit cell is relatively large. A  $(5\sqrt{3} \times 4)$  structure is proposed, where a  $\theta_{\text{sulfate}}$  of  $\sim 0.25$  ML is calculated and the  $\text{SO}_{4\text{ad}}$  species are situated again, in the  $[11\bar{2}]$  direction of the Au(111) unit cell. Assuming that the STM images are correctly interpreted, it is probable that both structure S-I and S-II resemble metastable structures which are too dense to fit a coadsorbed hydronium ion between the imaged parallel rows. Only when the distances are large enough does the thermodynamically stable  $(\sqrt{3} \times \sqrt{7})R19.1^\circ$  structure form with a

$\theta_{\text{sulfate}}$  of 0.2 ML. In this case, the H<sub>3</sub>O<sup>+</sup> surface cations coadsorb with sulfate in a 1:1 ratio to stabilize the structure, as shown in Figure 4.3c.

**Table 4.1:** Averaged sulfate-sulfate distances along ( $d_1$ ) and between ( $d_2$ ) the rows, as well as the measured enclosing angles ( $\alpha$ ) and total  $\theta_{\text{sulfate}}$  coverages obtained from *in-situ* STM images of a Au(111) electrode in 0.1 M H<sub>2</sub>SO<sub>4</sub> of structures S-I, S-II and S-III of adsorbed sulfate.

Structure	$d_1 / \text{\AA}$	$d_2 / \text{\AA}$	$\alpha / ^\circ$	$\theta / \text{ML}$
S-I	4.8±0.4	5.2±0.3	64±3	0.33
S-II	4.2±0.4	6.2±0.6	74±4	0.25
S-III	4.6±0.3	7.3±0.4	75±3	0.22

The fact that distinct adsorbed sulfate structures (with different rotation angles) are imaged is puzzling. At this moment, one can only attribute this observation to experimental conditions. Most *in-situ* STM studies report an ordered structure at least 50 mV more positive than the phase transition potential (0.85–0.92 V *vs.* SCE).<sup>[1,9]</sup> As confirmed by this study (Section 2.2.4), only the  $(\sqrt{3} \times \sqrt{7})R19.1^\circ$  structure is observed in that case. At the proximity of the phase transition spike ( $\sim 0.8$  V *vs.* SCE) however, different structures tend to form. The physical origin of this anomalous behaviour can be attributed to several factors: (i) kinetic hindrance at the proximity of the phase transition spike which can be related to the role of the cationic H<sub>3</sub>O<sup>+</sup> species in stabilizing the structure, (ii) surface quality and chemical purity which could cause the less thermodynamically stable structures (S-I and S-II) to be more easily imaged, (iii) lack of impurities due to the better quality of ultra-pure water used, and (iv) better control in the potential shift of the pseudo-reference since now, compared to previously reported data, a current-potential curve of the Au(111) electrode could be recorded during STM image acquisition without losing potential control. Unfortunately, it has been more than a decade since *in-situ* STM images of sulfate on Au(111) have been last reported, which makes it extremely difficult of compare these observations to state-of-the-art studies. With this in mind, more systematic measurements are required in order to help fully understand the information provided by the *in-situ* STM images in Figure 4.3.

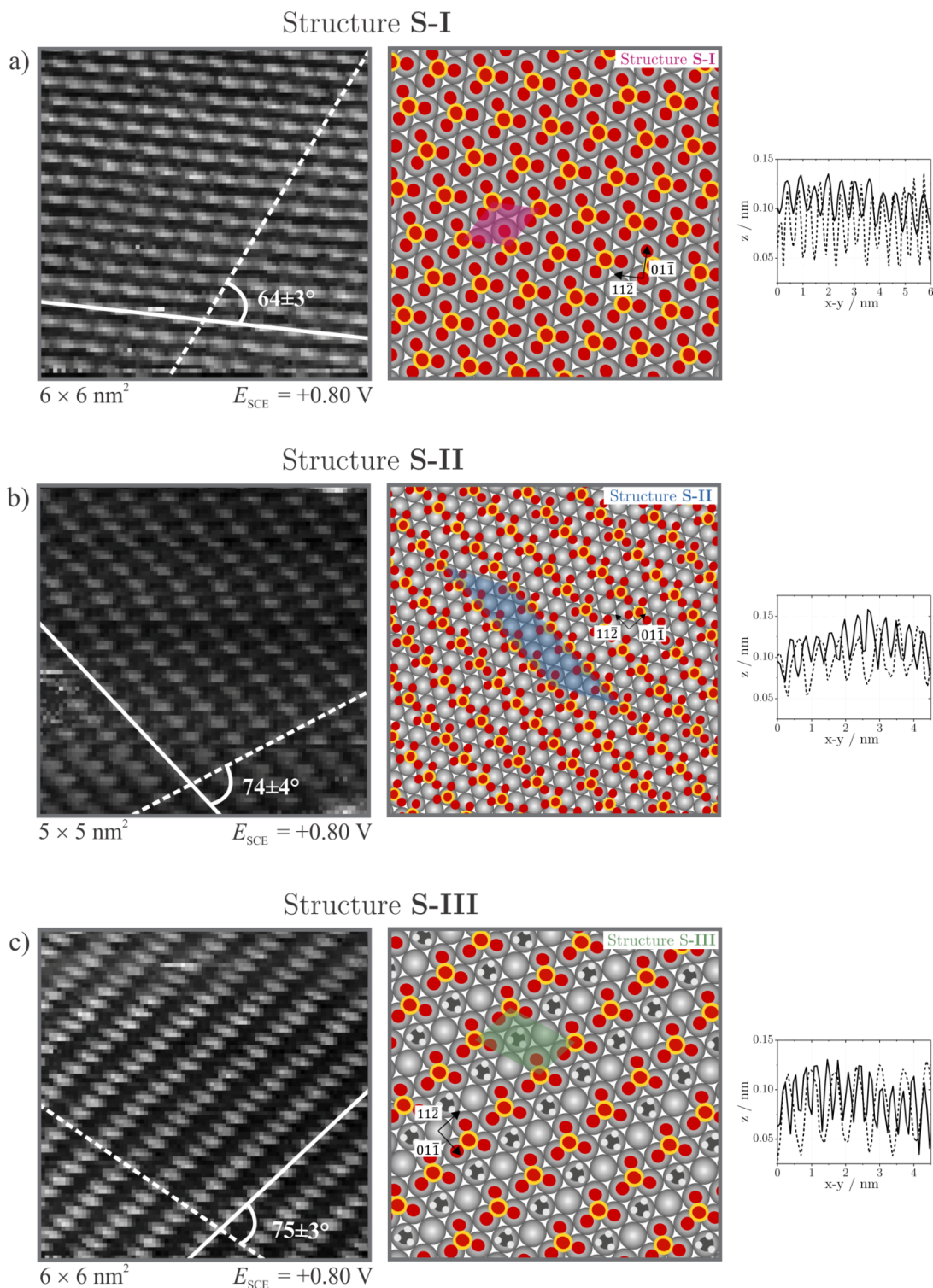


**Figure 4.3:** *In-situ* STM images indicating three different sulfate structures for Au(111) in 0.1 M  $\text{H}_2\text{SO}_4$ :  $E = 0.80 \text{ V}$ ,  $U_{\text{T}} = 0.5 \text{ V}$ ,  $I_{\text{T}} = 3 \text{ nA}$ , where (a)  $6 \times 6 \text{ nm}^2$ , (b)  $5 \times 5 \text{ nm}^2$ , and (c)  $6 \times 6 \text{ nm}^2$ , represent structure S-I, S-II & S-III, respectively. The proposed models and the height profiles of key features in each structure and is represented alongside each STM image.



## 5 Adsorption of Carboxylates

It is expected that acetate and formate adsorb on the Au(111) surface in a similar manner. Unlike formate, acetate is not reactive on gold<sup>[51]</sup> which makes it easier to image an adsorbed structure at a molecular level and under electrochemical conditions. More insight on formate adsorption can be gained by studying the adsorption of its neighbouring carboxylate such as acetate. The findings for adsorbed acetate and formate on Au(111) are compared and conclusions regarding the expected adsorption behaviour for other carboxylates in the homologous series are drawn.

### 5.1 Au(111) in Acetic Acid

The electrochemical behaviour of Au(111) in an acetic acid electrolyte is first investigated, followed by *in-situ* STM imaging the characteristic features in the current-potential curve.

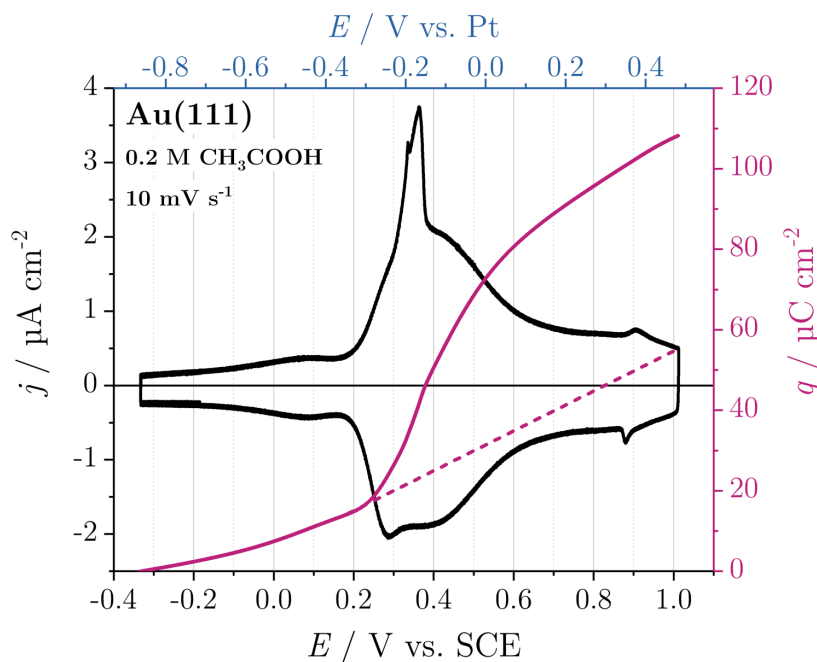
#### 5.1.1 Electrochemical Behaviour

Figure 5.1 shows a typical current-potential curve (second cycle) for Au(111) in 0.2 M CH<sub>3</sub>COOH (pH 2.7) at a scan rate of 10 mV s<sup>-1</sup>. The current-potential curve very much resembles that obtained for Au(111) in sulfuric acid. It is evident that acetate on Au(111) acts as a typical specifically adsorbing anion. In other words, the reconstructed ( $\sqrt{3} \times 22$ )-Au(111) surface which is stable in the negative potential region, is transformed to an unreconstructed (1×1)-structure due to the adsorption of acetate at around 0.3–0.4 V.

At around 0.9 V, a characteristic small peak indicating a phase transition in the adsorbed adlayer is observed. For the acetate adlayer, the stability region is constrained by the onset of surface oxidation controlled by the electrolyte's pH. The solution pH of this system is around 2.7 (Figure 5.1). Increasing the pH to 4 or 5 would lead to a shift in the surface oxidation of Au(111) to more negative potentials, resulting in a stronger overlap between OH and acetate adsorption.<sup>[180]</sup> This would make the *in-situ* STM imaging



of the acetate adlayer on the Au(111) surface very difficult or even impossible. It should be noted that in the presence of  $\text{HClO}_4$  in solution,<sup>[51]</sup> which is often used as a base electrolyte to establish pH 1, this characteristic peak had escaped detection. This could be due to the OH adsorption currents which mask the phase transition peak. However, the peak is seen in the presence of  $\text{HClO}_4$  at higher scan rates of  $1 \text{ V s}^{-1}$ , particularly in the negative scan (not shown).



**Figure 5.1:** Current-potential curve (black) of a Au(111) electrode in 0.2 M  $\text{CH}_3\text{COOH}$  at 20 °C. Scan rate:  $10 \text{ mV s}^{-1}$ .<sup>[52]</sup> Also shown is the measured potential *vs.* Pt pseudo-reference electrode (blue) and anodic charge density *vs.* potential curve (pink). The dashed (pink) line shows the estimation for double-layer charging.

Figure 5.1 also shows the anodic charge density *vs.* potential plot. The curve is typical for anion adsorption and greatly resembles that for formate adsorption<sup>[50]</sup> and sulfate adsorption,<sup>[35]</sup> obtained from chronocoulometry, on Au(111). The adsorption isotherms for acetate on Au(111) (from a voltammetric scan at  $50 \text{ mV s}^{-1}$ , not shown), corrected for double-layer charging (at the potential region of 0.1 V–0.2 V negative of acetate adsorption), enables the coverage of acetate to be estimated for the Au(111) electrode. Using a charge density of  $222 \text{ } \mu\text{C cm}^{-2}$  for the transfer of one electron per Au



surface atom (deprotonation of acetic acid), the total acetate coverage  $\theta_{\text{acetate}}$  of around 0.25 ML, at the potential of the phase transition, reaches a value similar to that of formate on Au(111).<sup>[50]</sup>

### 5.1.2 *In-situ* STM Imaging

An *in-situ* STM image of a thermally-annealed Au(111) electrode after immersion in 0.2 M CH<sub>3</sub>COOH at 0.15 V, is shown in Figure 5.2a. The image clearly shows that the well-known ( $\sqrt{3} \times 22$ ) reconstruction is stable in the presence of acetic acid in solution in the negative potential region just before the onset of acetate adsorption. As the electrode potential is stepped to 0.85 V, the surface reconstruction is lifted, allowing monoatomic high gold islands to appear on the surface (Figure 5.2b). The measurements indicate that the size of the islands, which grow via Ostwald ripening,<sup>[181–183]</sup> is around  $6 \pm 2$  nm and occupy a surplus of  $\sim 4\%$  of reconstruction atoms. The islands on the Au(111) electrode in the presence of acetic acid increase in number and are nearly half the size of those imaged in the presence of sulfuric acid.<sup>[178]</sup> The islands' formation and/or development appear to be affected by the nature of the anions in solution and perhaps by the mobility of surface atoms. The smaller sizes of the island along with the more pronounced triangular shapes show a reduced mobility of surface atoms in the presence of acetate compared to sulfate. Interestingly, the critical size of the islands appears too small to for an adsorbed structure to form on its surface. The cause of such an observation remains uncertain and will be systematically investigated in another study.

If the potential is stepped back to the negative potential region, potential-induced reconstruction causes reconstruction lines to form. The structure of the lines evolves differently depending on the exact potential. The structure at 0.15 V (Figure 5.2b) contains more herringbone-like features such as elbows, than at -0.1 V (Figure 5.2c). The islands arising from the earlier lifting of the reconstruction are assumed to act as defect sites where these elbows are formed. It has been observed that the surface reconstruction process is much faster at 0.15 V compared to that at -0.1 V. The shape of structure, either herringbone or parallel rows, as well as its kinetics, depends on the potential difference of the electrode relative to the potential of onset of acetate adsorption, and possibly to the *pzc*. For Au(111) electrodes in the presence of sulfate and perchlorate under electrochemical conditions, a similar potential dependence for surface reconstruction has been reported,<sup>[29,30]</sup> as discussed in Section 4.1. It is likely that for anion-covered electrodes, the mobility of surface atoms demonstrates potential-dependence.

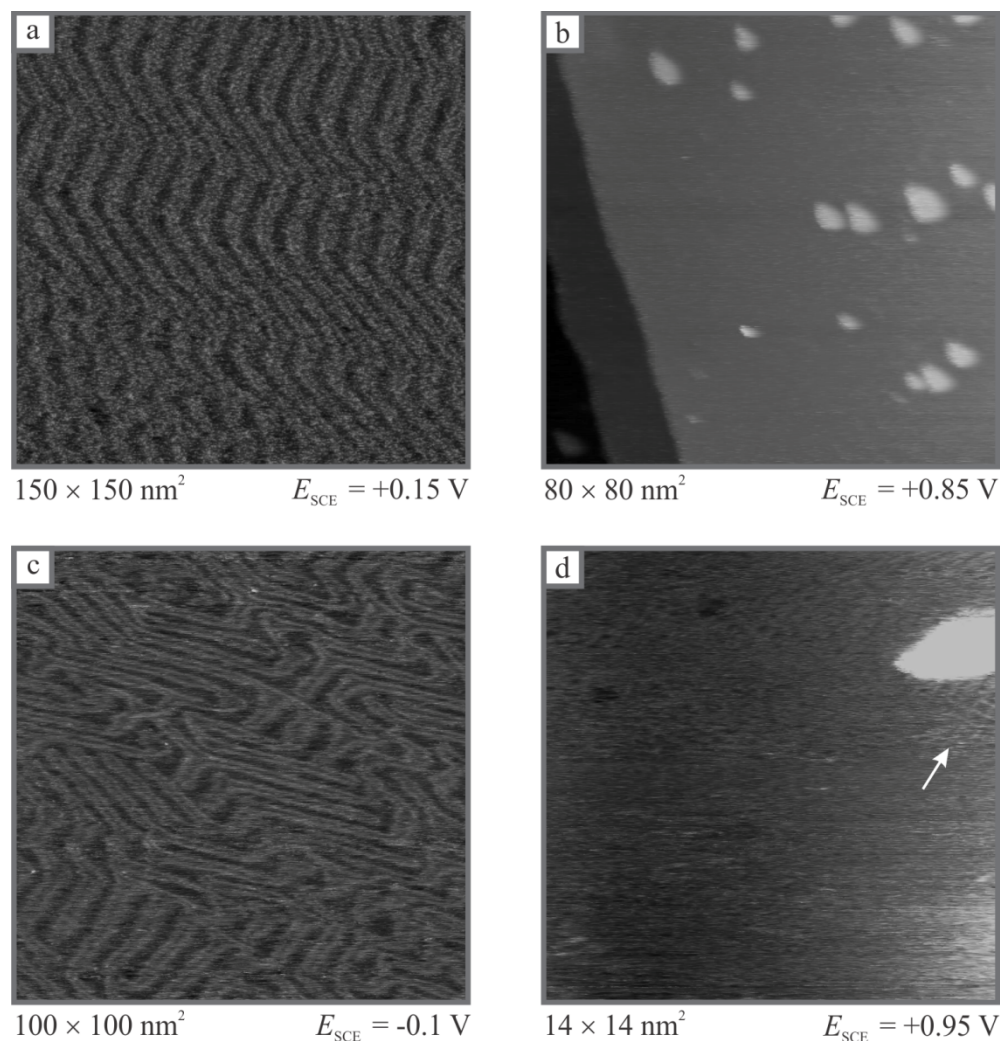


**Figure 5.2:** *in-situ* STM images of Au(111) in 0.2 M  $\text{CH}_3\text{COOH}$  showing the Au(111) (a)  $(\sqrt{3} \times 22)$  surface reconstruction at potentials closer to the *pzc*:  $150 \times 150 \text{ nm}^2$ ,  $E = 0.15 \text{ V}$ ,  $U_T = 0.3 \text{ V}$ ,  $I_T = 2 \text{ nA}$ , (b)  $(1 \times 1)$  surface after lifting of reconstruction, before phase transition:  $80 \times 80 \text{ nm}^2$ ,  $E = 0.85 \text{ V}$ ,  $U_T = 0.3 \text{ V}$ ,  $I_T = 2 \text{ nA}$ , (c) surface reconstruction after stepping back to a negative potential away from the *pzc*:  $100 \times 100 \text{ nm}^2$ ,  $E = -0.1 \text{ V}$ ,  $U_T = 0.2 \text{ V}$ ,  $I_T = 2 \text{ nA}$  and (d) initial formation of acetate structure positive of the phase transition peak:  $14 \times 14 \text{ nm}^2$ ,  $E = 0.95 \text{ V}$ ,  $U_T = 0.4 \text{ V}$ ,  $I_T = 2 \text{ nA}$ .<sup>[52]</sup>

Similar to other specifically adsorbing anions, the adsorption of acetate causes the lifting of the surface reconstruction of Au(111). So far, as in the case of sulfate adsorption (Section 2.2.4), no adlayer structure of acetate has been imaged negative of the phase transition peak (0.92 V).<sup>[9,50]</sup> At more positive potentials (0.95 V) however, ordered adlayer structures have been imaged. It should be noted that the structures initially formed on

the electrode surface with very low coverage at the edges of Au islands, as indicated with an arrow in Figure 5.2d.

### 5.1.3 Transition of Adsorbed Acetate Structures with Time

A unique behaviour is observed positive of the phase transition peak (0.92 V), similar to the case of sulfate adsorption on Au(111). Two distinct ordered structures of parallel zigzag chains sequentially form on the terraces of the unreconstructed Au(111) surface (acetate structures A-I and A-II). Interestingly, the distribution of acetate on the surface right after the potential step, differs from its final structural order. Previously, zigzag chains have also been observed for acetate on Cu(110) using STM under UHV conditions.<sup>[39]</sup> In contrast, random adsorption has been proposed for acetate adsorption on Pt(111) electrodes at both high and low coverages.<sup>[184]</sup>

Initially, structure A-I completely covers the electrode surface and appears to be of short range, as shown Figure 5.3a (scan top to bottom). The structure gradually transforms into structure A-II (Figure 5.3a-d). The time dependence of the extracted coverages, from the *in-situ* STM images for the two different structures, is shown in Figure 5.4. While imaging at 0.95 V for 20 min, structure A-II becomes dominant on the terraces after around 10 min. and slowly grows to form long range domains of around 60 nm in size whilst the metastable structure A-I vanishes, as clearly seen in Figure 5.3d. The measurements indicate that the formation of the thermodynamically stable structure A-II is most probably triggered by structure A-I appearing first on the surface after stepping to potentials positive of the adlayer phase transition peak. Both structures are rotated at an angle of  $23^\circ \pm 3^\circ$  with respect to each other. This angle is not characteristic of the direction of the underlying Au atoms which could be an indication that the structure is probably stabilized by coadsorbed water.

Interestingly, neither structure has been observed on the monoatomic high Au islands. Assuming that the islands have a perfect triangular shape, a minimum of around 5- and 28-unit cells of structure A-I and A-II, respectively, can form on a fully-grown island. Since a rather small number of unit cells can form for structure A-I, it is highly likely that they do not form whatsoever because of the relatively high mobility of surface atoms. Therefore, if according to the observation that structure A-II only forms after structure A-I, neither structure can be imaged on the rather small islands. The absence of an ordered structure on the islands could also be an explanation for the small peak intensity at around 0.9 V in the current-potential curve (Figure 5.1).

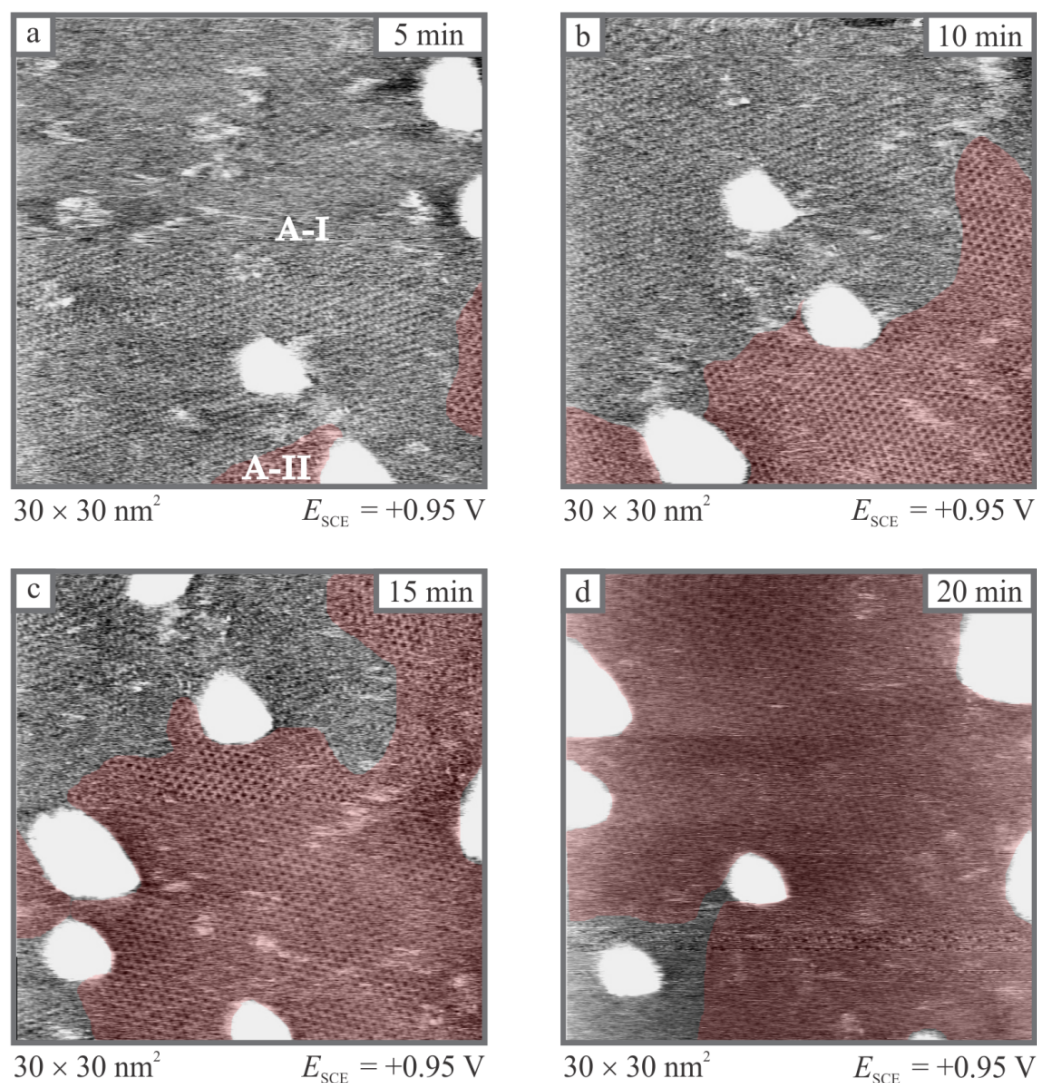


**Figure 5.3:** *in-situ* STM images of Au(111) in 0.2 M CH<sub>3</sub>COOH showing the time dependence on the appearance of two different acetate structures A-I and A-II: 30×30 nm<sup>2</sup>,  $E = 0.95$  V,  $U_T = 0.6$  V,  $I_T = 5$  nA. Structure A-II is highlighted in red. The scan direction is from top to bottom (a-d). The time specifications indicate completion of the individual STM images after stepping the potential to 0.95 V.<sup>[52]</sup>

Findings from electrochemical measurements (not shown) also indicate a slow transformation of the structure. A slight but clear increase in the intensity of the cathodic peak in the negative-going potential sweep is recorded after waiting for 20 min. at a constant potential of the peak. A change in the shape and charge of the peak gives evidence of the higher stability of structure A-II; nonetheless, the charge increase does not completely explain the difference in coverage.

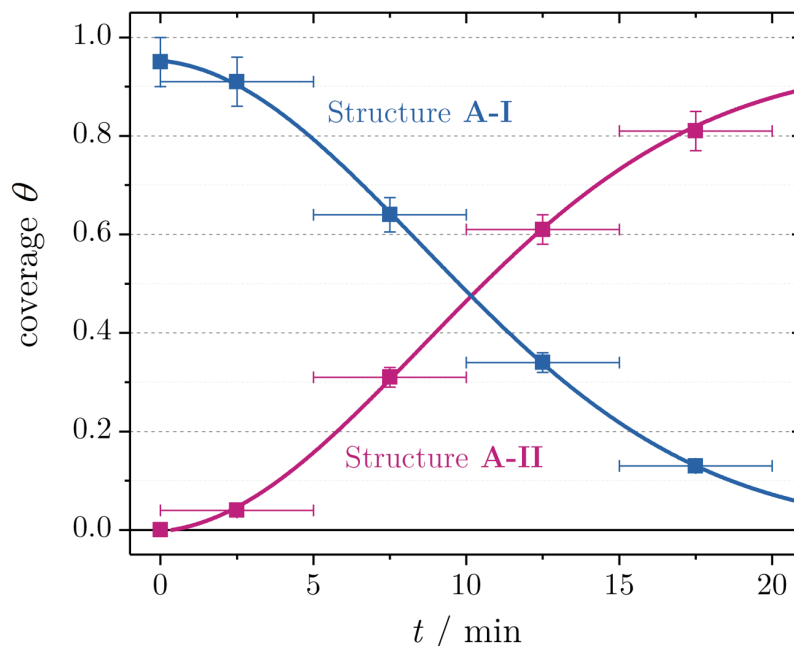


**Figure 5.4:** Plot of the coverage of structure A-I (blue symbols) and structure A-II (pink symbols) of acetate on the Au(111) terrace *vs.* time.<sup>[52]</sup> The blue line represents an empirical fit with an exponential function whose exponent is a 2<sup>nd</sup> order polynomial. The sum of coverages of the blue and the pink lines give a total of 0.95, since around 5 % of the surface is covered with monoatomic high Au islands, on top of which no structure was imaged.

#### 5.1.4 Acetate Structures A-I and A-II: STM Images and Proposed Models

High-resolution *in-situ* STM images of both adsorbed structures, A-I and A-II, helped to determine the arrangement and size of the species on the surface as well as their lattice parameters. Acetate adsorption might take place with either acetate acid or acetate anions as a precursor. As seen in the current-potential curve,  $\text{CH}_3\text{COO}^-$  is in equilibrium with  $\text{CH}_3\text{COOH}$  (Equation 5.1) and it is impossible to settle on whether adsorption takes place simultaneously, or after the deprotonation of  $\text{CH}_3\text{COOH}$ .

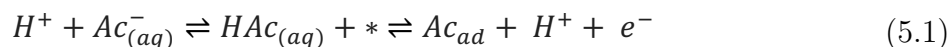
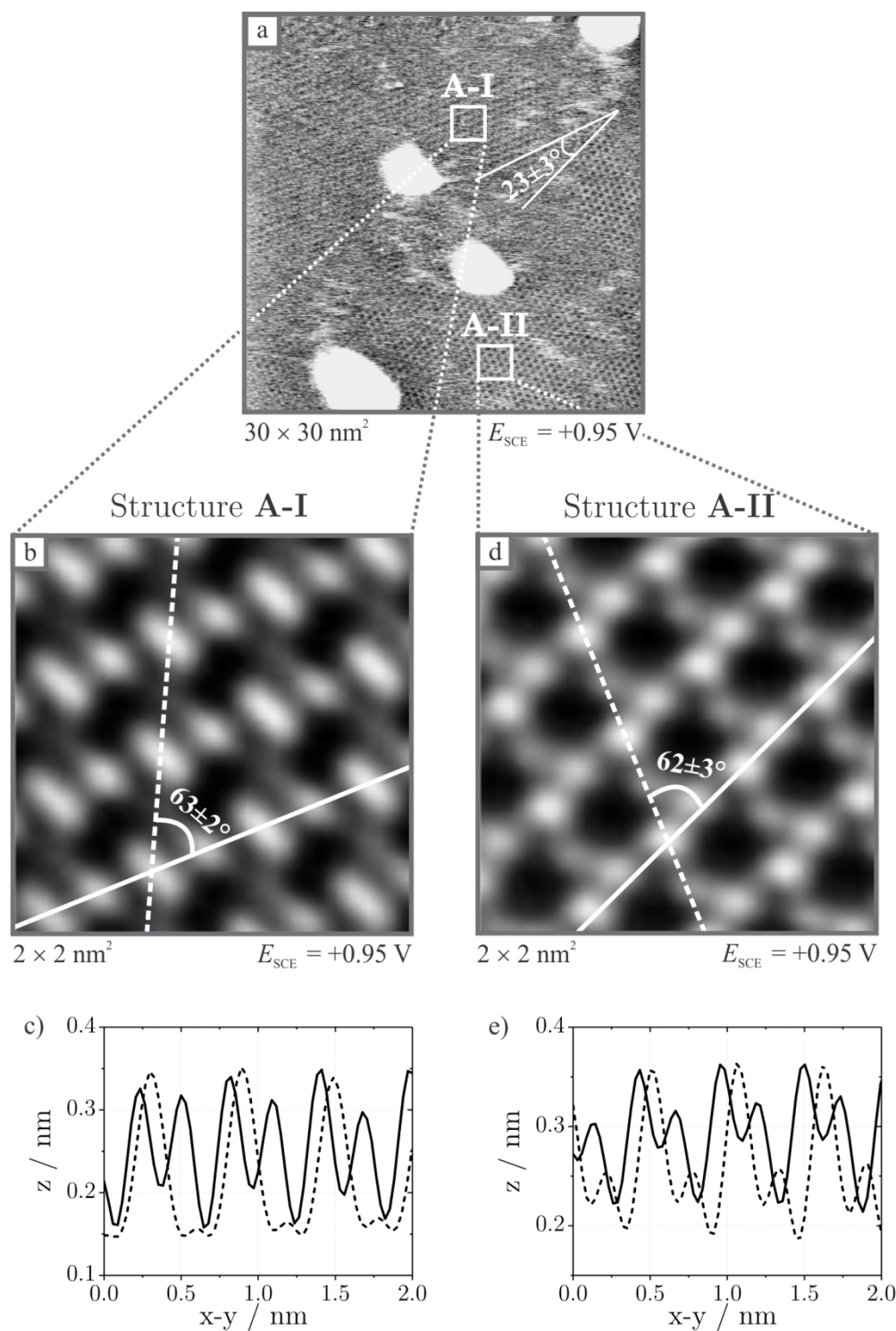


Figure 5.5a represents an *in-situ* STM image that brings out the two distinct structures of acetate on Au(111). For the proposed models of either structure, the bright features in the images are attributed to adsorbed acetate, even though  $\text{CH}_3\text{COOH}$  is the major species in solution.





**Figure 5.5:** *in-situ* STM images of Au(111) in 0.2 M CH<sub>3</sub>COOH indicating (a) two distinct acetate structures, first (b) structure A-I: 2×2 nm<sup>2</sup>,  $E = 0.95 \text{ V}$ ,  $U_{\text{T}} = 0.6 \text{ V}$ ,  $I_{\text{T}} = 5 \text{ nA}$ , where (c) is the height profile of key features along the solid and the dotted lines in (b). Second, (d) structure A-II: 2×2 nm<sup>2</sup>,  $E = 0.95 \text{ V}$ ,  $U_{\text{T}} = 0.6 \text{ V}$ ,  $I_{\text{T}} = 5 \text{ nA}$ , where (e) is the height profile of key features along the solid and the dotted lines in (d).<sup>[52]</sup>

## Structure A-I

The high-resolution *in-situ* STM image of structure A-I indicates that there are two types of intensity maxima, as seen in Figure 5.5b. The first and second maximum will be described shortly and later, respectively, in this section. The first, bright, elongated features have a length of  $3.8 \pm 0.2$  Å, assigned to the length between two oxygen atoms of an acetate anion (from end to end), *i.e.* an individual acetate anion is ascribed to each long bright feature. An individual acetate anion is ascribed to each long bright feature. This shows evidence that acetate adsorbs via the two oxygen atoms binding to two Au surface atoms, *i.e.* in the bidentate configuration. These results support spectroscopic measurements which have indicated that acetate anions prefer to bind to a Au surface in a bidentate configuration, independent of crystal orientation.<sup>[51]</sup> The findings also agree with DFT calculations and STM images acquired for acetate adsorbed on Au(110) under UHV conditions.<sup>[40]</sup> It is not possible however, from the spectroscopic data, to distinguish between specific adsorption sites for the acetate adsorbate. Therefore, the analysis of the high-resolution *in-situ* STM images provides significant information for the preferred arrangement of acetate species on Au(111).

Figure 5.5c shows that the nearest-neighbour distance between two acetate anions in the chain direction is  $5.8 \pm 0.3$  Å, and between the adjacent chains is  $5.9 \pm 0.3$  Å. Furthermore, a  $63 \pm 2^\circ$  enclosing angle is measured. The angle is an indication of the symmetry direction of the underlying Au(111) substrate. The distances however, hint to an incommensurate structure. Because of the greater mobility of the adsorbate, it is quite hard to determine the precise interatomic distances and angles for structure A-I, compared to those of structure A-II, straight from STM image. The distances are slightly larger than 2 times the Au-Au distance of 2.89 Å in the Au(111)-(1×1) unit cell,<sup>[91]</sup> forming a  $(\sqrt{19} \times \sqrt{19})R23.45^\circ$  arrangement with respect to the Au(111) surface. The adlayer structure features acetate anions binding to the surface at various sites in-between top and bridge geometries. The structure correlates with a calculated surface coverage of acetate anions of approximately 0.21 ML, where the coverage is defined on the basis of the number of bare Au atoms within the unreconstructed Au(111)-(1×1) surface unit cell.

The second, bright, round-like feature in Figure 5.5b can be attributed to a coadsorbate that stabilizes adsorbed acetate, possibly via hydrogen bonding. Based on charge considerations, a water molecule, rather than a hydronium cation, most probably stabilizes structure A-I. The process of forming a stable adlayer appears to be slowed down due to the repulsive interactions between the water molecules and the hydrophobic

methyl group. It is possible that time is required until water settles down on the surface and helps convert the metastable structure into a thermodynamically stable one. Such *hydrophobic* interactions are also considered when explaining the differences between the adsorption of formate and acetate.

## Structure A-II

Figure 5.5d represents a high-resolution *in-situ* STM image of structure A-II where again, two types of maxima are observed. The first is related to the brighter features which are  $2.30 \pm 0.04$  Å apart. Each pair of bright features could be a single acetate anion with two oxygen atoms bound to the Au(111) surface. Clearly, this is not the observation for structure A-I. The fact that two oxygen atoms of acetate appear as a single elongated STM feature for structure A-I as opposed to structure A-II, is rather puzzling. It can be explained by assuming that both structures have distinct densities of states, which could be confirmed by theoretical calculations.

Again, a coadsorbed water molecule can be assigned to the second less bright feature. According to the measurements and as shown in Figure 5.5e, the nearest distances separating two acetate anions in the chain direction is  $5.3 \pm 0.3$  Å, and between the adjacent chains is  $5.6 \pm 0.3$  Å. An enclosing angle of  $62 \pm 3^\circ$  is measured. Similarly, the angle is an indication of the underlying Au(111) substrate's symmetry direction. In this case however, the distances are twice the Au-Au distance in the Au(111)-(1×1) unit cell, resulting in a hexagonally close packed (2×2) structure. The acetate anions are situated in the  $[01\bar{1}]$  direction of the Au(111) unit cell. In agreement with the electrochemical measurements mentioned above, the unit cell contains one acetate anion resulting in  $\theta_{\text{acetate}}$  of 0.25 ML.

Based on the experimental data, a simple model for both structures of adsorbed acetate anions on a Au(111) electrode surface has been proposed (Figure 5.6). The model represents the  $(\sqrt{19} \times \sqrt{19})R23.45^\circ$  arrangement of acetate for structure A-I, transforming to the more stable (2×2) arrangement for structure A-II.

Identical well-defined structures for the adsorption of CO from CO-saturated acidic aqueous solutions on Pt(111) have previously been established. On the basis of *in-situ* STM,<sup>[74]</sup> surface X-ray scattering (SXS)<sup>[185–187]</sup> and more recently, *in-situ* second harmonic generation and differential reflectance spectroscopy,<sup>[188]</sup> a  $(2 \times 2)$ -3CO and a  $(\sqrt{19} \times \sqrt{19})R23.45^\circ$ -13CO structure at low and higher potentials, respectively, have been identified.<sup>[186,189]</sup> Furthermore, evidence from *in-situ* Fourier transform IR spectroscopy



showed that the spectrum associated with these structures features bands for on-top and bridge-bonded CO<sup>[190]</sup> which also fits well with the results presented here in this work. Interestingly, no change in the  $(\sqrt{19} \times \sqrt{19})R23.45^\circ$ -13CO ordered structure has been detected using X-ray diffraction,<sup>[191]</sup> leading to the conclusion that this structure can only exist as small domains and does not exhibit a long range order. Furthermore, the coadsorption of water at the Pt(111) interface also leads to a partial shift from on-top to bridge-bonded CO,<sup>[192]</sup> thus providing evidence of the solvent's effect on altering the distribution of sites of an adsorbate in an electrochemical system. The observed structures of carbon monoxide and acetate adlayer on metallic surfaces could be associated with their hydrophobic properties.

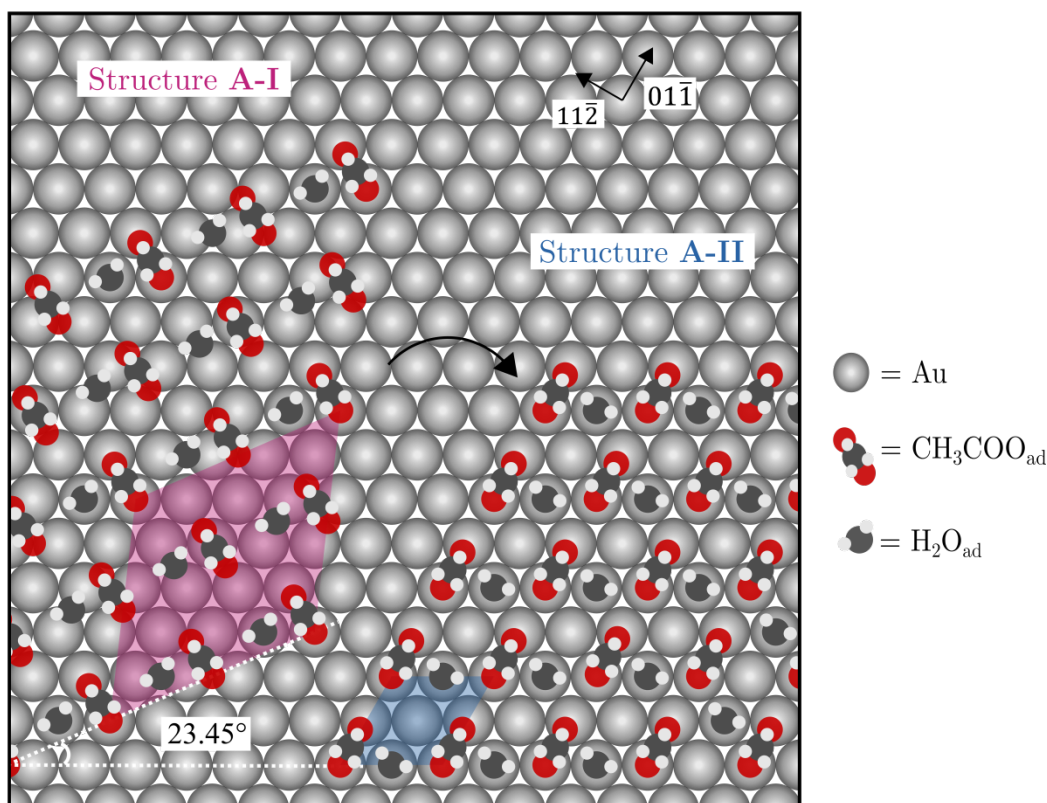


**Figure 5.6:** Model for structures A-I and A-II of acetate on a Au(111) surface in 0.2 M CH<sub>3</sub>COOH. Structures A-I and A-II are represented by a  $(\sqrt{19} \times \sqrt{19})R23.4^\circ$  and a  $(2 \times 2)$  arrangement of anions with respects to the underlying Au(111) surface, respectively. The structures are stabilized by coadsorbed H<sub>2</sub>O molecules.<sup>[52]</sup>

## 5.2 Au(111) in Formic Acid

In the technical sense, the successful *in-situ* imaging of a small absorbed carboxylate such as acetate on the Au(111) surface aided in doing so too for formate. Both acetate and formate have a similar potential stability window and a similar shift with respect to the Pt pseudo-reference electrode being used. The challenges of imaging an ordered adsorbed formate structure is first mentioned. In addition, the electrochemical behaviour of a Au(111) surface in formic acid in the presence of perchloric acid is discussed. Using *in-situ* STM, characteristic features in the current-potential curves of Au(111) in formic acid in the absence (voltammogram not shown) and the presence of perchloric acid is investigated.

### 5.2.1 Electrochemical Behaviour

Three important potential regions have previously been identified for formic acid oxidation on Au(111).<sup>[50]</sup> Figure 5.7 shows a current-potential curve for Au(111) in 0.2 M HCOOH + 0.1 M HClO<sub>4</sub>, where the potential regions are labelled. At negative potentials (region I), the slow adsorption of HCOOH takes place while at more positive potentials (region II), the electrooxidation of HCOOH simultaneously starts with the adsorption of formate which lifts the reconstruction of the Au(111) electrode surface. The hysteresis observed at around 0.4 V, during HCOOH oxidation, could be explained by the reconstruction processes taking place on the surface. The current maximum in the bell-shaped curve represents the highest catalytic activity in this potential region ( $E_{\max}$ ). In the more positive potential limit of region II at around 0.92 V, an abrupt jump or *kink* in HCOOH oxidation currents is observed for both the positive and negative scan. The potential  $E_{\text{kink}}$  and the oxidation current density  $j_{\text{kink}}$  are related to a specific coverage of adspecies species showing a 2D phase transition.

The cathodic charge density *vs.* potential plot is shown in Figure 5.7. Approximate adsorption isotherms for formate on Au(111) (from a voltammetric scan at 50 mV s<sup>-1</sup>, not shown), corrected for double-layer charging (at the potential region of 0.0 V–0.2 V negative of formate adsorption), are calculated to estimate the coverage of formate on the Au(111) electrode. Using a charge density of 222  $\mu\text{C cm}^{-2}$  for the transfer of one electron per Au surface atom, the formate coverage  $\theta_{\text{formate}}$  increases with increasing potential until it reaches a value of around 0.25 ML at the potential of the phase transition.<sup>[50]</sup> The exact value depends on the manner of double-layer correction and an error of around 5%

is accepted. The phase transition is attributed to the adsorption of strongly bound formate adlayer, for which spectroscopic methods have confirmed to be present on gold.<sup>[54,193,194]</sup> Noteworthy is how the charge density *vs.* potential plot for formate adsorption on Au(111) is very similar to that of acetate adsorption on Au(111), discussed above in Section 5.1.1. At the phase transition potential,  $\theta_{\text{formate}}$  reaches a similar value to that of  $\theta_{\text{acetate}}$  on Au(111). The close resemblance in adsorption isotherms for both carboxylates, acetate and formate, supports the suggestion that both acetate and formate could adsorb on Au(111) in a similar manner.

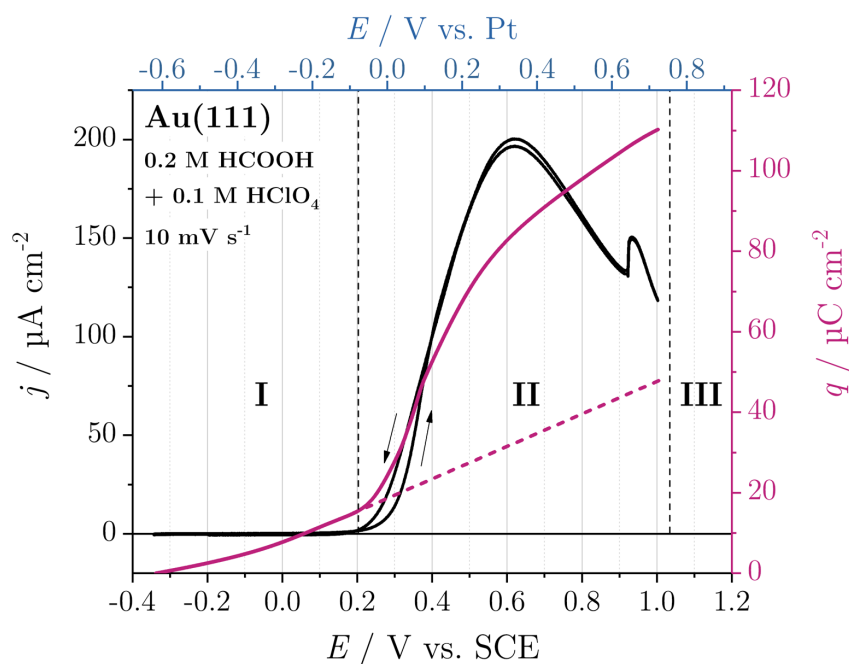


**Figure 5.7:** Current-potential curve (black) of a Au(111) electrode in 0.2 M HCOOH + 0.1 M HClO<sub>4</sub> at 20 °C. Scan rate: 10 mV s<sup>-1</sup>. Also shown, is the measured potential *vs.* Pt pseudo-reference electrode (blue) and cathodic charge density *vs.* potential curve (pink). The dashed (pink) line corresponds to the estimated double-layer charge.

The adsorption of formate inhibits OH adsorption on Au(111) up to around 1.2 V and therefore shifts the onset of gold surface oxidation to more positive potentials, especially for higher HCOOH concentrations. Specifically-adsorbed anions like sulfate on different electrode surfaces, are commonly known to show a very similar behaviour. The current-potential curve in Figure 5.7 is limited in the positive potential region by the

onset of surface oxidation at around 1.5 V (region III). In this potential region, the highest electrocatalytic activity is expected (not shown). Nonetheless, the oxidation of HCOOH on Au is strongly affected by the presence of surface oxides and  $\text{OH}_{\text{ad}}$ .<sup>[195]</sup> Therefore in this work, only regions I and II will be investigated using STM, since significant changes in the surface structure of the Au(111) electrode take place at more positive potentials.<sup>[196]</sup> It should also be noted that the shape of current-potential curves of a Au(111) electrode in the absence of  $\text{HClO}_4$  (not shown) and in its presence (Figure 5.7) is very similar in terms of both the potentials at which characteristic surface processes occur and the magnitude of current densities. The only difference is the shape of the bell-shaped curve in region II.  $\text{HClO}_4$  is commonly used in aqueous solutions of electrochemical systems as a supporting electrolyte. On the one hand, it enhances the electrolyte conductivity by increasing the number of proton donors in solution, which stabilizes the electrolyte pH in very acidic solutions. On the other hand, its anion  $\text{ClO}_4^-$  has minimal influence on electrocatalytic reactions and on gold electrodes, is considered to adsorb weakly (non-specifically).<sup>[1,197]</sup> Nonetheless, the studies on the adsorption properties of  $\text{ClO}_4^-$  ions are rather limited and to a great extent, controversial. Some studies have argued that  $\text{ClO}_4^-$  adsorbs on Au(111) with a full charge transfer<sup>[198,199]</sup>, while others have shown the coverage of perchlorate  $\theta_{\text{perchlorate}}$  on Au(111) to be quite small, ranging from 0.04 ML<sup>[199,200]</sup> up to 0.15 ML.<sup>[201]</sup> This discrepancy could arise due to either the adsorption process being disturbed by the simultaneous reconstruction of the Au(111) or by the electrooxidation of HCOOH and the competitive coadsorption of  $\text{HCOO}_{\text{ad}}$ . Therefore, studying the influence of  $\text{ClO}_4^-$  ions on the adsorption of  $\text{HCOO}^-$  ions on the Au(111) surface, would be beneficial to gain insight on the adsorption of either anion.

### 5.2.2 *In-situ* STM Imaging

It is expected that at potentials positive of  $E_{\text{kink}}$ , an ordered structure of formate forms on the Au(111) electrode surface. Ordered structures of formate on Cu(111), under UHV conditions with different  $\theta_{\text{formate}}$  of up to 0.25 ML, have already been reported.<sup>[202]</sup> Under electrochemical conditions though, the ongoing formic acid oxidation reaction strongly hampers the imaging of formate on active metallic surfaces. Meaning, the formic acid oxidation currents, in the potential region where formate adsorption takes place, are much larger (for slow scan rates) than capacitive and pseudo-capacitive currents for the charging of the electric double-layer and the adsorption of ions, respectively. It is therefore crucial to ensure adequate experimental conditions, by having good tip insulation and

electrode surface quality. As a measure of surface quality, a cyclic voltammogram of a Au(111) STM crystal in a formic acid electrolyte of relatively high concentration ( $> 50$  mM) is first recorded. A *clear* step-up in current is only observed for electrodes with good surface quality, having large and well-ordered Au(111) terraces. In addition, it is important to guarantee a suitable HCOOH concentration. Lower concentrations exhibit reduced Faraday currents in the STM cell, nevertheless a slight step-up in current. If the concentration is too low however, both the surface oxidation and the phase transition overlap with one another, making it extremely challenging to image a structure. Therefore, relatively higher concentrations ( $> 100$  mM) are chosen since they demonstrate a clear step-up in current and shift the surface oxidation to more positive potentials.

*In-situ* STM imaging indicates that the Au(111) surface after thermal annealing and immersion into 0.2 M HCOOH in the presence and absence of  $\text{HClO}_4$  at around 0.1 V, shows the well-known herringbone structure (not shown). In addition, the oxidation of formic acid is not observed on the reconstructed surface. Similar to the behaviour of Au(111) in acetic acid, the reconstruction is stable in the negative potential region where no specific anion adsorption occurs. After stepping the electrode potential to 0.5 V (slightly more positive than the hysteresis observed in the voltammogram in Figure 5.7), the surface reconstruction is lifted due to formate adsorption, where monoatomic high Au islands appear on the surface (not shown). Most probably and like the in the case of sulfate and acetate, the adsorption of formate lifts the Au(111) surface reconstruction.<sup>[203]</sup> As expected, formate behaves as a typical specifically adsorbing anion. At more positive potentials (0.6–1.0 V), the Au(111)-(1 $\times$ 1) seems to be catalytically active, making it challenging to image an adsorbed formate structure in parallel.

### 5.2.3 Formate Structure F-I

Figure 5.8a and Figure 5.8b represent an *in-situ* STM image and its 2D-FFT, respectively, of a Au(111) electrode in 0.2 M HCOOH positive of the phase transition at around 0.95 V. An ordered structure of parallel zigzag chains is observed, which is here named structure F-I. Similar to the case of acetate adsorption, zigzag chain-like structure have been reported for formate adsorption on Cu(110) using STM under UHV conditions.<sup>[39]</sup> It is assumed that the maxima in the STM images in Figure 5.8b represent  $\text{HCOO}_{\text{ad}}$ . The height profiles along the maxima found in the *in-situ* STM images are shown in Figure 5.8c. Two important aspects are observed. First, the height of the maxima in case of the adsorption of formate anions on Au(111) (Figure 5.8c) are almost two times larger than

those in the case of the adsorption of acetate anions (Figure 5.5e). Assuming either anion binds in a perpendicular bidentate configuration, it is expected that the height of an acetate anion would be larger than that of a formate anion. Since this is not the case, it is probable that: (i) formate does not solely bind to the surface in the perpendicular bidentate configuration and that (ii) compared to formate, acetate lies flatter on the surface due to its hydrophobic CH<sub>3</sub> group.

Second, the nearest-neighbour distances between two formate anions in the row direction is  $8.5 \pm 0.4$  Å, and between the adjacent chains is  $9.7 \pm 0.5$  Å. The distances correspond to around  $3d$  and  $2\sqrt{3}d$  of Au surface atom diameters, respectively. While considering an enclosing angle of  $88 \pm 2^\circ$ , a  $(3 \times 2\sqrt{3})$  structure, with respect to the underlying Au(111)-(1×1) surface, is suggested. A simple model for the structure of adsorbed formate on Au(111) is shown in Figure 5.8d. The structure is clearly different to that obtained for the adsorption on acetate anions on Au(111). Nonetheless, like the acetate anions, the formate anions adsorb on the surface along the  $[01\bar{1}]$  direction of the Au(111) unit cell. In the structural model, twelve Au surface atoms correspond to an integer number of bidentate formate  $\text{HCOO}_{\text{ad}}^{\text{B}}$ , which corresponds to  $\theta_{\text{formate}}$  of around 0.08 ML. Compared to what is expected from the total anionic charge obtained from the electrochemical measurements discussed above in this section, 3 formate species are supposed to adsorb in 1 unit cell. Most likely only strongly bound formate species are detected by *in-situ* STM. It is probable that the additional charge results from the adsorption of other formate species (either strongly or slightly less bound, in different or the same configuration). These species can be assigned to the local maxima observed in Figure 5.8b, which have previously escaped detection by *in-situ* STM.<sup>[50]</sup> Either that two additional formate species, instead of one, cover the Au atoms but are not clearly seen in the image, or that the absence of HClO<sub>4</sub> in solution results in a slightly lower coverage since as mentioned above, the non-specific adsorption of ClO<sub>4</sub><sup>-</sup> could result in a  $\theta_{\text{perchlorate}}$  of up to 0.15 ML.<sup>[201]</sup>

Based on what is observed so far, it is possible to provide insight on the rather controversial mechanism of formic acid electrooxidation. Formate species of different configurations could also adsorb on Au(111). Strongly bound  $\text{HCOO}_{\text{ad}}^{\text{B}}$  which is not reactive, accumulates on the Au surface and blocks sites which reactive formate species could adsorb onto. This is one reason for the decrease in the current densities at potentials more positive to  $E_{\text{max}}$ . Noteworthy is the fact that different binding configurations of adsorbed formate have been reported on a Ag(111) surface.<sup>[204]</sup> In

addition, DFT studies have identified that it is possible that  $\text{HCOO}_{\text{ad}}^{\text{M}}$  binds to bridge sites on  $\text{Cu}(hkl)$  surfaces. Nonetheless, the perpendicular geometry of formate species in the monodentate configuration shows slightly higher energy compared to those in the bidentate configuration.<sup>[205,206]</sup>

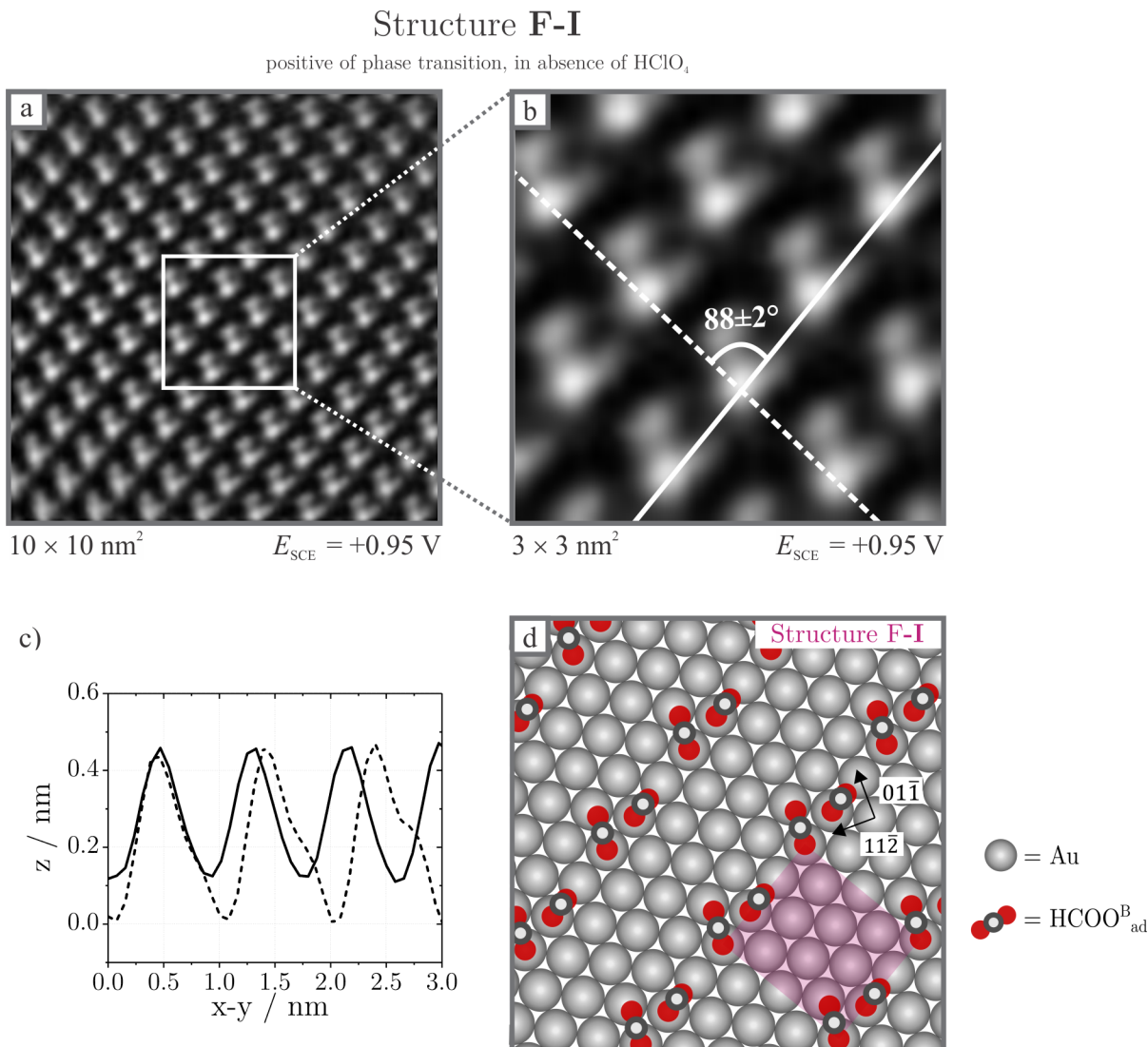


**Figure 5.8:** (a-b) *in-situ* STM images of Au(111) in 0.2 M  $\text{HCOOH}$ , indicating the structure F-I of formate, first (a)  $10 \times 10 \text{ nm}^2$ ,  $E = 0.95 \text{ V}$ ,  $U_{\text{T}} = 0.65 \text{ V}$ ,  $I_{\text{T}} = 8 \text{ nA}$ , where (b) is a crop out and 2D-FFT of (a), and (c) is the height profile of key features along the solid and the dotted lines in (a). (d) Model for structure F-I of adsorbed formate on Au(111) represented by a  $(3 \times 2\sqrt{3})$  arrangement of anions.

### 5.2.4 Influence of the Presence of HClO<sub>4</sub> on the Adsorption of Formate

Figure 5.9 shows that structures of parallel chains were also observed on the Au(111) electrode in 0.2 M HCOOH + 0.1 M HClO<sub>4</sub>, negative and positive of the phase transition. Compared to the system without HClO<sub>4</sub>, the Au(111)-(1×1) surface is surprisingly less stable, making it difficult to image a structure, as clearly seen in Figure 5.9.

#### Structure F-II

Negative of the phase transition peak at around 0.8 V (Figure 5.9a), structure F-II is imaged. The nearest-neighbour distances between two formate anions in the row direction is  $15.9 \pm 0.8$  Å, and between the adjacent chains is  $26.0 \pm 1.4$  Å. In addition, an enclosing angle of  $79 \pm 5^\circ$  is measured (Figure 5.9b and c). A distance of around 2.3 nm between the adjacent rows, was previously reported.<sup>[50]</sup> The distances correspond to around  $2\sqrt{7}d$  and  $9d$  of Au surface atom diameters, respectively, which suggest a  $(2\sqrt{7} \times 9)$  structure of adsorbed formate, with respect to the underlying Au(111)-(1×1) surface.

#### Structure F-III

With increasing potential, the formate structure becomes denser and forms a different structure (structure F-III). Positive of the phase transition peak at around 0.95 V, zigzag chains are imaged (Figure 5.9d). Interestingly, zigzag chain-like structures are observed at potentials positive of the phase transitions, for different carboxylates.<sup>[40,52,207]</sup> The nearest-neighbour distances between two formate anions in the chain direction is  $7.5 \pm 0.7$  Å, and between the adjacent chains is  $8.6 \pm 0.5$  Å. In addition, an enclosing angle of  $87 \pm 3^\circ$  is measured (Figure 5.9e and f). Structure F-III corresponds to a  $(\sqrt{7} \times 3)$  structure. These findings strongly suggest that the formate anions, with and without the presence of perchloric acid, and like acetate anions, are situated in the  $[01\bar{1}]$  direction of the Au(111) unit cell. Although the addition of HClO<sub>4</sub> is expected to only influence the ionic strength and the reactivity (slightly), a clear change in the adsorbed structure is also observed. It would have been extremely beneficial to identify the angle by which both structures F-II and F-III are rotated by with respect to one another. Unfortunately, the structure of the underlying Au(111) surface was not imaged during this measurement. This is usually done by stepping back with the potential to a region where the (1×1)-structure is stable. It should also be noted that both structures were imaged on different areas of the crystal and it would be misleading to quantify such a rotation from the images in Figure 5.9.



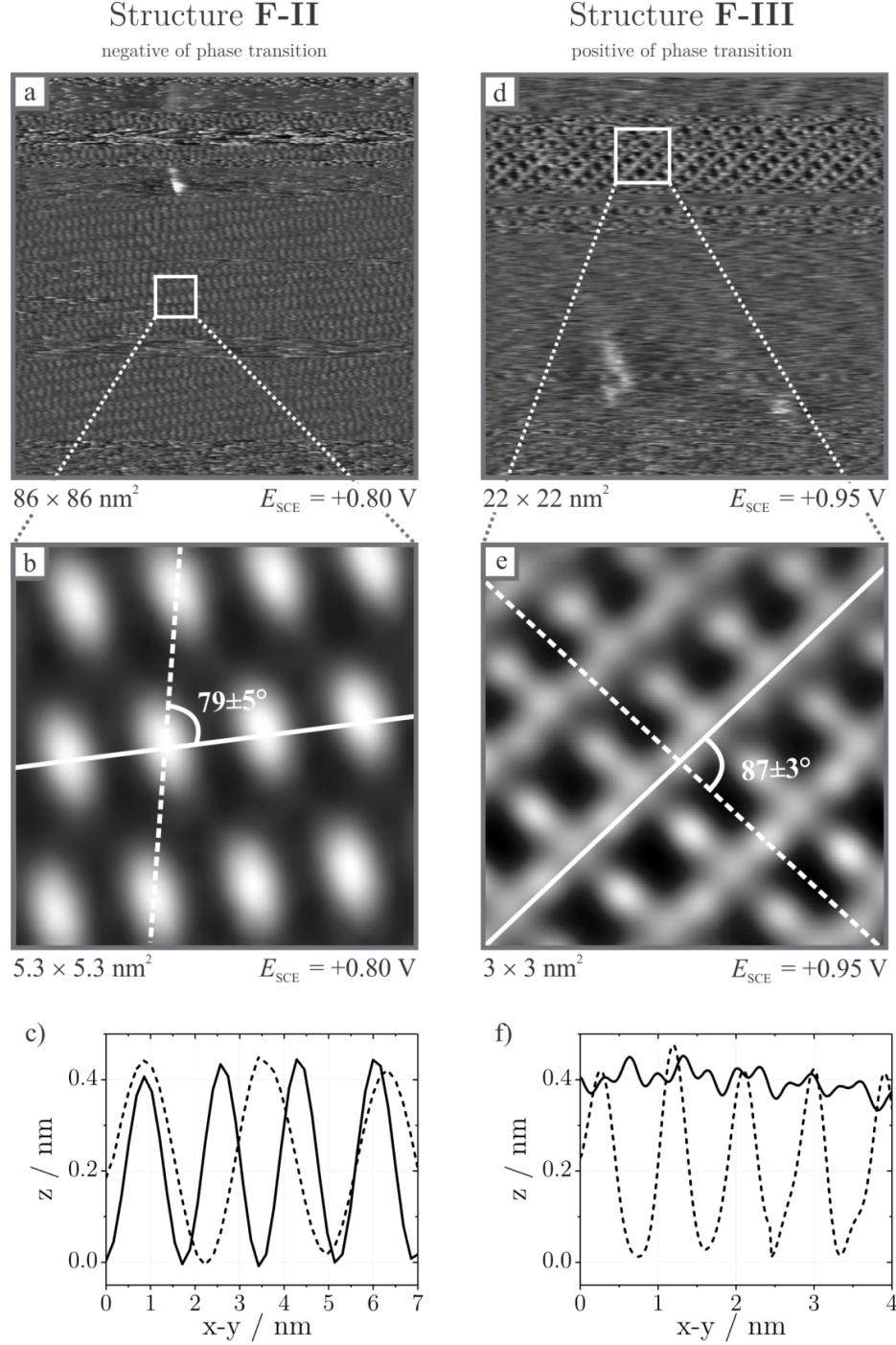


**Figure 5.9:** *in-situ* STM images of Au(111) in 0.2 M HCOOH + 0.1 M HClO<sub>4</sub> indicating two formate structures, first (a) negative of the phase transition, structure F-II: 86×86 nm<sup>2</sup>,  $E = 0.80$  V,  $U_T = 0.6$  V,  $I_T = 9$  nA, where (b) is a crop out and 2D-FFT of (a) and, (c) is the height profile of key features along the solid and the dotted lines in (b), and second (d) positive of the phase transition, structure F-III: 22×22 nm<sup>2</sup>,  $E = 0.95$  V,  $U_T = 0.65$  V,  $I_T = 3$  nA, where (e) is a crop out and 2D-FFT of (d) and, (f) is the height profile of key features along the solid and the dotted lines in (e).

Based on the experimental data, a simple model for both structures of adsorbed formate on a Au(111) electrode surface has been proposed (Figure 5.10). It is assumed that for structure F-III,  $\text{HCOO}_{\text{ad}}^{\text{B}}$  make up the compact chains in the *in-situ* STM image, in Figure 5.9e, and that a second formate species represents the second maxima. Respectively, structures F-II and F-III correspond to  $\theta_{\text{formate}}$  of  $\sim 0.02$  ML and 0.22 ML which is in the latter case, in agreement (to a great extent) with electrochemical measurements discussed above in this section.

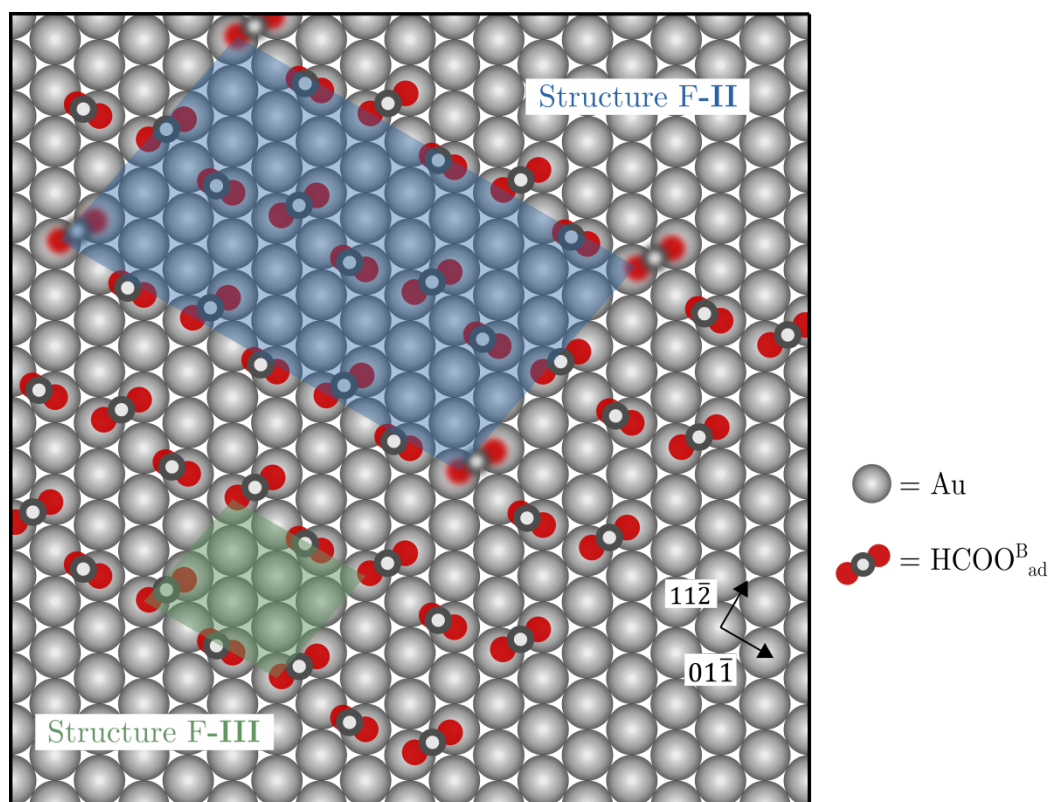


**Figure 5.10:** Model of structures F-II and F-III of adsorbed formate on a Au(111) surface in 0.2 M  $\text{HCOOH} + 0.1$  M  $\text{HClO}_4$ . Structures F-II and F-III are represented by a  $(2\sqrt{7} \times 9)$  and a  $(\sqrt{7} \times 3)$  arrangement of anions with respects to the underlying Au(111) surface, respectively.

From the *in-situ* STM images, Au surface sites are assumed to be blocked, mainly by the adsorption of a strongly bound formate anion in the bidentate configuration. This postulation is in good agreement with vibrational spectroscopic findings.<sup>[54,193,194]</sup> In fact, it

has been observed that with increasing the electrode potential in region II, formate is the only electrosorbed species to accumulate on Au.<sup>[54]</sup> In addition, using *in-situ* STM, a similar coverage (0.25 ML) was previously reported for the adsorption of formate on a Au(111) surface in 0.5 M HCOOH + 0.1 M HClO<sub>4</sub>. However, a different structure to that mentioned in this study is reported.<sup>[50]</sup>

### 5.3 Acetate vs. Formate Adsorption

The differences between the current-potential curves and structures in either electrolyte can be explained by the difference in the chemical nature and the structure of the species in solution. It is noteworthy that the formation of a 2D adlayer of the specifically adsorbing acetate or formate anions, on the underlying unreconstructed Au(111) substrate, is observed at approximately the same potential and is of a very similar surface coverage.<sup>[52]</sup> In fact, the phase transition kink in Figure 5.7, indicates the close resemblance of adsorbed acetate and formate. Interestingly, both acetate and formate adlayer structures on Au(111) resemble parallel zigzag chains.

Even so, a difference in the sharpness and the intensity of the phase transition peaks is observed. Clearly, the peak in the case of acetate is smaller than in the case of formate. The charge of the process (adsorption and rearrangement of the electrical double-layer) as well as its kinetics, affects the voltammetric response of an adlayer phase transition. The different behaviour of formate and acetate could possibly be a consequence of geometric and electronic properties. Acetate anions have the methyl group and are bigger in size compared to formate anions, which induces steric hindrance. This in turn affects hydrophobicity, causing changes in the structure of neighbouring water molecules, and subsequently alters the electrical double-layer properties. In other words, in the arrangement of adsorbed species, the nature of the adsorbed anion and/or coadsorbed water or hydronium molecules could play a major role. Moreover, the slight difference in formic acid and acetic acid acidity may result in different surface  $pK_a$  values, which may also influence the anions' adsorption behaviour. In this sense, since  $\text{CH}_3\text{COO}_{\text{ad}}$  species are expected to be oriented away from the solvent and have a relatively large dipole moment, they require stabilization by electrostatic interactions with a solvated  $\text{H}_3\text{O}^+$  or by neutral  $\text{H}_2\text{O}$  molecules. This is however not the case for  $\text{HCOO}_{\text{ad}}$  and therefore, in the proposed model for formate adsorption, a coadsorbed cationic species is not considered.

From the electrochemical and *in-situ* STM images above, both acetate and formate strongly adsorb on Au. This assumption is considered since sulfate, although not irreversibly adsorbed, is commonly considered as a strongly adsorbing anion too. The strength of binding of an acetate and a formate anion to the Au(111) surface is reflected by their onset potentials of adsorption. Evidently, the onset potentials of adsorption of either anion is very similar to that of sulfate. It is expected that formate forms a slightly weaker bond on the surface than acetate does since formic acid compared to acetic acid, is the stronger acid  $pK_a$  of 3.78.<sup>[208]</sup> For acetate and formate, the free-anion concentration in solution is approximately 2 and 6.5 mM, respectively. This could cause a difference of around 30 mV in onset potential. For the total concentration of 0.2 M of acetic acid, the onset potential for acetate adsorption is at 0.16 V vs. SCE. In comparison, the onset potential of formate adsorption, which starts simultaneously with formic acid oxidation, is at a slightly more negative potential of 0.1 V. It can therefore be concluded that the adsorption strength of both carboxylates is quite comparable. In fact, electrochemical measurements for Au(111) in formic acid with different added amounts of acetic acid indicate the coadsorption of acetate and formate anions.<sup>[52]</sup> The presence of both acetate and formate on the Au(111) surface, leads to an electrochemical behaviour with characteristics which lie in between those of each individual anion.

### **Specific Adsorption of Other Carboxylate Anions**

The dissociation of carboxylic acids results in anions which can be considered as examples of a significant class of species that affect both chemical and electrochemical reactions. Previous electrochemical studies on carboxylate anion adsorption include those carried out for formate,<sup>[48,50,205,206]</sup> acetate,<sup>[39,40,51,209]</sup> benzoate,<sup>[22,38,207,210]</sup> oxalate,<sup>[211–213]</sup> malonate,<sup>[214]</sup> succinate,<sup>[214]</sup> and citrate.<sup>[23]</sup> These studies suggest that the desired bonding to the surface is through the deprotonated carboxylate group's two oxygen atoms, *i.e.* in a bidentate adsorption configuration. Interestingly, all the two-oxygen carboxylates which have been studied so far using *in-situ* STM, exhibit phase transitions within their adsorbed layers.<sup>[50,207]</sup> The adsorption behaviour of carboxylates seems to become more complex for longer alkyl chains. For adsorption and reactivity studies on electrode surfaces, carboxylates are regarded as simple model compounds.<sup>[22,38]</sup> By comparing findings from a series of adsorption studies performed on carboxylates, the role of molecular structures on the interaction with the electrode surface can be obtained. Moreover, the influence of the structures of adsorbed anions on their acid-base equilibrium can be identified.

## 6 Adsorption of Phosphate Oxoanions

The blocking effect of strongly adsorbed phosphate on the electrocatalytic oxidation of formic acid on metallic surfaces has been extensively studied. Nevertheless, the geometry and structure of such adsorbates are yet to be investigated. This chapter will focus on the electrochemical behaviour and the arrangement of ordered structures of adsorbed phosphate on a Au(111) surface, in the presence of different alkali metal cations.

### 6.1 Au(111) in Sodium Phosphate Buffer Solutions

The adsorption of phosphate on Au(111) is systematically studied using cyclic voltammetry, for a large pH range between 1 and 12 (not shown). The measurements indicate that phase transition spikes which are related to the adsorption of phosphate on Au(111) are strongly dependent on both the pH and the electrode potential. The spikes are only observed for  $\text{pH} \geq 6.5$ . As an example, Figure 6.1 shows the current-potential curves for a freshly prepared, thermally annealed Au(111) electrode in different sodium phosphate buffer solutions. The distinct voltammograms for  $6 < \text{pH} < 11$  could be linked to the acid-base equilibrium of phosphate anions in bulk solution ( $\text{H}_2\text{PO}_4^- \rightleftharpoons \text{HPO}_4^{2-} + \text{H}^+$ ) and to  $\text{p}K_{\text{a}2} = 7.21$ .<sup>[215]</sup> Nonetheless, the adsorbed phosphate species are not essentially  $\text{H}_2\text{PO}_4^-$  and  $\text{HPO}_4^{2-}$  (where the latter, dominates in the bulk solution). It is also probable that similar to the case of  $\text{SO}_4^{2-}$  ions that more favourably adsorb on Au electrodes from  $\text{HSO}_4^-$  which is dominant at low pH values,  $\text{PO}_4^{3-}$  ions too adsorb on the electrified surface as a result of adsorption-induced deprotonation.

The similar current intensities of the spikes indicate that phosphate like sulfate anions, show reversible adsorption/desorption kinetics on the Au surface. Reversible kinetics have been reported (using SEIRAS) for the adsorption of phosphate anions on Au surfaces in this pH range.<sup>[69,70,216]</sup> Interestingly, it was also reported that a single preferred phosphate species seems to adsorb for  $6 < \text{pH} < 10$ . In an attempt to support these

findings, *in-situ* STM images for the adsorption of phosphate on Au(111) have been acquired. However, since the additional competitive adsorption of  $\text{OH}^-$  at  $\text{pH} > 10$  shifts towards more negative potentials and overlaps with the adsorption of phosphate, it is extremely difficult to image a structure at  $\text{pH} > 9$ . Therefore, an electrolyte with  $\text{pH} 7.6$  was chosen to perform the *in-situ* STM measurements.

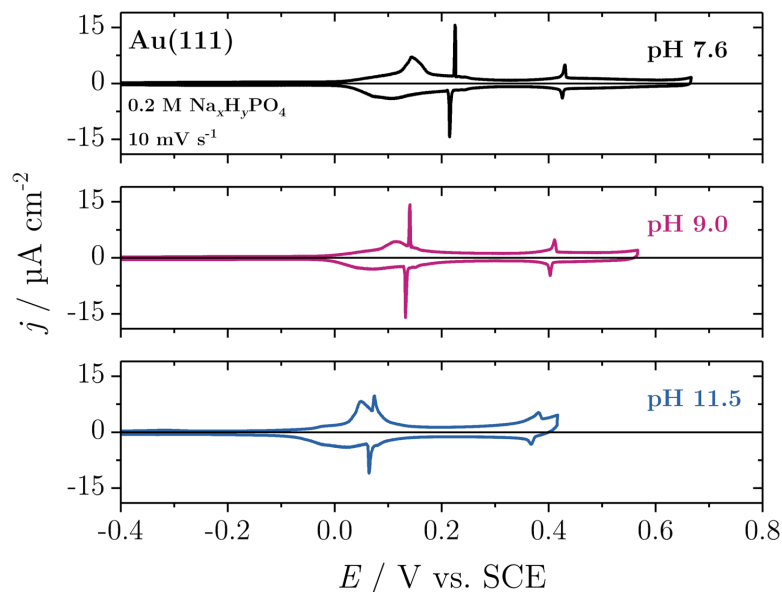


**Figure 6.1:** Current-potential curves of a freshly prepared Au(111) electrode in 0.2 M sodium phosphate buffer solutions at pH 7.6, pH 9.0 and pH 11.5 at 20 °C. Scan rate: 10 mV s<sup>-1</sup>.

### 6.1.1 Electrochemical Behaviour

Figure 6.2 shows the current-potential curve for a freshly prepared, thermally annealed Au(111) electrode in 0.185 M  $\text{Na}_2\text{HPO}_4$  + 0.015 M  $\text{NaH}_2\text{PO}_4$  at pH 7.6. The currents within the negative potential region (0.6 V–0.0 V) originate from the charging of the electrical double-layer. In this potential region, the reconstructed electrode surface is stable and is unaffected by the presence of phosphate anions in solution. The onset of phosphate adsorption lifts the gold surface reconstruction and transforms it to a (1×1) structure at around 0 V. Using *in-situ* STM, a reconstructed Au(111) surface with a  $(\sqrt{3} \times 22)$  structure is observed at -0.05 V which is lifted at more positive potentials (not shown). While taking the solution pH into account, the onset of the lifting of surface reconstruction of the Au(111) electrode occurs at approximately the same potential in the

presence of phosphate and sulfate anions (Figure 2.8). It is known that the onset of the lifting of surface reconstruction and anion adsorption depends on the adsorption strength of the anion.<sup>[1,78]</sup> It can therefore be assumed that phosphate anions adsorb on Au(111) as strongly as sulfate anions.<sup>[217]</sup> Nonetheless, care must be taken when making such interpretations since at pH 1,  $\sim 75\%$  of the phosphate in solution, remains undissociated. Hence, the lifting of the surface reconstruction at almost the same potential in either solution indicates that phosphate adsorbs slightly stronger than sulfate.<sup>[217]</sup>

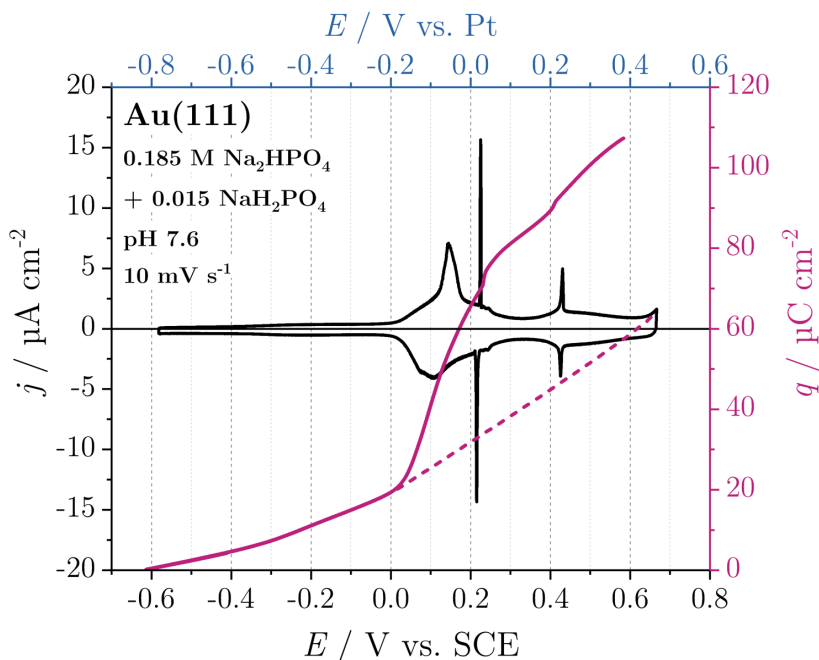


**Figure 6.2:** Current-potential curve (black) of a Au(111) electrode in 0.185 M  $\text{Na}_2\text{HPO}_4$  + 0.015 M  $\text{NaH}_2\text{PO}_4$  at pH 7.6 and at 20 °C. Scan rate: 10 mV s<sup>-1</sup>. Also shown, is the measured potential *vs.* Pt pseudo-reference electrode (blue) and anodic charge density *vs.* potential curve (pink). The dashed (pink) line corresponds to the estimated double-layer charge.

At 0.0–0.2 V and like in the case of sulfate, phosphate anions are assumed to adsorb on the surface; yet, no structure has been imaged. The images clearly indicate that phosphate, like sulfate, acts like a typical specifically adsorbing anion. Nonetheless, the edges of the islands in the presence of phosphate do not seem sharp, compared to those in the presence of sulfate. This phenomenon has been observed in several measurements and seems reproducible, regardless of the tip quality. It is possible that this observation is a

reflection of the adsorption strength of phosphate species on the Au(111) surface. In other words, at this potential where phosphate is already expected to adsorb, the mobility of the atoms on the surface seems to be relatively high due to the fact that more species are present in solution, in comparison to the case of sulfate.

The shape of the current-potential curve in Figure 6.2 resembles that of a Au(111) electrode in 0.1 M H<sub>2</sub>SO<sub>4</sub> (Figure 2.8). Unlike in the presence of sulfate however, in the presence of phosphate, two sharp current spikes can be observed at around 0.22 V and 0.42 V. As mentioned above, both spikes indicate a phase transition within the adlayer of adsorbed phosphate anions. One reason for the additional spike in the case of phosphate, compared to sulfate, is the polyprotic nature of phosphate species.<sup>[71]</sup> The two spikes hint that there could be two different adsorbed structures of phosphate anions on the Au(111) surface in the presence of sodium cations. Between the two spikes, the current displays a U-shaped profile, similar to the so-called *pit* around the *pzc* that can be observed in the adsorption studies of neutral organic molecules.<sup>[218]</sup> For the sake of simplicity, the U-shaped current profile in this work will also be referred to as the ‘pit’. Since the nature of the different adsorbed phosphate species cannot be revealed by the STM measurements, the adsorbates are herein referred to as phosphates.

The electrochemical measurement in Figure 6.2 also shows the anodic charge density *vs.* potential plot, where the charge density continuously increases with increasing potential. The adsorption isotherms are calculated by subtracting the double-layer charge for the Au(111) electrode, resulting in a charge density of ca. 55  $\mu\text{C cm}^{-2}$  and 65  $\mu\text{C cm}^{-2}$ , for the first and second phase transition spikes, respectively. Since the values of the charge densities for both the sulfate and phosphate systems are very similar, one would also expect a one-electron-transfer reaction to take place in the case of phosphate adsorption. Therefore, assuming a charge density of 222  $\mu\text{C cm}^{-2}$  for a charge of full monolayer coverage on a smooth Au(111) surface, the total phosphate coverage ( $\theta_{\text{phosphate}}$ ) is  $\sim 0.25$  ML and 0.27 ML for the first and second phase transition spikes, respectively. Nonetheless, the *in-situ* STM images of phosphate adsorbed on Au(111) can help verify the assumption that a one-electron-transfer indeed takes place.

### 6.1.2 Potential Dependence on Phosphate Structure P-I

Figure 6.3 shows the magnification of the two current spikes in the current-potential curve found in Figure 6.2. A series of *in-situ* STM images of a Au(111) electrode were recorded at different potentials between the spikes (Figure 6.3b-d).



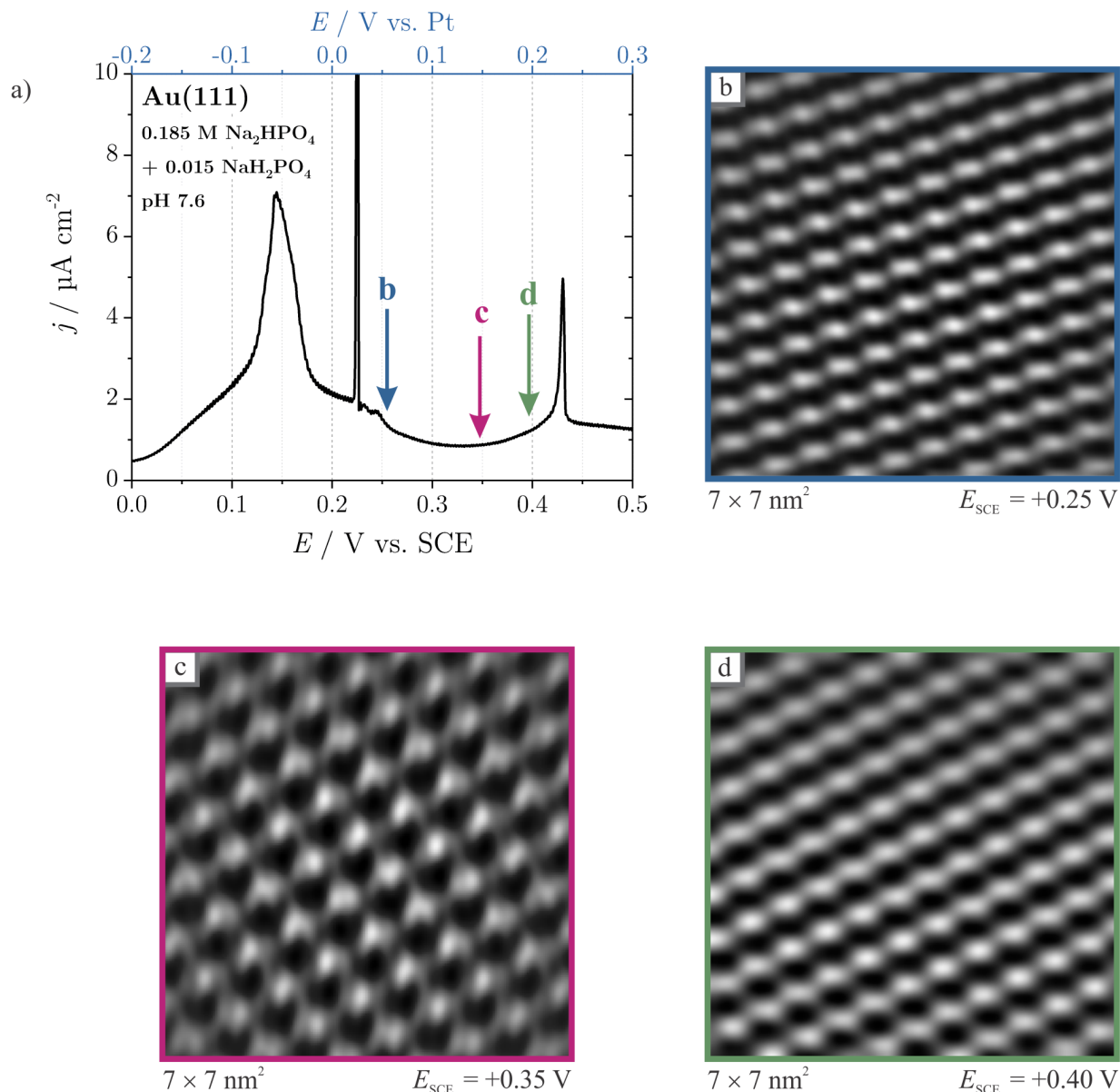


**Figure 6.3:** (a) Current-potential curve of a Au(111) electrode in 0.185 M Na<sub>2</sub>HPO<sub>4</sub> + 0.015 M NaH<sub>2</sub>PO<sub>4</sub> at pH 7.6, displaying the U-shaped ‘pit’ in the positive-going scan. Scan rate: 10 mV s<sup>-1</sup>. (b-d) A series of 2D-FFT *in-situ* STM images of Au(111) showing ordered structures of adsorbed phosphate at different potentials within the so-called ‘pit’, where (b)  $7 \times 7 \text{ nm}^2$ ,  $E = 0.25 \text{ V}$ ,  $U_{\text{T}} = 0.1 \text{ V}$ ,  $I_{\text{T}} = 2.5 \text{ nA}$  and (c)  $7 \times 7 \text{ nm}^2$ ,  $E = 0.35 \text{ V}$ ,  $U_{\text{T}} = 0.2 \text{ V}$ ,  $I_{\text{T}} = 2 \text{ nA}$  and (d)  $7 \times 7 \text{ nm}^2$ ,  $E = 0.4 \text{ V}$ ,  $U_{\text{T}} = 0.23 \text{ V}$ ,  $I_{\text{T}} = 2 \text{ nA}$ .

The formation of an ordered adlayer of parallel rows of phosphates in the presence of sodium cations, is observed (phosphate structure P-I). This finding indicates that the adsorption of phosphate is highly influenced by the nature of the cation since at a similar

pH value, an ordered structure of adsorbed phosphate could not be found when potassium cations were present in solution, instead.<sup>[9,20]</sup> In addition, a potential dependence on structure P-I has been observed as shown in Figure 6.4. Figure 6.4a shows that structure P-I seems to be more compact at potentials closer to one of the two current spikes, where the current densities are slightly higher than at the centre of the pit.

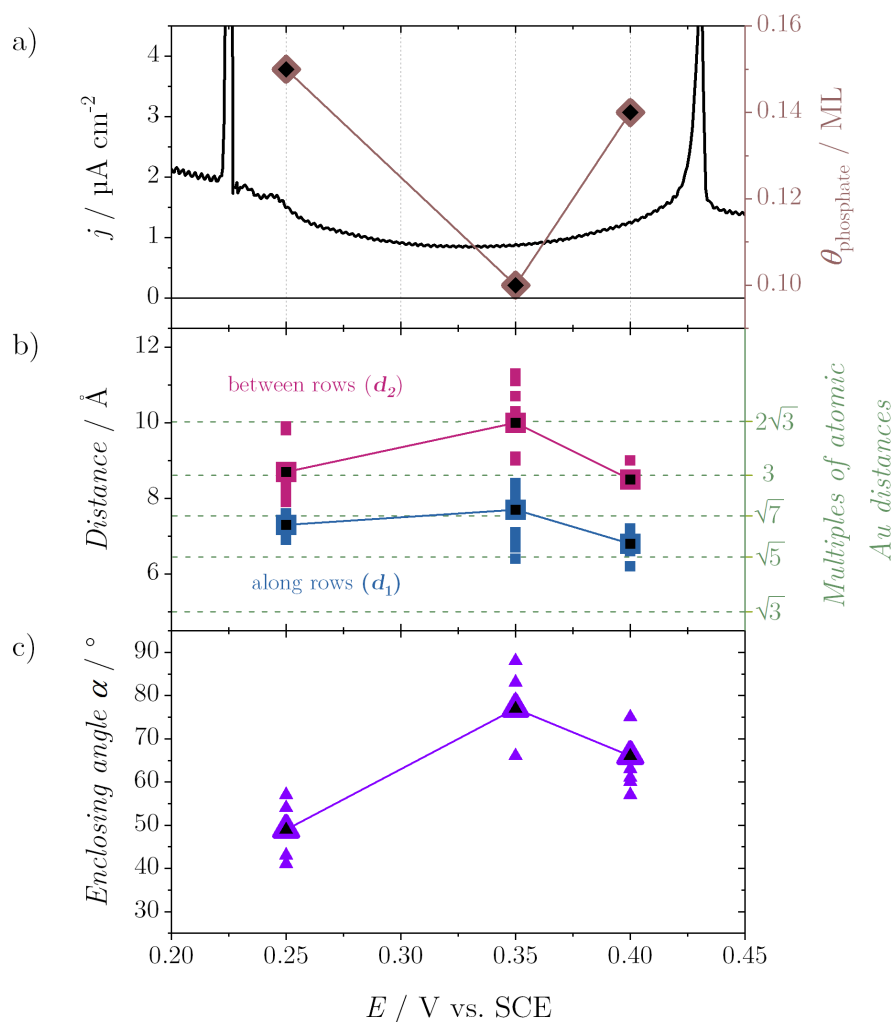


**Figure 6.4:** (a) Current-potential curve of a Au(111) electrode in 0.185 M  $\text{Na}_2\text{HPO}_4$  + 0.015 M  $\text{NaH}_2\text{PO}_4$  at pH 7.6, displaying the U-shaped ‘pit’ in the positive-going scan. Scan rate: 10  $\text{mV s}^{-1}$ , in addition to the potential dependence on total  $\theta_{\text{phosphate}}$  coverage and (b) on the phosphate-phosphate distances along ( $d_1$ ) and between ( $d_2$ ) the rows, as well as (c) on the measured enclosing angles ( $\alpha$ ) obtained from *in-situ* STM images.

Since this chapter contains several ordered structures with very similar geometries, the dimensions of the structures are given in terms of abbreviations/symbols. Figure 6.4b and c represent the influence of electrode potential on the nearest distances separating two phosphates along a row ( $d_1$ ) and between the adjacent rows ( $d_2$ ), as well as their enclosing angles ( $\alpha$ ), respectively. Both distances, along and between the rows, decrease at potentials close to the current spikes. The same trend is observed for the enclosing angle. This results in a total  $\theta_{\text{phosphate}}$  of around 0.15 ML at 0.25 and at 0.40 V, as seen in Figure 6.4a. For the sake of clarity, the potential dependence on the distances  $d_1$  and  $d_2$ ,  $\alpha$  and  $\theta_{\text{phosphate}}$  of structure P-I is shown in Table 6.1. These values represent the statistical average values obtained from *in-situ* STM images at different electrode potentials.

**Table 6.1:** Averaged phosphate-phosphate distances along ( $d_1$ ) and between ( $d_2$ ) the rows, as well as the measured enclosing angles ( $\alpha$ ) and total  $\theta_{\text{phosphate}}$  coverages obtained from *in-situ* STM images of a Au(111) electrode in 0.185 M  $\text{Na}_2\text{HPO}_4$  + 0.015 M  $\text{NaH}_2\text{PO}_4$  at pH 7.6 of structure P-I of adsorbed phosphate at different potentials.

$E / \text{V}$	$d_1 / \text{\AA}$	$d_2 / \text{\AA}$	$\alpha / ^\circ$	$\theta / \text{ML}$
0.25	$7.3 \pm 0.4$	$8.7 \pm 0.9$	$49 \pm 10$	0.15
0.35	$7.7 \pm 0.4$	$10.0 \pm 1.0$	$77 \pm 4$	0.10
0.40	$6.8 \pm 0.6$	$8.6 \pm 0.5$	$66 \pm 3$	0.14

It is clear that the structure at 0.25 V and at 0.40 V is very similar and a ‘breathing’ effect seems to take place around this potential region *i.e.* the structure fluctuates between a metastable structure found close to the current spikes and a more thermodynamically stable one towards the centre of the pit. Since the differences in distances are within the margin of error, structure P-I will be assumed to most-likely resemble the adlayer imaged at the pit ( $E = 0.35$  V). At this potential, the distances and enclosing angle correspond to a  $(2\sqrt{3} \times \sqrt{7})$  structure, similar to that of sulfate anions adsorbed on Au(111). However, in contrast to the sulfate structure, one of the two unit cell vectors ( $\sqrt{3}$ ) is double in size. This results in a calculated  $\theta_{\text{phosphate}}$  of about 0.1 ML which is around half of the coverage calculated from the electrochemical measurement, discussed above in Section 6.1. Hence, a two- instead of a one-electron-transfer reaction is

expected to take place at the metal-electrolyte interface during the adsorption of phosphate anions on Au(111) at potentials between 0.25 V and 0.40 V.

Interestingly, the  $\theta_{\text{phosphate}}$  at 0.35 V is half of that of either adsorbed sulfate<sup>[9]</sup> or adsorbed phosphate in the presence of potassium cations.<sup>[20]</sup> These findings strongly indicate that the observed structures of tetrahedral four-oxygen oxoanions seem to be highly dependent on the nature of the coadsorbate and on the alkali metal cation. From the charge calculations, there could be two possibilities regarding the nature of the coadsorbed species with which phosphate anions can adsorb on a Au(111) electrode. Both possibilities rely on the assumption that only phosphate species with three free oxygen atoms to occupy the trigonal adsorption sites of the Au(111), like in the case of sulfate, are considered. Those species are  $\text{HPO}_4^{2-}$  and  $\text{PO}_4^{3-}$ .

The first possibility would be that at this pH, a dominant species like the  $\text{HPO}_4^{2-}$  ion is stabilized by a coadsorbate. On the one hand, a single  $\text{HPO}_4^{2-}$  ion could coadsorb with a neutral  $\text{H}_2\text{O}$  molecule. On the other hand, two  $\text{HPO}_4^{2-}$  ions could adsorb as a unit with a single coadsorbed  $\text{H}_3\text{O}^+$  or  $\text{Na}^+$  ion. The coadsorption of the cationic hydronium or sodium ions would weaken the coulombic repulsions between the adjacent phosphate anions. Nonetheless, it is more likely that  $\text{Na}^+$  ions rather than  $\text{H}_3\text{O}^+$  ions or water, coadsorb within the adlayer. The absence of an ordered phosphate structure on Au(111) in acidic and neutral solutions in the presence of  $\text{K}^+$  ions, suggests that the coadsorption of  $\text{Na}^+$  ions plays a major role in stabilizing ordered phosphate structures.<sup>[9]</sup>

The second (more-likely) possibility is that a  $\text{PO}_4^{3-}$  ion, although not the dominant species in solution, adsorbs on the surface along with a  $\text{H}_3\text{O}^+$  or a  $\text{Na}^+$  ion. The molecules in this case match the geometrical arrangement of the Au(111) surface, like in the case of sulfate adsorption. Assuming phosphate anions show a similar behaviour to sulfate anions upon adsorption, it is possible that the observed phosphate structure, like the sulfate structure, is stabilized by a coadsorbed  $\text{H}_3\text{O}^+$  cation. In this case however,  $\text{Na}^+$  cations are most likely the coadsorbate since they are the dominant cationic species in solution. In addition, the ionic radius of a hydronium cation in solution is  $1.41 \pm 0.02 \text{ \AA}$  while a solvated sodium cation has a radius of  $2.36 \pm 0.06 \text{ \AA}$ .<sup>[219]</sup> The difference in size of the coadsorbate could explain the difference in the adsorbed structures of both sulfate and phosphate. Assuming that the sodium cations are adsorbing with their solvation shell intact, the required space to fit a sodium cation between two phosphate species on the surface is nearly double that for a non-solvated hydronium cation. Consequently, the  $\text{PO}_4^{3-}$  ions are forced to adsorb in a more open structure than  $\text{SO}_4^{2-}$  ions. As explained

above, this possibility would be analogous to the sulfate structure on Au(111) which is stabilized by  $\text{H}_3\text{O}^+$  cations, since the  $\text{SO}_4^{2-}$  ion as well, is not the dominant species in solution.

### 6.1.3 Phosphate Structure P-II

Figure 6.5b-d shows a sequence of *in-situ* STM images of a Au(111) electrode surface at potentials positive and negative of the second phase transition spike at 0.43 V in the positive-going scan of the current-potential curve (Figure 6.5a). It is observed that structure P-I which was imaged negative of the second phase transition spike at around 0.32 V (Figure 6.5c), disappears from the terraces and a structure of parallel rows reappears on top of islands (Figure 6.5b and d) when the potential is stepped to around 0.5 V, positive of the spike. From the *in-situ* STM images, the nearest-neighbour distances between two phosphate anions along a row ( $d_1$ ), between the adjacent rows ( $d_2$ ), and its enclosing angle ( $\alpha$ ) were obtained. On the monoatomic high islands, the average dimensions of the structure are  $d_1 = 5.5 \pm 0.5 \text{ \AA}$ ,  $d_2 = 6.9 \pm 0.7 \text{ \AA}$  and  $\alpha = 73 \pm 2^\circ$ , as shown in Figure 6.6a and b. The dimensions are related to a second structure (phosphate structure P-II) since the values are distinctly different from those measured for structure P-I. The measured distances and angle for the structure on top of the islands resemble a  $(\sqrt{3} \times \sqrt{7})$  structure and a  $\theta_{\text{phosphate}}$  of  $\sim 0.2 \text{ ML}$ , which is double the coverage obtained for structure P-I. Noteworthy is the fact that at a potential where structure P-I is imaged, a higher activity in formic acid oxidation negative of the step-up in current is observed.

Since structure P-II is similar to that of adsorbed sulfate positive of the phase transition spike, it is possible that structure P-I resembles that of sulfate at potentials negative of the phase transition within the adsorbed adlayer on a Au(111) electrode, even though no structure has been imaged. The formation of an ordered structure positive of the current spike at 0.43 V was not only observed on top of the Au islands but also near step edges (Figure 6.6c and d). Near step edges, the averaged dimensions are  $d_1 = 5.6 \pm 0.5 \text{ \AA}$ ,  $d_2 = 11.1 \pm 1.0 \text{ \AA}$  and  $\alpha = 62 \pm 6^\circ$ . Interestingly, the distance  $d_1$  is almost identical for the imaged structures on top of the islands and at step edges. In addition, the calculated  $\theta_{\text{phosphate}}$  at the step edges is  $\sim 0.13 \text{ ML}$ , which is close to those obtained for the metastable structure at potentials slightly positive of the first spike and slightly negative of the second spike at 0.25 V and at 0.40 V, respectively. It is possible that either structure is essentially the same, but their potential dependence is related to the type of defect found on the surface.

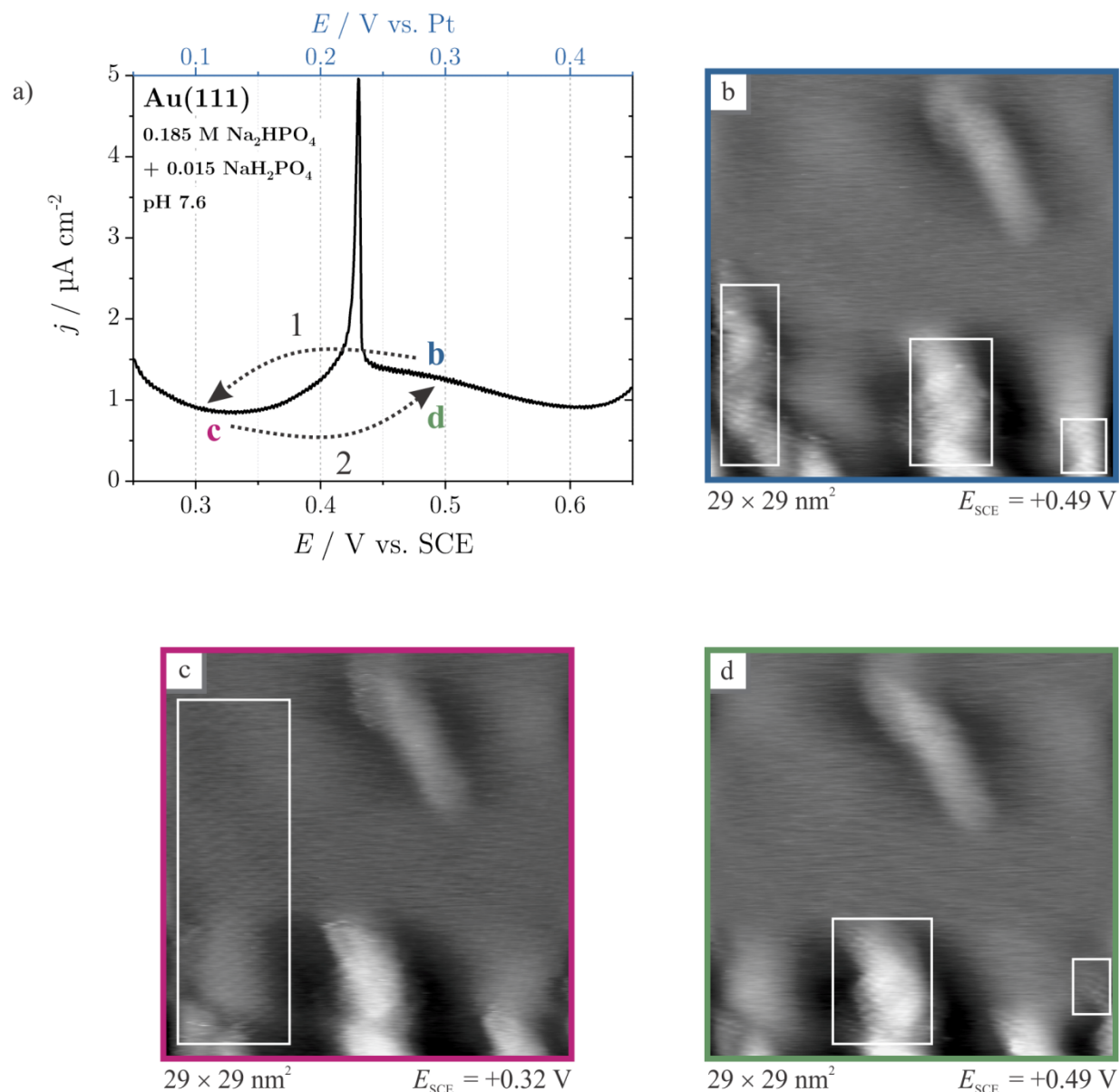


**Figure 6.5:** (a) Current-potential curve of a Au(111) electrode in 0.185 M  $\text{Na}_2\text{HPO}_4$  + 0.015 M  $\text{NaH}_2\text{PO}_4$  at pH 7.6, displaying the second current spike attributed to a phase transition in the positive-going scan. Scan rate  $10 \text{ mV s}^{-1}$ . (b-d) A series of *in-situ* STM images indicating ordered structures of adsorbed phosphate at different areas on the surface (white box) where, (b)  $29 \times 29 \text{ nm}^2$ ,  $E = 0.49 \text{ V}$ ,  $U_T = 0.32 \text{ V}$ ,  $I_T = 4 \text{ nA}$ . (c)  $29 \times 29 \text{ nm}^2$ ,  $E = 0.32 \text{ V}$ ,  $U_T = 0.15 \text{ V}$ ,  $I_T = 4 \text{ nA}$ . (d)  $29 \times 29 \text{ nm}^2$ ,  $E = 0.49 \text{ V}$ ,  $U_T = 0.32 \text{ V}$ ,  $I_T = 4 \text{ nA}$ .

Structure P-II is only stable near surface defects. Even after imaging positive of the second phase transition spike for almost an hour, no ordered structure was observed on the terraces. The adsorption behaviour of phosphate anions positive and negative of the

second phase transition spike (at 0.43 V) is distinctly different. It is likely that phosphate electrolytes adsorb  $\text{CO}_2$  to form carbonates, which could be a reason the different structures. These findings are reproducible; however, during the measurements a continuous shift in the electrode potential is present. This shift is compensated during the measurements; yet, it is difficult to disregard the fact that in this potential region, even slight potential shifts could affect the analysis of the *in-situ* STM images.

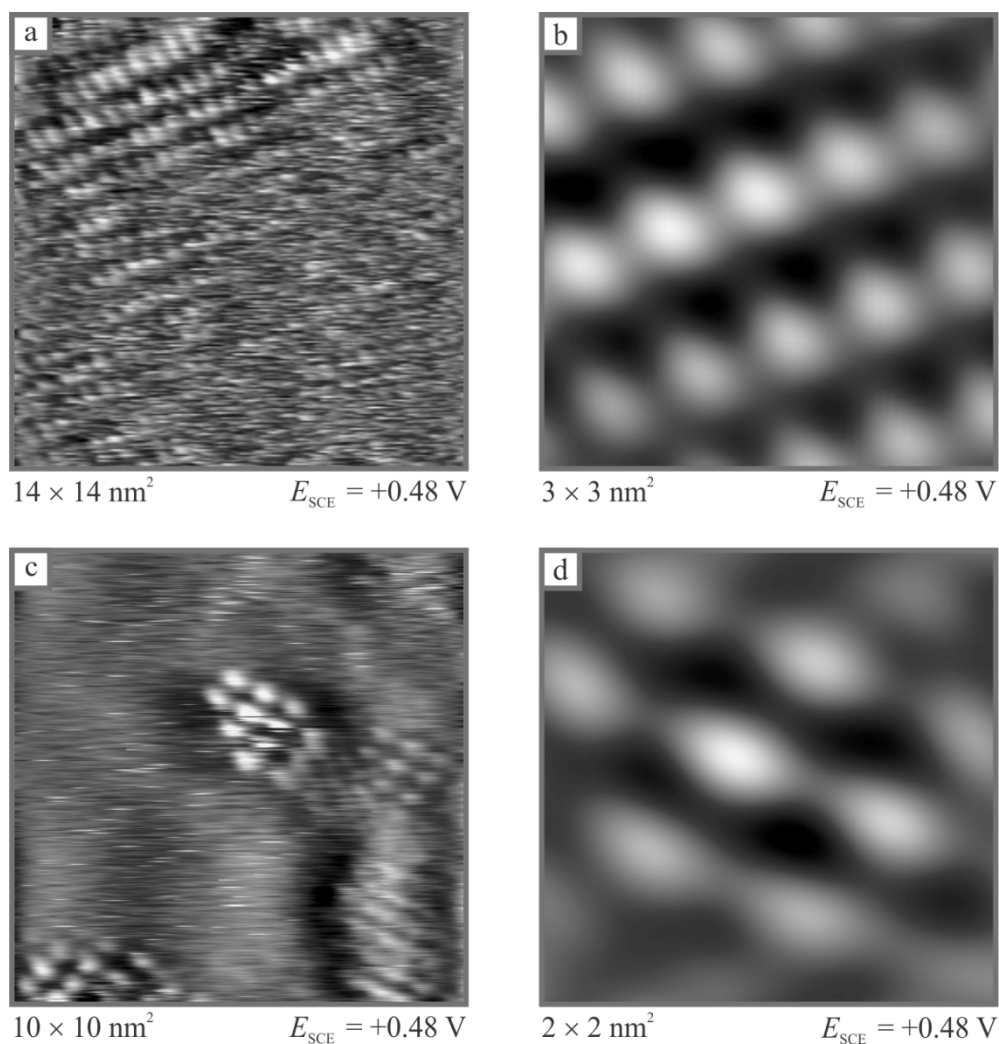


**Figure 6.6:** *in-situ* STM images of Au(111) in 0.185 M  $\text{Na}_2\text{HPO}_4$  + 0.015 M  $\text{NaH}_2\text{PO}_4$  at pH 7.6 indicating ordered structures of adsorbed phosphate (a) on top of a monoatomic high Au island:  $14 \times 14 \text{ nm}^2$ ,  $E = 0.48 \text{ V}$ ,  $U_T = 0.24 \text{ V}$ ,  $I_T = 2 \text{ nA}$  where (b) is a crop out and 2D-FFT of the *in-situ* STM image in (a):  $3 \times 3 \text{ nm}^2$ , and (c) at step edges:  $10 \times 10 \text{ nm}^2$ ,  $E = 0.48 \text{ V}$ ,  $U_T = 0.32 \text{ V}$ ,  $I_T = 4 \text{ nA}$  where (d) is a crop out and 2D-FFT of the *in-situ* STM image in (c).



Clearly, it is impossible from *in-situ* STM images alone to determine the nature of the phosphate species which adsorb on Au(111). However, spectroscopic studies have revealed that  $\text{PO}_4$  in  $\text{HPO}_4^{2-}$  dominant alkaline solutions are the adsorbed phosphate species at Au surfaces.<sup>[67]</sup> This finding highlights the importance of deprotonation upon adsorption. In addition, geometry optimization calculations have revealed that  $\text{PO}_4$  prefers to bind in a tridentate configuration via three O atoms on the Au(111) surface.<sup>[67]</sup> Based on the above considerations, Figure 6.7 shows a model for the  $(2\sqrt{3} \times \sqrt{7})$  and  $(\sqrt{3} \times \sqrt{7})$  phosphate P-I and P-II structures on a Au(111) electrode, respectively. The main maxima in the *in-situ* STM images in Figure 6.3b and Figure 6.6c representing the two main structures are assigned to phosphate. The  $\text{PO}_4^{3-}$  ions adsorb in a trigonal configuration alongside coadsorbed  $\text{Na}^+$  ions, on the top sites of the Au(111) surface.

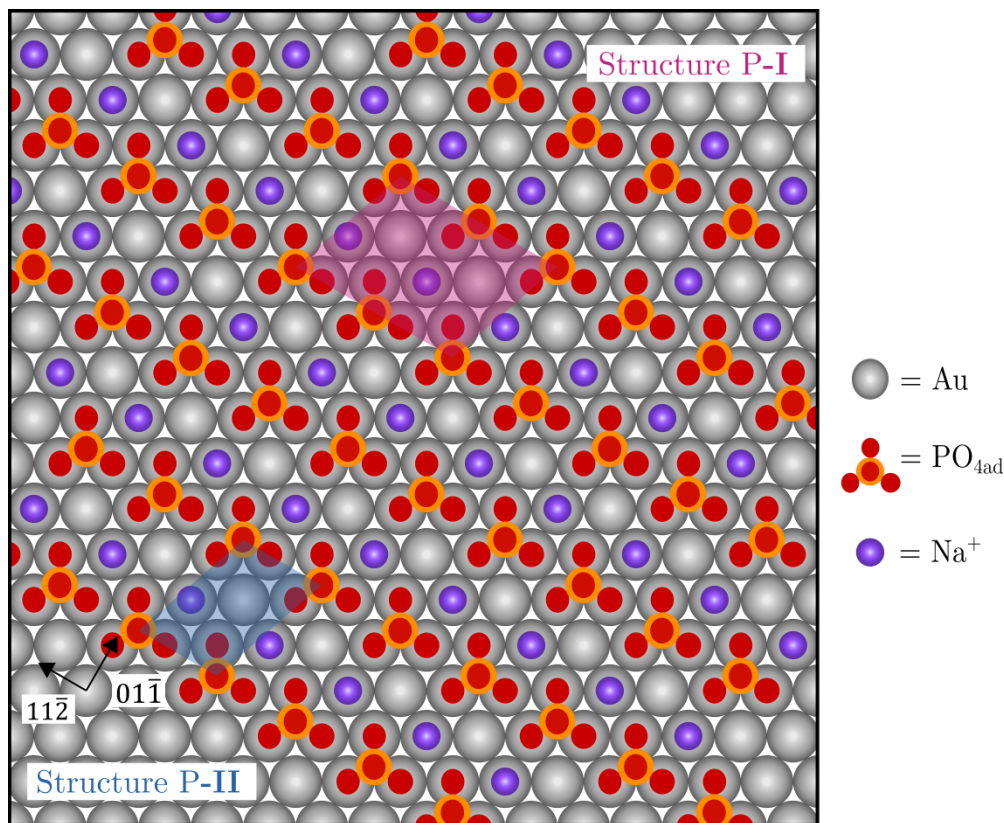


**Figure 6.7:** Model for structures P-I and P-II of adsorbed phosphate on a Au(111) surface in 0.185 M  $\text{Na}_2\text{HPO}_4$  + 0.015 M  $\text{NaH}_2\text{PO}_4$  at pH 7.6. Structures P-I and P-II are represented by a  $(2\sqrt{3} \times \sqrt{7})$  and a  $(\sqrt{3} \times \sqrt{7})$  arrangement of anions with respects to the underlying Au(111) surface, respectively. The structures are stabilized by coadsorbed  $\text{Na}^+$  ions.



As mentioned above, although the main species in solution at pH 7.6 is  $\text{HPO}_4^{2-}$ , it is difficult to determine the most likely adsorbed phosphate species on the surface. By slightly varying the molar fractions of  $\text{HPO}_4^{2-}$  and  $\text{H}_2\text{PO}_4^-$  in solution at this pH range, the influence of the nature of phosphate species on the imaged structures can be studied. Therefore, further *in-situ* STM measurements at a slightly lower pH 7.3, where the current spikes are prominent, have also been conducted. At pH 7.3, the amount of  $\text{HPO}_4^{2-}$  and  $\text{H}_2\text{PO}_4^-$  is almost equimolar. Figure 6.8 represents the current-potential curve of the Au(111) electrode in 0.04 M  $\text{Na}_2\text{HPO}_4$  + 0.16 M  $\text{NaH}_2\text{PO}_4$  at pH 7.3 along with a series of *in-situ* STM image at characteristic potentials in the voltammogram. The measured dimensions  $d_1$ ,  $d_2$  and  $\alpha$  of the structures measured at different potentials for pH 7.3 are very similar to those for pH 7.6. The dimensions are summarized in Table 6.2.

A potential dependence on the structure in between the two current spikes (structure P-I) is likewise observed. More specifically, the calculated  $\theta_{\text{phosphate}}$  decreases slightly, towards the center of the pit, with changing the potential. When the potential is stepped positive of the second spike, it is seen that structure P-II prefers to form at the proximity of surface defects like Au islands, as was the case for pH 7.6. The dimensions of structure P-II at pH 7.3 closely resemble a  $(\sqrt{3} \times \sqrt{7})$  structure and have a calculated  $\theta_{\text{phosphate}}$  of 0.19 ML. It can therefore be concluded that in this pH range, the adsorption behaviour of phosphate in the presence of sodium cations is independent of pH. Naively, it could have first been hypothesized that the adsorption of phosphate on Au(111) depends solely on the pH of the electrolyte or on structuring at the interface. However, measurements indicate that a vital role is also played by non-covalent interactions between spectator species like alkali metal cations and by Au(111) active sites.

**Table 6.2:** Averaged phosphate-phosphate distances along ( $d_1$ ) and between ( $d_2$ ) the rows, as well as the measured enclosing angles ( $\alpha$ ) and total  $\theta_{\text{phosphate}}$  coverages obtained from *in-situ* STM images of a Au(111) electrode in 0.04 M  $\text{Na}_2\text{HPO}_4$  + 0.16 M  $\text{NaH}_2\text{PO}_4$  at pH 7.3 of structures P-I and P-II of adsorbed phosphate at different potentials.

$E / \text{V}$	$d_1 / \text{\AA}$	$d_2 / \text{\AA}$	$\alpha / ^\circ$	$\theta / \text{ML}$
0.25	$6.9 \pm 0.4$	$8.3 \pm 0.3$	$50 \pm 2$	0.16
0.30	$6.5 \pm 0.4$	$8.1 \pm 0.9$	$66 \pm 9$	0.15
0.46	$5.8 \pm 0.3$	$7.2 \pm 0.6$	$69 \pm 5$	0.19

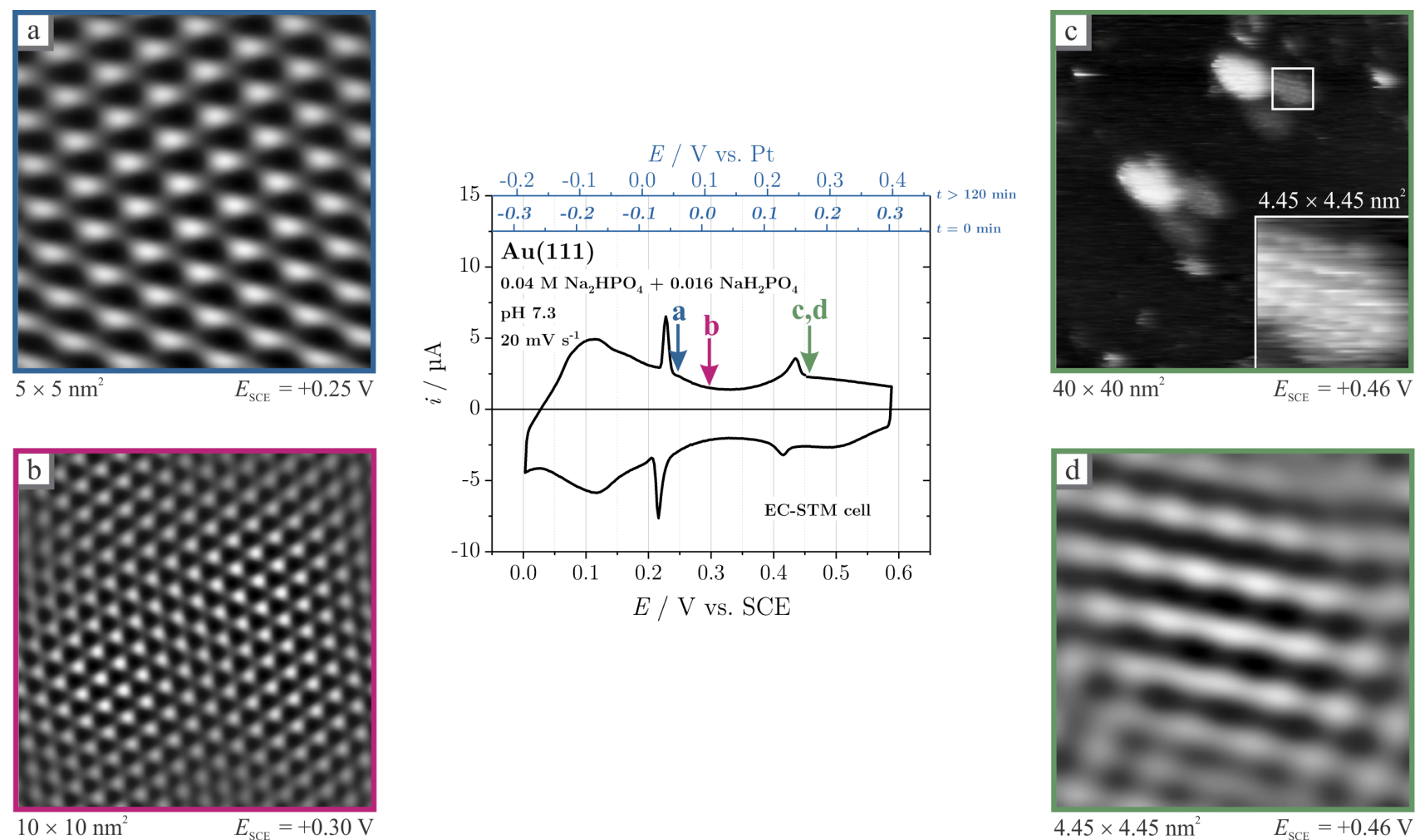


**Figure 6.8:** Current-potential curve for a Au(111) electrode in 0.04 M  $\text{Na}_2\text{HPO}_4$  + 0.16 M  $\text{NaH}_2\text{PO}_4$  at pH 7.3. Scan rate 10 mV  $\text{s}^{-1}$ . A series of *in-situ* STM images representing ordered structures of adsorbed phosphate that are (a) on a terrace:  $5 \times 5 \text{ nm}^2$  (2D-FFT),  $E = 0.25 \text{ V}$ ,  $U_{\text{T}} = -0.11 \text{ V}$ ,  $I_{\text{T}} = 3 \text{ nA}$ , (b):  $10 \times 10 \text{ nm}^2$  (2D-FFT),  $E = 0.3 \text{ V}$ ,  $U_{\text{T}} = -0.16 \text{ V}$ ,  $I_{\text{T}} = 2.5 \text{ nA}$ , (c) on Au islands:  $40 \times 40 \text{ nm}^2$ ,  $E = 0.46 \text{ V}$ ,  $U_{\text{T}} = -0.19 \text{ V}$ ,  $I_{\text{T}} = 4 \text{ nA}$ , where the inset is a zoom in of the structure:  $4.45 \times 4.45 \text{ nm}^2$ , and (d) is a 2D-FFT of the 'zoom in' in (c).

## 6.2 Au(111) in a Lithium Phosphate Buffer Solution

As discussed above, ordered structures of adsorbed phosphate form on Au(111) in the presence of sodium cations. Since the exchange of the alkali metal cation can most-likely influence the adsorbed structures of phosphate on the surface, it was only logical to study the adsorption behaviour of phosphate ions in the presence of a similar cation like lithium.

Figure 6.9 shows the current-potential curve of a Au(111) electrode in 0.1 M  $\text{H}_3\text{PO}_4$  + 0.18 M LiOH at pH 7.3 along with a series of *in-situ* STM image at characteristic potentials in the voltammogram. The voltammogram is shifted to slightly more positive potentials (around 20 mV) compared to that in the presence sodium cations in Figure 6.2, owing to the slight difference in pH value. In the negative potential region, the current-potential curve looks similar to that measured for a Au(111) electrode in the presence of sodium phosphate (Figure 6.2). In the double-layer region, the electrode surface is reconstructed (not shown). The reconstruction lines show a potential dependence on the shape the reconstruction lines like those observed in the presence of sulfate anions (Section 4.1). The peak at around 0.17 V is assigned to the lifting of the surface reconstruction due to the onset of phosphate adsorption. At potentials 0.0–0.20 V, where phosphate is expected to adsorb, no structure was imaged using *in-situ* STM like in the case of sulfate anions or phosphate anions in the presence of sodium cations.

In the positive potential region however, the current-potential curve looks different with only one sharp current spike at  $\sim 0.23$  V. The spike indicates a phase transition within the phosphate adlayer which has been confirmed using STM. Figure 6.9a represents an *in-situ* STM image of an ordered structure of adsorbed phosphate positive of the spike at 0.35 V. The diameter of each bright spot in the image resembles that of a phosphate anion. Paired with the phosphate species, small *hook-like* structures that can be assigned to a coadsorbate were also imaged. From the *in-situ* STM image, the nearest-neighbour distances between two phosphate anions along a row ( $d_1$ ), between the adjacent rows ( $d_2$ ), and its enclosing angle ( $\alpha$ ) were obtained. The structure positive of the current spike has the following dimensions:  $d_1 = 14.9 \pm 0.6$  Å,  $d_2 = 17.9 \pm 0.9$  Å and  $\alpha = 74 \pm 4^\circ$  which amounts to a total  $\theta_{\text{phosphate}}$  of 0.07 ML. The coverage is smaller than that found for phosphate adsorbed on a Au(111) surface in the presence of sodium (discussed in Section 6.1) and in the presence of potassium<sup>[137]</sup>. The adsorption of phosphate anions in a sulfate-like structure might be hindered by the nature of the coadsorbate. The radius of a solvated lithium cation is much larger than that of a solvated sodium cation since a

second hydration shell has to be considered in the case of lithium. The solvated ion would therefore require more space on the surface during adsorption. Consequently, the phosphate ions would repel one another to give space for the coadsorbed lithium cations, resulting in a more open structure.

At more positive potentials, an anodic peak in the current-potential curve in Figure 6.9 is observed at around 0.50 V. The potential of the counter peak in the negative-going scan is shifted around 100 mV more negative. It is possible that the formation of a second phase transition is kinetically hindered. Indeed the *in-situ* STM image in Figure 6.9b of the Au(111) electrode surface positive of the anodic peak at 0.6 V shows a semi-disordered structure of an adsorbate. Still it is possible to measure the dimensions of the structure where  $d_1 = 13.7 \pm 0.9$  Å,  $d_2 = 14.7 \pm 0.9$  Å,  $\alpha = 80 \pm 5^\circ$ . Despite the lower degree of order, the structure, compared to that imaged negative of the peak at 0.5 V, is denser with a  $\theta_{\text{phosphate}}$  of 0.1 ML. It should be noted that these values have to be regarded with care as the structure is only semi-ordered and the margin of error is higher than that of the ordered structure that has been imaged before for structure P-II on the Au islands in the presence of sodium cations.

Similar to the case of adsorbed phosphate in the presence of sodium cations, a potential dependence on the coverage of anions is observed in the presence of lithium cations. In both cases, the coverage increases with increasing electrode potential. Nonetheless, the adsorption behaviour of phosphate anions at positive potential seems different. While structure P-II in the presence of sodium cations tends to form only in the proximity of surface defects, the structure observed in the presence of lithium cations can be found on the terraces. This could be due to a different stabilization from a coadsorbate. Since solvated lithium ions have a larger diameter than solvated sodium cations, the amount of space they require as a coadsorbate is much larger. On the other hand, at the potential range where the semi-ordered structure is imaged, the onset of hydroxide adsorption occurs. A competition between  $\text{Li}^+$  and  $\text{OH}^-$  species can result in the higher mobility of atoms on the surface and hence, a less ordered structure.

As the potential is stepped back to 0.48 V, between the anodic and the cathodic peaks, the semi-ordered structure transitions to a more ordered one (Figure 6.9d). From this measurement it can be concluded that phosphate forms an ordered adsorbed structure in the presence of lithium cations on the Au(111) surface. The order of the structure decreases towards more positive potentials, where the mobility of the phosphate ions on the surface is higher and therefore, only a semi-ordered structure is imaged.

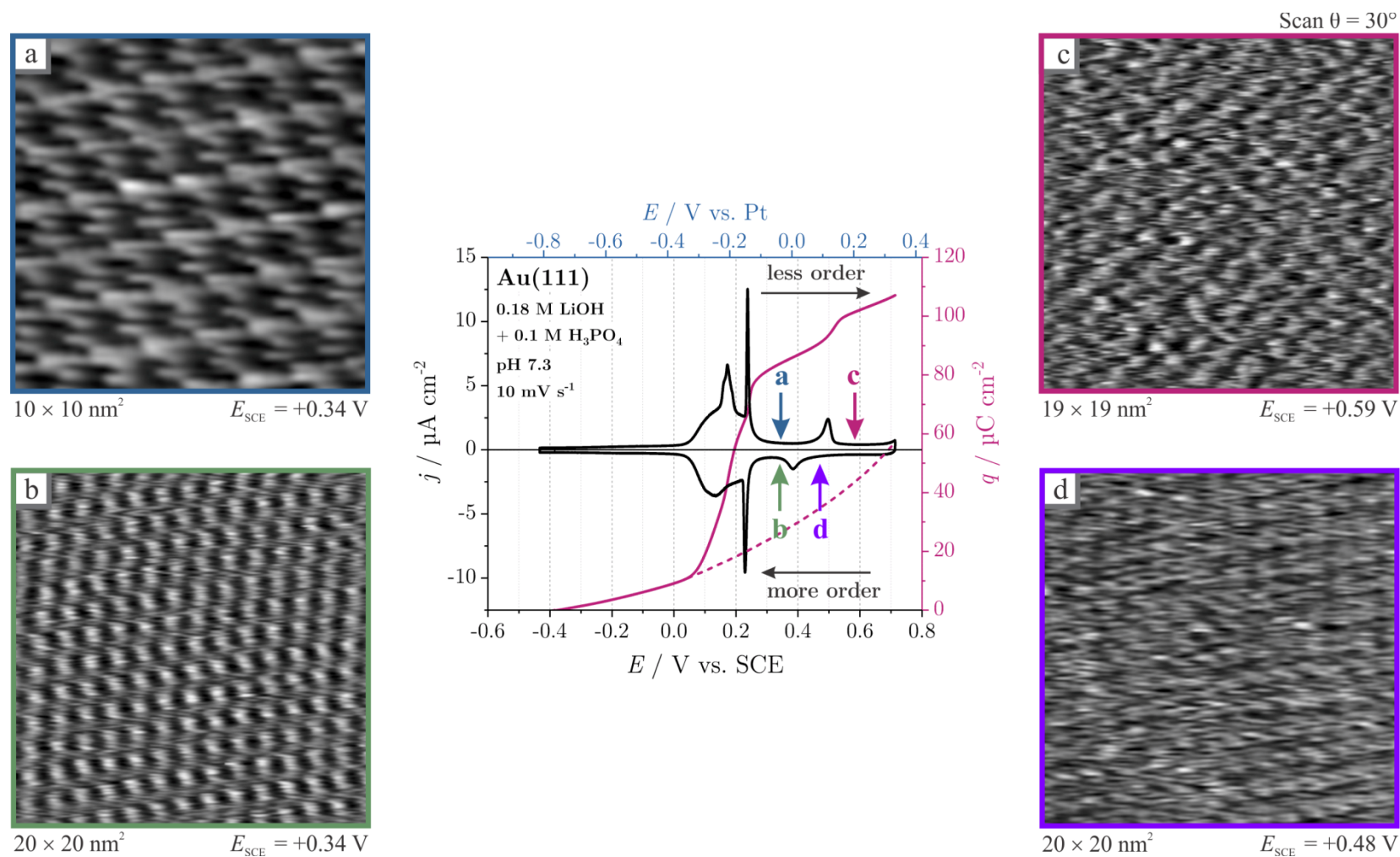


**Figure 6.9:** Current-potential curve for a Au(111) electrode in 0.1 M H<sub>3</sub>PO<sub>4</sub> + 0.18 M LiOH at pH 7.3. Scan rate 10 mVs<sup>-1</sup>. Courtesy of Johannes. M. Hermann. A series of *in-situ* STM images of a Au(111) electrode in 0.1 M H<sub>3</sub>PO<sub>4</sub> + 0.18 M LiOH representing structures of adsorbed phosphate that are (a) ordered: 10×10 nm<sup>2</sup>,  $E = 0.34$  V,  $U_T = -0.11$  V,  $I_T = 2$  nA, (b) ordered: 20×20 nm<sup>2</sup>,  $E = 0.34$  V,  $U_T = -0.11$  V,  $I_T = 5$  nA. (c) semi-ordered: 19×19 nm<sup>2</sup>,  $E = 0.59$  V,  $U_T = 0.26$  V,  $I_T = 7$  nA (Scan angle: 30°), (d) semi-ordered: 20×20 nm<sup>2</sup>,  $E = 0.48$  V,  $U_T = 0.15$  V,  $I_T = 7$  nA.

### 6.3 Influence of Alkali Metal Cations ( $K^+$ , $Na^+$ and $Li^+$ )

Although alkali metal cations in aqueous electrolytes are typically considered non-electroactive, this study indicates that they significantly contribute to the interfacial state of an electrode and hence, influence the adsorption behaviour of oxoanions like phosphates on the surface. This is in agreement with recent findings which have also reported an influence of alkali metal cations on electrocatalytic reactions.<sup>[220–223]</sup> The voltammetric response of the anionic adsorption on the Au(111) electrode in phosphate buffered solutions is influenced by the nature of the coadsorbed cations. This is probably due to the competition between the various phosphate species and the cationic species in solution. The mechanism through which the cations influence the adsorption behaviour of the phosphate anions is not clearly understood. It seems however, that they mainly affect the degree of the stability of an ordered structure on the surface.

At a given concentration and for  $6 < \text{pH} < 10$ , the observed trend by the alkali metal cation series is as follows:  $K^+$  does not induce the appearance of the phase transition spike(s) in the voltammogram while  $Na^+$  and  $Li^+$  do. The effect of the cation is comparatively more pronounced for the second pair of spikes/peaks at around 0.5 V which indicates that the order/disorder phase transition within the adsorbed phosphate layer is quite sensitive to the nature of the cation. In addition, the kinetic hindrance observed for the formation of the second phase transition in case of  $Li^+$  can be attributed to the larger cation size compared to  $Na^+$ . In both cases, the concentration of cationic species at the OHP seems essentially different. Calculations of the stability of the solvated alkali metal cations indicate that larger hydrated cations at the OHP are more energetically favoured than smaller ones.<sup>[222]</sup> Interestingly, the effect of cation size on the activity of  $CO_2$  electrochemical reduction was reported to be more pronounced for close-packed surfaces of Cu.<sup>[222]</sup> It is possible, that a similar effect can be found for the oxidation of formic acid; however, this should be more systematically investigated.

For  $K^+$ , no ordered structure of adsorbed phosphates was observed by STM (not shown) while for  $Na^+$  and for  $Li^+$ , ordered structures of distinct behaviour were imaged. These findings indicate the existence of specific anion-cation interactions. One fact to support this hypothesis is a previously reported shift in the wavenumber of some bands in the FTIR spectra of  $PO_4^{3-}$  and  $HPO_4^{2-}$  anions adsorbed on a Pt electrode, compared to the spectra obtained for the ions in solution.<sup>[66]</sup> It is also probable that in comparison to  $K^+$ , a stronger affinity exists between  $Na^+$  or  $Li^+$  and  $PO_4^{3-}$  or  $HPO_4^{2-}$  ions in solution.

## 7 Conclusions and Outlook

In order to optimize existing electrocatalytic systems, it is essential to understand the characteristics and the nature of electrified interface. This study shows that at a given electrode potential, the structure of the Au(111) surface is essentially determined by the nature and composition of the electrolyte. Combining both electrocatalysis and *in-situ* STM imaging is shown here to be an effective and unique way to gain a better understanding of the progress of the formation of surface reconstruction at different electrode potentials. The morphology of the reconstructed Au(111) surface is observed to depend not only on the preparation and the annealing temperatures but also on the potential applied. Despite the fact that Au electrodes in sulfuric acid media are one of the most well-established systems in electrocatalysis, interactions at the interface remain unexpectedly complicated.

The electrochemical behaviour of Au(111) in carboxylic acids (acetic and formic acid) and in phosphate buffer solutions has been studied by cyclic voltammetry and by *in-situ* STM. Measurements in acetic acid were performed first since unlike formic acid, acetate acid is not active on the gold surface. The specific adsorption of acetate and formate lifts the Au(111) surface reconstruction. A peak (step-up in current, in the case of formate) in the current-potential curve at relatively the same potential is attributed to a phase transition within their adsorbed layers. Because of the similarity of either anion in terms of geometry, both acetate and formate bind in a bidentate configuration and form a 2D structure on the unreconstructed Au(111) surface. Although parallel zigzag chains of an ordered structure are imaged for either  $C_1$  molecule, their nearest-neighbour distances and proposed structural models are essentially different. Nonetheless, the structures maintain relatively simple hexagonally closely packed unit cells.

In the case of acetate, two distinct structures (A-I and A-II) of different orientation are imaged. Structure A-I transforms with time to a more thermodynamically favoured structure (A-II) of  $CH_3COO_{ad}$ . Structure A-I forms on the surface with an intermediate

coverage ( $\sim 0.21$  ML) which with time increases to 0.25 ML for structure A-II. In the case of formate, the anion adsorbs on the surface with a coverage which lies somewhere between those obtained for acetate adsorption on Au(111). The difference in calculated coverages of structures F-I and F-III of  $\text{HCOO}_{\text{ad}}$  is affected by the presence of (i) weaker bound formate species and (ii) non-specifically adsorbed perchlorate species in solution, which are both probably not detected by STM. The difference in adsorption behaviour of acetate and formate could be a consequence of the difference in the chemical nature of either species. More specifically, the acetate anions having a methyl group. Nevertheless, both acetate and formate seem to strongly adsorb on the Au surface. In fact, mixed structures of either carboxylate while adsorbing onto the surface are also expected, which would then have a blocking effect on the electrocatalytic formic acid oxidation. Findings from this study show that the formation of parallel zigzag chains of an adsorbed adlayer on metallic surfaces is not only characteristic for formate but also a key feature for acetate and maybe other neighbouring carboxylates in the homologous series. The approach of studying the adsorption behaviour of unreactive adsorbates to understand those of reactive ones has been found to be extremely valuable and can be applied to other metallic surfaces.

Studying the specific adsorption of phosphate anions at metal surfaces is also essential since it too, could have a blocking effect on the electrocatalytic oxidation of formic acid. Unlike the case of sulfate adsorption, an additional spike is observed for phosphate adsorption owing to the polyprotic nature of phosphate. The spikes are related to phase transitions within adsorbed phosphate layers which are attributed to distinct coverages of ordered adlayer structures. Similar to  $\text{SO}_{4\text{ad}}$ ,  $\text{PO}_{4\text{ad}}$  prefers to bind to the surface in a tridentate configuration on top sites of Au(111) atoms. The coadsorption of a cationic species is necessary to stabilize the adsorbed structure, in which the role  $\text{H}_3\text{O}^+$  ions play in the adsorption of  $\text{SO}_4^-$  is analogous to that of  $\text{Na}^+$  ions in the adsorption of  $\text{PO}_4^{2-}$ . A potential dependence or ‘breathing effect’ on the adsorbed phosphate structures, at the U-shaped current profile is reported. A more compact structure (P-II) of adsorbed phosphate is observed positive of the second phase transition spike which is analogous to the  $(\sqrt{3} \times \sqrt{7})$  structure of adsorbed sulfate (S-III, positive of the phase transition spike). Since the margin of error is relatively large due to a time effect or a potential shift that is unavoidable unless a real reference electrode is used, further systematic studies are needed to clearly understand this behaviour. This study allows for a better understanding of the adsorbed structures of oxoanions on Au(111). However, information on the kinetics



involved in such adsorption processes remains scarce. For example, identifying the influence of oxoanion adsorption on island growth or observing the effect of defects on structure formation could be extremely beneficial.

Although no definitive conclusion can be drawn from this work on the anionic species responsible for the adsorption states of phosphate on the Au(111) surface, the nature of the cationic species in solution seems to play a major role on their adsorption behaviour. Unexpectedly, the behaviour is strongly dependent on the type of alkali metal cation ( $K^+$ ,  $Na^+$  and  $Li^+$ ) in solutions of the same pH. Direct evidence regarding the stabilization of the adsorbed structures on the surface has been revealed by *in-situ* STM. For phosphate buffered solutions, the nature of the cations monotonously influences the adsorbed phosphate structures. For  $K^+$  ions, no ordered structure is observed while for  $Na^+$  and  $Li^+$  ions, structures which resemble a  $(\sqrt{3} \times \sqrt{7})$  arrangement are imaged. In the case of  $Li^+$  ions, further rearrangement in the adsorbed phosphate layer starts at more negative potentials. It is observed that larger cations like  $Na^+$  and  $Li^+$  have a stronger effect on the adsorption behaviour of oxoanions than smaller cations like  $K^+$  do.

Although cations are commonly considered as strongly solvated and do not significantly affect reactions, this study shows that the anion-cation interactions at the electrode/electrolyte interface can influence the adsorption of relevant reaction intermediates. As a consequence, the effect of anions, cations and solvent molecules in electrochemical reactions is key to understanding adsorption processes. While progress has been made in the attempt to explain the effect of cations on the adsorption behaviour of oxoanions, it remains quite difficult to predict, solely from voltammetric data and *in-situ* STM, the possible interactions between anions and cations at the electrode surface.

Besides the nature of the electrode surface, the electrocatalytic activity could significantly be affected by the composition of the electrolyte. A model which correctly describes the mechanism of an electrocatalytic reaction on metallic surfaces must consider the effect of the anions, cations and solvent molecules which may not themselves be directly involved in a reaction. Studying the adsorption of active and spectator species at the electrode surface is important since electrocatalytic reactions involve at least one adsorption step. The structural arrangement and competition of adspecies on the Au electrode surface plays a key role on the oxidation kinetics during the formic acid electrocatalytic reaction. This is mainly because the adsorption of formate occurs simultaneously with the oxidation process itself.



# Bibliography

- [1] O. M. Magnussen, *Chem. Rev.* **2002**, *102*, 679–725.
- [2] A. Hamelin, in *Mod. Asp. Electrochem. Vol. 16* (Eds.: B.E. Conway, R.E. White, J.O. Bockris), Plenum Press, New York, **1985**.
- [3] S. Yoshimoto, K. Itaya, *Annu. Rev. Anal. Chem.* **2013**, *6*, 213–235.
- [4] J. C. F. Rodriguez-Reyes, C. G. F. Siler, W. Liu, A. Tkatchenko, C. M. Friend, R. J. Madix, *J. Am. Chem. Soc.* **2014**, *136*, 13333–13340.
- [5] J. V. Perales-Rondón, E. Herrero, J. M. Feliu, *Electrochim. Acta* **2014**, *140*, 511–517.
- [6] J. Souza-Garcia, C. Angelucci, *The Role of Anions in Single Crystal Platinum Cyclic Voltammograms*, **2015**.
- [7] O. M. Magnussen, J. Hagebock, R. J. Behm, *Faraday Discuss.* **1992**, *94*, 329–338.
- [8] F. C. Simeone, D. M. Kolb, S. Venkatachalam, T. Jacob, *Angew. Chemie - Int. Ed.* **2007**, *46*, 8903–8906.
- [9] A. Cuesta, M. Kleinert, D. M. Kolb, *Current* **2000**, 5684–5690.
- [10] D. M. Kolb, N. Batina, A. S. Dakkouri, in *Nanoscale Probes of the Solid/Liquid Interface* (Ed.: A.A. Gewirth; H. Siegenthaler), Springer Netherlands, Dordrecht, **1995**, pp. 263–284.
- [11] J. M. Hermann, Y. Mattausch, A. Weiß, T. Jacob, L. A. Kibler, *J. Electrochem. Soc.* **2018**, *165*, J3192–J3198.
- [12] W. Ma, S. Xie, X. G. Zhang, F. Sun, J. Kang, Z. Jiang, Q. Zhang, D. Y. Wu, Y. Wang, *Nat. Commun.* **2019**, *10*, 1–10.
- [13] K. Holst-Olesen, M. Reda, H. A. Hansen, T. Vegge, M. Arenz, *ACS Catal.* **2018**, *8*, 7104–7112.
- [14] K. Zhou, Y. Li, *Angew. Chem. Int. Ed. Engl.* **2012**, *51*, 602–613.
- [15] C. G. F. Siler, T. Cremer, J. C. F. Rodriguez-Reyes, C. M. Friend, R. J. Madix, *ACS Catal.* **2014**, *4*, 3281–3288.
- [16] S. Chen, D. Lee, M. Schell, *Electrochim. Acta* **2001**, *46*, 3481–3492.
- [17] P. Rodriguez, Y. Kwon, M. T. M. Koper, *Nat. Chem.* **2011**, *4*, 177–182.

- [18] N.-T. Suen, S.-F. Hung, Q. Quan, N. Zhang, Y.-J. Xu, H. M. Chen, *Chem. Soc. Rev.* **2017**, *46*, 337–365.
- [19] S. Z. Qiao, Y. Zheng, Y. Jiao, M. Jaroniec, S. Z. Qiao, *Angew. Chemie - Int. Ed.* **2015**, *54*, 52–65.
- [20] C. Schlaup, S. Horch, *Surf. Sci.* **2013**, *608*, 44–54.
- [21] K. Itaya, *Electrochemistry* **2015**, *83*, 670–679.
- [22] B. Han, Z. Li, T. Wandlowski, *Anal. Bioanal. Chem.* **2007**, *388*, 121–129.
- [23] Y. Lin, G. B. Pan, G. J. Su, X. H. Fang, L. J. Wan, C. L. Bai, *Langmuir* **2003**, *19*, 10000–10003.
- [24] Y. Shingaya, M. Ito, *J. Electroanal. Chem.* **1999**, *467*, 299–306.
- [25] A. S. Dakkouri, M. Dietterle, D. M. Kolb, in *Adv. Solid State Physics, Vol. 36* (Ed.: R. Helbig), Springer, Heidelberg, **1997**.
- [26] D. M. Kolb, F. C. Simeone, *Scanning Tunneling Microsc. Surf. Sci. Nanosci. Catal.* **2010**, 119–146.
- [27] D. M. Kolb, *Angew. Chemie Int. Ed.* **2001**, *40*, 1162–1181.
- [28] N. J. Tao, S. M. Lindsay, **1991**, *70*, 5141–5143.
- [29] Y. He, E. Borguet, *J. Phys. Chem. C* **2011**, *115*, 5726–5731.
- [30] L. A. Kibler, J. M. Hermann, A. Abdelrahman, A. A. El-Aziz, T. Jacob, *Curr. Opin. Electrochem.* **2018**, *9*, 265–270.
- [31] Y. Grunder, J. Beane, A. Kolodziej, C. Lucas, P. Rodriguez, *Surfaces* **2019**, *2*, 145–158.
- [32] T. Kondo, J. Zegenhagen, S. Takakusagi, K. Uosaki, *Surf. Sci.* **2015**, *631*, 96–104.
- [33] G. J. Edens, X. Gao, M. J. Weaver, *J. Electroanal. Chem.* **1994**, *375*, 357–366.
- [34] M. Weber, I. R. de Moraes, A. J. Motheo, F. C. Nart, *Colloids Surfaces A Physicochem. Eng. Asp.* **1998**, *134*, 103–111.
- [35] Z. Shi, J. Lipkowski, M. Gamboa, P. Zelenay, A. Wieckowski, *J. Electroanal. Chem.* **1994**, *366*, 317–326.
- [36] I. R. de Moraes, F. C. Nart, *J. Electroanal. Chem.* **1999**, *461*, 110–120.
- [37] T. Wandlowski, K. Ataka, S. Pronkin, D. Diesing, *Electrochim. Acta* **2004**, *49*, 1233–1247.
- [38] D. C. Grinter, T. Woolcot, C. L. Pang, G. Thornton, *J. Phys. Chem. Lett.* **2014**, *5*, 4265–4269.
- [39] S. L. Silva, T. M. Pham, A. A. Patel, S. Haq, F. M. Leibsle, *Surf. Sci.* **2000**, *452*, 79–94.
- [40] F. Hiebel, B. Shong, W. Chen, R. J. Madix, E. Kaxiras, C. M. Friend, *Nat. Commun.* **2016**, *7*, 1–8.
- [41] P. Broekmann, M. Wilms, M. Kruft, C. Stuhlmann, K. Wandelt, *J. Electroanal.*

- Chem.* **1999**, *467*, 307–324.
- [42] A. Javier, Y. Kim, J. Soriaga, *Phil. Sci. Lett* **2011**.
- [43] M. Wilms, P. Broekmann, M. Kruft, Z. Park, C. Stuhlmann, K. Wandelt, *Surf. Sci.* **1998**, *402–404*, 83–86.
- [44] Z. Li, F. Calaza, F. Gao, W. T. Tysoe, *Surf. Sci.* **2012**, *606*, 1934–1941.
- [45] S. Gilman, *Electrochim. Acta* **2012**, *65*, 141–148.
- [46] O. Karis, J. Hasselström, N. Wassdahl, M. Weinelt, A. Nilsson, M. Nyberg, L. G. M. Pettersson, J. Stöhr, M. G. Samant, *J. Chem. Phys.* **2000**, *112*, 8146–8155.
- [47] Y. Chen, M. Heinen, Z. Jusys, R. J. Behm, *Langmuir* **2006**, *22*, 10399–10408.
- [48] V. Grozovski, F. J. Vidal-Iglesias, E. Herrero, J. M. Feliu, *ChemPhysChem* **2011**, *12*, 1641–1644.
- [49] M. Osawa, K. I. Komatsu, G. Samjeské, T. Uchida, T. Ikeshoji, A. Cuesta, C. Gutiérrez, *Angew. Chemie - Int. Ed.* **2011**, *50*, 1159–1163.
- [50] L. A. Kibler, M. Al-Shakran, *J. Phys. Chem. C* **2016**, *120*, 16238–16245.
- [51] A. Berná, J. M. Delgado, J. M. Orts, A. Rodes, J. M. Feliu, *Electrochim. Acta* **2008**, *53*, 2309–2321.
- [52] A. Abdelrahman, J. M. Hermann, T. Jacob, L. A. Kibler, *ChemPhysChem* **2019**, *20*, 1–9.
- [53] W. Gao, E. H. Song, Q. Jiang, T. Jacob, *Chem. - A Eur. J.* **2014**, *20*, 11005–11012.
- [54] A. Cuesta, G. Cabello, F. W. Hartl, M. Escudero-Escribano, C. Vaz-Domínguez, L. A. Kibler, M. Osawa, C. Gutiérrez, *Catal. Today* **2013**, *202*, 79–86.
- [55] M. Shimomura, T. K. Kawaguchi, Y. Fukuda, K. Murakami, A. Z. Alzahrani, G. P. Srivastava, *Phys. Rev. B - Condens. Matter Mater. Phys.* **2009**, *80*, 3–5.
- [56] J. Joo, T. Uchida, A. Cuesta, M. T. M. Koper, M. Osawa, *J. Am. Chem. Soc.* **2013**, *135*, 4–7.
- [57] S. Brimaud, J. Solla-Gullón, I. Weber, J. M. Feliu, R. J. Behm, *ChemElectroChem* **2014**, *1*, 1075–1083.
- [58] J. Joo, T. Uchida, A. Cuesta, M. T. M. Koper, M. Osawa, *Electrochim. Acta* **2014**, *129*, 127–136.
- [59] J. V. Perales-Rondón, S. Brimaud, J. Solla-Gullón, E. Herrero, R. Jürgen Behm, J. M. Feliu, *Electrochim. Acta* **2015**, *180*, 479–485.
- [60] M. Talha, Y. Ma, Y. Lin, A. Singh, W. Liu, X. Kong, *New J. Chem.* **2019**, *43*, 1943–1955.
- [61] J. Jiang, D. I. Kim, P. Dorji, S. Phuntsho, S. Hong, H. K. Shon, *Process Saf. Environ. Prot.* **2019**, *126*, 44–52.
- [62] S. Carda-Broch, M. C. García-Alvarez-Coque, M. J. Ruiz-Angel, *J. Chromatogr. A* **2018**, *1559*, 112–117.
- [63] A. Abdelrahman, J. M. Hermann, L. A. Kibler, *Electrocatalysis* **2017**, *8*, 509–517.

- [64] Y. J. Deng, G. K. H. Wiberg, A. Zana, M. Arenz, *Electrochim. Acta* **2016**, *204*, 78–83.
- [65] F. C. Nart, T. Iwasita, *Electrochim. Acta* **1992**, *37*, 385–391.
- [66] V. B. Paulissen, C. Korzeniewski, *J. Electroanal. Chem.* **1990**, *290*, 181–189.
- [67] M. Yaguchi, T. Uchida, K. Motobayashi, M. Osawa, *J. Phys. Chem. Lett.* **2016**, *7*, 3097–3102.
- [68] M. Weber, F. C. Nart, *Electrochim. Acta* **1996**, *41*, 653–659.
- [69] J. Mostany, P. Martínez, V. Climent, E. Herrero, J. M. Feliu, *Electrochim. Acta* **2009**, *54*, 5836–5843.
- [70] R. Gisbert, G. García, M. T. M. Koper, *Electrochim. Acta* **2010**, *55*, 7961–7968.
- [71] W. M. Haynes, *CRC Handbook of Chemistry and Physics*, CRC Press, Boca Raton, FL, **2014**.
- [72] T. Cremer, C. G. F. Siler, J. C. F. Rodríguez-Reyes, C. M. Friend, R. J. Madix, *J. Phys. Chem. Lett.* **2014**, *5*, 1126–1130.
- [73] E. Hwang, D. H. Kim, *J. Phys. Chem. C* **2017**, *121*, 18584–18592.
- [74] I. Villegas, M. J. Weaver, *J. Chem. Phys.* **1994**, *101*, 1648–1660.
- [75] Y. Shingaya, M. Ito, *Electrochim. Acta* **1998**, *44*, 889–895.
- [76] A. Hamelin, *J. Electroanal. Chem.* **1982**, *142*, 299–316.
- [77] L. A. Kibler, *Int. Soc. Electrochem.* **2003**, 1–56.
- [78] D. M. Kolb, *Prog. Surf. Sci.* **1996**, *51*, 109–173.
- [79] A. F. Hollemann; E. Wiberg, *Lehrbuch Der Anorganischen Chemie*, Walter De Gruyter, Berlin/New York, **1995**.
- [80] M. Noel, K. I. Vasu, *Cyclic Voltammetry and the Frontiers of Electrochemistry*, Aspect Publications, London, **1990**.
- [81] B. Speiser, *Chemie unserer Zeit* **1981**, *15*, 62–67.
- [82] V. S. Bagotsky, in *Fundam. Electrochem.*, John Wiley & Sons, Inc., Hoboken, New Jersey, **2006**, pp. 191–217.
- [83] Y. Liang, J. H. K. Pfisterer, D. McLaughlin, C. Csoklich, L. Seidl, A. S. Bandarenka, O. Schneider, *Small Methods* **2018**, *1800387*, 1–27.
- [84] Y. Geng, P. Li, J. Li, X. Zhang, Q. Zeng, C. Wang, *Coord. Chem. Rev.* **2017**, *337*, 145–177.
- [85] A. A. Gewirth, B. K. Niece, *Chem. Rev.* **1997**, *97*, 1129–1162.
- [86] A. Alkauskas, **2006**, 1–131.
- [87] E. Riedel, C. Janiak, *Anorganische Chemie*, Boston: De Gruyter, Berlin, **2015**.
- [88] S. K. Chatterjee, *Crystallography and the World of Symmetry*, Springer Berlin, Heidelberg, **2008**.
- [89] A. Zangwill, *Physics at Surfaces*, Cambridge University Press, Cambridge, **1988**.

- 
- [90] M. Kleinert, Strukturuntersuchungen Mit Dem Rastertunnelmikroskop an Gold- Und Platineinkristallelektroden, Universität Ulm, **2001**.
- [91] D. N. Batchelder, R. O. Simmons, *J. Appl. Phys.* **1965**, *36*, 2864–2868.
- [92] M. Henzler; W. Göpel, *Oberflächenphysik Des Festkörpers*, Vieweg+Teubner Verlag, Teubner Stuttgart, **1991**.
- [93] G. A. Somorjai, *Chemistry in Two Dimensions: Surfaces*, Cornell University Press, Ithaca, New York, **1981**.
- [94] P. J. Estrup, in *Chem. Phys. Solid Surfaces V* (Eds.: R. Vanselow, R. Howe), Springer-Verlag Berlin Heidelberg, Berlin, **1984**, pp. 205–230.
- [95] G. A. Somorjai, *Introduction to Surface Chemistry and Catalysis*, Wiley-Interscience, New York, **1994**.
- [96] A. S. Dakkouri, D. M. Kolb, in *Interfacial Electrochem. Theory, Exp. Appl.* (Ed.: A. Więckowski), Marcel Dekker, Inc., New York, **1999**, pp. 151–173.
- [97] G. Ertl, *Surf. Sci.* **1985**, *152–153*, 328–337.
- [98] J. Clavilier, R. Faure, G. Guinet, R. Durand, *J. Electroanal. Chem.* **1980**, *107*, 205–209.
- [99] N. Batina, A. S. Dakkouri, D. M. Kolb, *J. Electroanal. Chem.* **1994**, *370*, 87–94.
- [100] A. . Dakkouri, D. M. Kolb, in *Interfacial Electrochem. Theory Exp. Appl.* (Ed.: A. Wieckowski), **1999**, pp. 151–173.
- [101] H. Melle, E. Menzel, *Zeitschrift fur Naturforsch. - Sect. A J. Phys. Sci.* **1978**, *33*, 282–289.
- [102] K. Takayanagi, *Ultramicroscopy* **1982**, *8*, 145–161.
- [103] U. Harten, A. M. Lahee, J. P. Toennies, C. Woll, *Phys. Rev. Lett.* **1985**, *54*, 2619–2622.
- [104] M. Giesen, G. Beltramo, S. Dieluweit, J. Müller, H. Ibach, W. Schmickler, *Surf. Sci.* **2005**, *595*, 127–137.
- [105] H. Ibach, *Physics of Surfaces and Interfaces*, Springer-Verlag Berlin Heidelberg, Berlin, **2006**.
- [106] D. M. Kolb, J. Schneider, *Surf. Sci.* **1985**, *162*, 764–775.
- [107] B. M. Ocko, J. Wang, A. Davenport, H. Isaacs, *Phys. Rev. Lett.* **1990**, *65*, 1466–1469.
- [108] X. Gao, A. Hamelin, M. J. Weaver, *Phys. Rev. Lett.* **1991**, *67*, 618–621.
- [109] X. Gao, G. J. Edens, A. Hamelin, M. J. Weaver, *Surf. Sci.* **1993**, *296*, 333–351.
- [110] D. M. Kolb, A. . Dakkouri, N. Batina, in *Nanoscale Probes of the Solid/Liquid Interface* (Eds.: A.A. Gewirth, H. Siegenthaler), **1995**, pp. 263–264.
- [111] A. Hamelin, L. Stoicoviciu, G. J. Edens, X. Gao, M. J. Weaver, *J. Electroanal. Chem.* **1994**, *365*, 47–57.
- [112] A. S. Dakkouri, R. Randler, D. M. Kolb, in *Proc. Symp. Electerochemical Double*

- Layer* (Eds.: C. Korzeniewski, B.E. Conway), The Electrochemical Society, Inc., Pennington, NJ, **1997**, pp. 13–31.
- [113] E. Budevski; G. Staikov; W.J. Lorenz, *Electrochemical Phase Formation and Growth*, VCH Verlagsgesellschaft, Weinheim, **1996**.
- [114] W. Kossel, *Zur Theorie Des Kristallwachstums*, Göttingen, **1927**.
- [115] G. A. Somorjai; Y. Li, *Introduction to Surface Chemistry and Catalysis*, Wiley & Sons Ltd, New York, **2010**.
- [116] T. A. Baker, C. M. Friend, E. Kaxiras, *J. Phys. Chem. C* **2009**, *113*, 3232–3238.
- [117] C. A. Scamehorn, N. M. Harrison, M. I. McCarthy, *J. Chem. Phys.* **1994**, *101*, 1547–1554.
- [118] A. J. Bard, H. D. Abruiia, C. E. Chidsey, L. R. Faulkner, S. W. Feldberg, K. Itaya, M. Majda, O. Melroy, R. W. Murray, M. D. Porter, et al., *J. Phys. Chem. J. Phys. Chem.* **1993**, *97*, 7147–7173.
- [119] C. H. Hamann; W. Vielstich, *Elektrochemie*, Wiley-VCH, Weinheim, **2005**.
- [120] P. W. Atkins; J. de Paula, *Kurzlehrbuch Physikalische Chemie*, Wiley-VCH, Weinheim, **2008**.
- [121] G. Wedler, *Lehrbuch Der Physikalischen Chemie*, Wiley-VCH, Weinheim, **2007**.
- [122] H. Helmholtz, *Ann. der Phys. und Chemie* **1879**, *7*, 337–382.
- [123] D. M. Kolb, **2002**, *500*, 722–740.
- [124] B. Timmer, M. Sluyters-Rehbach, J. H. Sluyters, *Surf. Sci.* **1969**, *18*, 44–61.
- [125] W. Schmickler, *Grundlagen Der Elektrochemie*, Vieweg & Sohn Verlagsgesellschaft MbH, Braunschweig-Wiesbaden, **1996**.
- [126] R. Holze, *Leitfaden Der Elektrochemie*, Vieweg+Teubner Verlag, Stuttgart, **1998**.
- [127] J.O'M. Bockris; A.K.N. Reddy; M.E. Gamboa-Aldeco, *Modern Electrochemistry 2A*, Springer US, New York, **2000**.
- [128] S. Trasatti, O. A. Petrii, *Pure Appl. Chem.* **1991**, *63*, 711–734.
- [129] U. Hartmann, *Scanning Tunneling Microscopy and Spectroscopy, Theory, Techniques and Applications*, VCH Publishers, Inc., New York, **1994**.
- [130] M. Soriaga, in *Front. Blcetrochemistry, Vol. 2* (Eds.: J. Lipkowski, P.N. Ross), VCH Publishers, Inc., New York, **1993**.
- [131] J. Liu, Z. Xu, B. Zhu, X. Du, Y. Yang, C. Yi, Z. Zhang, C. Cai, J. Li, *RSC Adv.* **2018**, *8*, 19103–19115.
- [132] M. Petri, Einfluß Verschiedener Additive Auf Die Elektrolytische Kupferabscheidung Auf Au(111), Universität Ulm, **2003**.
- [133] F. C. Simeone, **2008**.
- [134] C. Wöll, S. Chiang, R. J. Wilson, P. H. Lippel, *Phys. Rev. B* **1989**, *39*, 7988–7991.
- [135] P. Mrozek, M. Han, Y. E. Sung, A. Wieckowski, *Surf. Sci.* **1994**, *319*, 21–33.



- [136] D. A. Huckaby, L. Blum, *J. Electroanal. Chem.* **1991**, *315*, 255–261.
- [137] F. Silva, M. J. Sottomayor, A. Martins, *J. Electroanal. Chem.* **1994**, *375*, 395–399.
- [138] M. Nowicki, A. Emundts, J. Werner, G. Pirug, H. P. Bonzel, *Surf. Rev. Lett.* **2000**, *7*, 25–36.
- [139] A. R. Alemozafar, R. J. Madix, *J. Phys. Chem. B* **2004**, *108*, 14374–14383.
- [140] S. Haq, F. M. Leibsle, *Surf. Sci.* **1996**, *355*, DOI 10.1016/0039-6028(96)00514-6.
- [141] J. M. Phillips, F. M. Leibsle, A. J. Holder, T. Keith, *Surf. Sci.* **2003**, *545*, 1–7.
- [142] J. X. Wang, G. M. Watson, B. M. Ocko, *J. Phys. Chem.* **1996**, *100*, 6672–6677.
- [143] N. García, V. Climent, J. M. Orts, J. M. Feliu, A. Aldaz, *ChemPhysChem* **2004**, *5*, 1221–1227.
- [144] L. A. Kibler, M. Al-shakran, *J. Phys. Chem. C* **2016**, *120*, 16238–16245.
- [145] R. Kaischew, *Zeitschrift für Phys.* **1936**, *102*, 684–690.
- [146] C. Gerber, G. Binnig, H. Fuchs, O. Marti, H. Rohrer, *Rev. Sci. Instrum.* **1986**, *57*, 221–224.
- [147] G. Binnig, H. Rohrer, C. Gerber, E. Weibel, *Appl. Phys. Lett.* **1982**, *40*, 178–180.
- [148] L. A. Bottomley, J. E. Coury, P. N. First, *Anal. Chem.* **1996**, *68*, 185R–230R.
- [149] J. Schneir, R. Sonnenfeld, P. K. Hansma, J. Tersoff, *Phys. Rev. B - Condens. Matter* **1986**, *34*, 4979–4984.
- [150] R. Sonnenfeld, P. K. Hansma, B. Drake, T. Albrecht, C. Quate, P. Hansma, *Science (80-. )*. **1986**, *232*, 211–213.
- [151] R. Sonnenfeld, B. C. Schardt, *Appl. Phys. Lett.* **1986**, *49*, 1172–1174.
- [152] R. J. Behm, N. García, H. Rohrer, Eds. , *Scanning Tunneling Microscopy and Related Methods*, Springer Netherlands, **1990**.
- [153] R. Wiesendanger, *Scanning Probe Microscopy and Spectroscopy: Methods and Applications*, Cambridge University Press, Cambridge, **1994**.
- [154] J. G. Simmons, *J. Appl. Phys.* **1963**, *34*, 1793–1803.
- [155] M. Schweizer, Struktur Und Elektrochemie von Alkanthiolat-Monolagen Auf Den (100)-Oberächen von Gold Und Silber, Universität Ulm, **2004**.
- [156] P. K. Hansma, J. Tersoff, *J. Appl. Phys.* **1987**, *61*, R1–R23.
- [157] G. Binnig, H. Fuchs, C. Gerber, H. Rohrer, E. Stoll, E. Tosatti, *Europhys. Lett.* **1986**, *1*, 31–36.
- [158] S.-I. Park, C. F. Quate, *Appl. Phys. Lett.* **1986**, *48*, 112–114.
- [159] J. Ahn, M. Pyo, *Bull. Korean Chem. Soc.* **2000**, *21*, 644–646.
- [160] D. M. Kolb, R. J. Nichols, R. J. Behm, in *Electrified Interfaces Physics, Chem. Biol.* (Ed.: R. Guidelli), Springer, Dordrecht, **1992**.
- [161] E. Herrero, L. J. Buller, D. Abruna, *Chem. Rev.* **2001**, *101*, 1897–1930.
- [162] K. Itaya, E. Tomita, *Surf. Sci.* **1988**, *201*, 507–512.

- [163] R. Hoyer, Struktur Und Reaktivität Bimetallischer Einkristallelektroden Der Platin-Metalle, Universität Ulm, **2004**.
- [164] C. E. Bach, R. J. Nichols, W. Beckmann, H. Meyer, A. Schulte, J. O. Besenhard, **1993**, *140*, 1281–1284.
- [165] Z.-X. Xie, D. M. Kolb, **2000**, *481*, 177–182.
- [166] R. J. Colton, S. M. Baker, R. J. Driscoll, M. G. Youngquist, J. D. Baldeschwieler, W. J. Kaiser, *J. Vac. Sci. Technol. A Vacuum, Surfaces, Film.* **1987**, *6*, 349–353.
- [167] D. M. Kolb, *Electrochim. Acta* **2000**, *45*, 2387–2402.
- [168] L. A. Kibler, Elektrochemie an Wohldefinierten Edelmetalloberflächen, Universität Ulm, **2000**.
- [169] D. Dickertmann, F. D. Koppitz, J. W. Schultze, *Electrochim. Acta* **1976**, *21*, 967–971.
- [170] D. Pletcher, *A First Course in Electrode Processes*, The Royal Society Of Chemistry, Cambridge, **2009**.
- [171] R. G. Compton, C. E. Banks, Eds. , *Understanding Voltammetry*, Imperial College Press, London, **2011**.
- [172] A. Reitzle, Untersuchungen Zur Elektrochemischen Metallabscheidung Auf N-Si(111): H-Elektroden, Universität Ulm, **2003**.
- [173] D. W. Pohl, *IBM J. Res. Dev.* **1986**, *30*.
- [174] T. Will, Untersuchungen Zur Kupferabscheidung Auf Au(111) Elektroden: Eine in-Situ STM Studie, Universität Ulm, **1994**.
- [175] M. A. Schneeweiß, In Situ Rastertunnelmikroskopie Studien Zur Anodischen Goldoxidation Und Zur Adsorption von Aminothiophenolen Auf Au(111), Universität Ulm, **1997**.
- [176] J. Wintterlin, Struktur Und Reaktivität Einer Metalloberfläche - Eine Untersuchung Mit Dem Rastertunnelmikroskop Am System Al(111)/Sauerstoff, Freie Universität Berlin, **1988**.
- [177] C. Vaz-Domínguez, M. Escudero-Escribano, A. Cuesta, F. Prieto-Dapena, C. Cerrillos, M. Rueda, *Electrochem. commun.* **2013**, *35*, 61–64.
- [178] B. Madry, I. Morawski, T. Kosmala, K. Wandelt, M. Nowicki, *Top. Catal.* **2018**, *61*, 1335–1349.
- [179] U. Zhumaeva, A. Rudnev, J.-F. Li, A. Kuzume, T.-H. Vu, T. Wandlowski, *Electrochim. Acta* **2013**, *112*, 853–863.
- [180] D. S. Corrigan, E. K. Krauskopf, L. M. Rice, A. Wieckowski, M. J. Weaver, *J. Phys. Chem.* **1988**, *92*, 1596–1601.
- [181] M. Dietterle, T. Will, D. M. Kolb, *Surf. Sci.* **1995**, *327*, DOI 10.1016/0039-6028(95)00033-X.
- [182] S. Dieluweit, M. Giesen, *J. Electroanal. Chem.* **2002**, *121*, 27–42.

- 
- [183] S. Dieluweit, M. Giesen, *J. Phys. Condens. Matter* **2002**, *14*, 4211–4225.
- [184] T. Fukuda, A. Aramata, *J. Electroanal. Chem.* **1999**, *467*, 112–120.
- [185] N. M. Marković, C. A. Lucas, A. Rodes, V. Stamenković, P. N. Ross, *Surf. Sci.* **2002**, *499*, DOI 10.1016/S0039-6028(01)01821-0.
- [186] J. X. Wang, I. K. Robinson, B. M. Ocko, R. R. Adzic, *J. Phys. Chem. B* **2005**, *109*, 24–26.
- [187] Y. V. Tolmachev, A. Menzel, A. V. Tkachuk, Y. S. Chu, H. You, *Electrochem. Solid-State Lett.* **2004**, *7*, 23–26.
- [188] I. Fromondi, H. Zhu, Z. Feng, D. Scherson, *J. Phys. Chem. C* **2014**, *118*, 27901–27910.
- [189] I. Fromondi, D. Scherson, *Faraday Discuss.* **2008**, *140*, 59–68.
- [190] E. A. Batista, T. Iwasita, W. Vielstich, *J. Phys. Chem. B* **2004**, *108*, 14216–14222.
- [191] P. N. Ross, C. A. Lucas, N. M. Markovic, *Surf. Sci.* **1999**, *425*, L381–L386.
- [192] F. T. Wagner, T. E. Moylan, S. J. Schmieg, *Surf. Sci.* **1988**, *195*, 403–428.
- [193] Y. Zhang, M. J. Weaver, *Langmuir* **1993**, *9*, 1397–1403.
- [194] G. L. Beltramo, T. E. Shubina, M. T. M. Koper, *ChemPhysChem* **2005**, *6*, 2597–2606.
- [195] A. Capon, R. Parsons, *J. Electroanal. Chem. Interfacial Electrochem.* **1973**, *44*, 239–254.
- [196] M. A. Schneeweiss, D. M. Kolb, *Solid State Ionics* **1997**, *94*, 171–179.
- [197] D. V. Tripkovic, D. Strmcnik, D. van der Vliet, N. M. Markovic, V. Stamenkovic, *Faraday Discuss.* **2008**, *140*, 25–40.
- [198] B. E. Conway, *Prog. Surf. Sci.* **1995**, *49*, 331–452.
- [199] H. Angerstein-Kozłowska, B. E. Conway, *J. Electroanal. Chem.* **1987**, *228*, 429–453.
- [200] K. I. Ataka, T. Yotsuyanagi, M. Osawa, *J. Phys. Chem.* **1996**, *100*, 10664–10672.
- [201] U. E. Zhumaev, A. S. Lai, I. V. Pobelov, A. Kuzume, A. V. Rudnev, T. Wandlowski, *Electrochim. Acta* **2014**, *146*, 112–118.
- [202] T. Fujitani, Y. Choi, M. Sano, Y. Kushida, J. Nakamura, *J. Phys. Chem. B* **2000**, *104*, 1235–1240.
- [203] A. Hamelin, *J. Electroanal. Chem.* **1996**, *407*, 1–11.
- [204] W. S. Sim, P. Gardner, D. A. King, *J. Phys. Chem.* **1996**, 12509–12516.
- [205] A. Chutia, I. P. Silverwood, M. R. Farrow, D. O. Scanlon, P. P. Wells, M. Bowker, S. F. Parker, C. R. A. Catlow, *Surf. Sci.* **2016**, *653*, 45–54.
- [206] J. R. B. Gomes, J. A. N. F. Gomes, *Surf. Sci.* **1999**, *432*, 279–290.
- [207] T. H. Vu, T. Wandlowski, *J. Electron. Mater.* **2017**, *46*, 3463–3471.
- [208] E. A. Braude, F. C. Nachod, J. G. Hoffman, *Phys. Today* **1956**, *9*, 22–22.

- [209] Y. B. Song, D. T. Chin, *Electrochim. Acta* **2002**, *48*, 349–356.
- [210] T. H. Vu, T. Wandlowski, *J. Electroanal. Chem.* **2016**, *776*, 40–48.
- [211] A. Berná, A. Rodes, J. M. Feliu, *Electrochim. Acta* **2004**, *49*, 1257–1269.
- [212] A. Berná, J. M. Delgado, J. M. Orts, A. Rodes, J. M. Feliu, *Langmuir* **2006**, *22*, 7192–7202.
- [213] A. Berná, A. Rodes, J. M. Feliu, *J. Electroanal. Chem.* **2004**, *563*, 49–62.
- [214] J. M. Delgado, A. Berná, J. M. Orts, A. Rodes, J. M. Feliu, *J. Phys. Chem. C* **2007**, *111*, 9943–9952.
- [215] K. J. Powell, P. L. Brown, R. H. Byrne, T. Gajda, G. Hefter, S. Sjöberg, H. Wanner, *Pure Appl. Chem.* **2005**, *77*, 739–800.
- [216] T. Langkau, H. Baltruschat, *Electrochim. Acta* **1998**, *44*, 909–918.
- [217] F. Silva, A. Martins, *J. Electroanal. Chem.* **1999**, *467*, 335–341.
- [218] T. Fuchigami, M. Atobe, S. Inagi, *Fundamentals and Applications of Organic Electrochemistry: Synthesis, Materials, Devices*, John Wiley & Sons, Inc., New York, **2015**.
- [219] Y. Marcus, *Chem. Rev.* **1988**, *88*, 1475–1498.
- [220] S. Xue, B. Garlyyev, S. Watzele, Y. Liang, J. Fichtner, M. D. Pohl, A. S. Bandarenka, *ChemElectroChem* **2018**, *5*, 2326–2329.
- [221] J. Tymoczko, V. Colic, A. Ganassin, W. Schuhmann, A. S. Bandarenka, *Catal. Today* **2015**, *244*, 96–102.
- [222] J. Resasco, L. D. Chen, E. Clark, C. Tsai, C. Hahn, T. F. Jaramillo, K. Chan, A. T. Bell, *J. Am. Chem. Soc.* **2017**, *139*, 11277–11287.
- [223] T. J. P. Hersbach, I. T. McCrum, D. Anastasiadou, R. Wever, F. Calle-Vallejo, M. T. M. Koper, *ACS Appl. Mater. Interfaces* **2018**, *10*, 39363–39379.

# List of Abbreviations

AC	alternating current
<i>ads</i>	adsorbate
CE	counter electrode
CV	cyclic voltammogram
DC	direct current
DFT	density functional theory
DTS	distance tunneling spectroscopy
ECSA	electrochemically active surface area
<i>fcc</i>	face centred cubic
HER	hydrogen evolution region
HOPG	highly oriented pyrolytic graphite
<i>in-situ</i>	‘in the reaction mixture’
IR	infrared spectroscopy
IRAS	infrared reflection absorption spectroscopy
LDOS	local density of states
MSE	mercury sulfate electrode
pH	power of hydrogen
PID	proportional integral derivative
$pK_a$	logarithmic acid dissociation constant
<i>pzc</i>	potential of zero charge
RE	reference electrode
SHE	standard hydrogen electrode
STM	scanning tunneling microscopy
TOC	total organic content
UHV	ultra-high vacuum
WE	working electrode



# List of Symbols

$c$	molar concentration
$^{\circ}\text{C}$	degree Celsius
$E$	electrode potential
$E_{vac}$	vacuum level
$E_F$	Fermi level
$I$	current
$I_T$	tunneling current
$j$	current density
$K$	Kelvin
$M$	molarity
$M\Omega\text{ cm}$	electrical resistivity
$Q$	charge
$q$	charge density
$U$	voltage
$U_B$	tunneling bias
$U_T$	tunneling voltage
$V$	volt
$\Phi$	work function
$\Phi_t$	tunneling barrier





# List of Figures

Figure 2.1: (a) Unit cell of with a face-centred-cubic ( <i>fcc</i> ) lattice. (b) Single-crystal model of an <i>fcc</i> (hkl) metal.....	6
Figure 2.2: Model of a single-crystal with an <i>fcc</i> lattice, based on <sup>[90]</sup> (a) highlighting the {111} plane. (b) Plane view of the {111} plane along with its base vectors. (c) STM image of a Au(111)-(1×1) unreconstructed surface.....	6
Figure 2.3: Schematic representation (left) <sup>[103]</sup> and <i>in-situ</i> STM image (right) of the Au(111)-( $\sqrt{3} \times 22$ ) surface reconstruction. ....	8
Figure 2.4: Structure of a crystal surface represented by Kossel's Model <sup>[114]</sup> and ( <i>in-situ</i> ) STM images of a Au(111) surface, displaying important surface morphologies and defects. ....	10
Figure 2.5: Model of the metal-electrolyte interface where the metal is positively charged. <sup>[123]</sup> .....	12
Figure 2.6: Triangular voltage of the limiting potentials ( $E_1$ and $E_2$ ) used for cyclic voltammetry.....	14
Figure 2.7: Model of a hexagonal <i>fcc</i> (111) substrate with different adsorbate structures, where a (2×2), a ( $\sqrt{3} \times \sqrt{3}$ ) <i>R</i> 30° and a ( $\sqrt{7} \times \sqrt{7}$ ) <i>R</i> 30° superstructure is represented in black, blue and pink, respectively. ....	17
Figure 2.8: Current-potential curve of a freshly prepared Au(111) electrode in 0.1 M H <sub>2</sub> SO <sub>4</sub> at 20 °C. Scan rate: 10 mV s <sup>-1</sup> . Also shown, is the measured potential <i>vs.</i> Pt pseudo-reference electrode (blue scale).....	19
Figure 2.9: <i>In-situ</i> STM images of Au(111) in 0.1 M H <sub>2</sub> SO <sub>4</sub> showing the Au(111) (a) ( $\sqrt{3} \times 22$ ) surface reconstruction at a potential close to the <i>pzc</i> : 30×30 nm <sup>2</sup> , $E = -0.1$ V,	

$U_T = 0.2$  V,  $I_T = 2$  nA, (b)  $(1 \times 1)$  surface after lifting of reconstruction, before phase transition:  $490 \times 490$  nm<sup>2</sup>,  $E = 0.60$  V,  $U_T = 0.4$  V,  $I_T = 2$  nA, where the inset is the height profile of a monoatomic high Au island, (c) adsorbed sulfate structure, positive of the phase transition peak:  $4.4 \times 4.4$  nm<sup>2</sup>,  $E = 0.85$  V,  $U_T = 0.5$  V,  $I_T = 2$  nA, and (d) model of the  $(\sqrt{3} \times \sqrt{7})R19.1^\circ$  structure of adsorbed  $\text{SO}_4^{2-}$  or  $\text{HSO}_4^-$  ions and, coadsorbed  $\text{H}_3\text{O}^+$  ions or  $\text{H}_2\text{O}$  molecule, on the Au(111) surface. ....20

Figure 2.10: Model for the bidentate and tridentate configuration of formate and acetate, and sulfate and phosphate, respectively, adsorbed on Au(111). Similar  $\text{p}K_a$  values for deprotonation of formic and acetic acid in solution suggest comparable adsorption strength for formate and acetate on Au(111). Difference in  $\text{p}K_a$  values for sulfate and phosphate, compared to formate, suggest possible competition during adsorption. ....23

Figure 2.11: Schematic representation of the energy relationships at the tunnel barrier between an STM tip and a sample<sup>[154]</sup>, based on<sup>[153]</sup> where  $s$ : distance between tip and sample,  $\Phi_{\text{tip}}$  and  $\Phi_{\text{sample}}$ : wave functions of tip or sample, respectively,  $\Phi_T$ : average tunnel barrier height and  $eU_T$ : energy difference between both corresponding Fermi levels. ....25

Figure 2.12: Functioning principle of scanning tunneling microscopy<sup>[154]</sup>, based on<sup>[156]</sup>. ....27

Figure 2.13: Schematic representation of the four-electrode arrangement of an *in-situ* STM<sup>[25]</sup> where RE: reference electrode, CE: counter electrode, WE: working electrode,  $U_T$ : tunneling voltage and  $I_T$ : tunneling current. ....28

Figure 3.1: Schematic representation of the flame annealing, using a butane blow torch, of an STM gold single-crystal. ....31

Figure 3.2: Schematic representation of a three-electrode glass electrochemical cell with the *hanging-meniscus* set up.<sup>[171]</sup> ....33

Figure 3.3: *In-situ* STM scanner head calibration in the x-/y- and z- directions by performing measurements with HOPG and Au(111) substrates in air, respectively. ....35

Figure 3.4: Schematic representation of an *in-situ* STM cell.<sup>[132]</sup> ....36

Figure 3.5: Schematic representation of the anodic etching apparatus of W tips.<sup>[103]</sup> ....38

Figure 3.6: Schematic representation of the electrochemical coating of the STM tips using an anodic electrophoretic paint.<sup>[103]</sup> ....39

Figure 4.1: Potential-step time series of the HER activity for Au(111) in 0.1 M  $\text{H}_2\text{SO}_4$  at -0.485 V. The *in-situ* STM images illustrate surface structures: (a) thermally reconstructed Au(111) surface recorded after flame-annealing upon immersion at -0.2 V,  $80 \times 80 \text{ nm}^2$  (b) Au(111)-(1 $\times$ 1) right after stepping to 0.415 V,  $75 \times 75 \text{ nm}^2$ , (c-e) potential-induced formation of the reconstructed surface after lifting the reconstruction and stepping back to -0.185 V,  $200 \times 200 \text{ nm}^2$ , and (f-h) 0.115 V,  $200 \times 200 \text{ nm}^2$ . Here, the HER is used to monitor structural changes of the Au(111) surface.<sup>[178]</sup> .....45

Figure 4.2: *In-situ* STM image of Au(111) in 0.1 M  $\text{H}_2\text{SO}_4$  showing the appearance of three distinct sulfate structures S-I, S-II and S-III:  $38 \times 38 \text{ nm}^2$ ,  $E = 0.85 \text{ V}$ ,  $U_T = 0.5 \text{ V}$ ,  $I_T = 3 \text{ nA}$ . .....46

Figure 4.3: *In-situ* STM images indicating three different sulfate structures for Au(111) in 0.1 M  $\text{H}_2\text{SO}_4$ :  $E = 0.80 \text{ V}$ ,  $U_T = 0.5 \text{ V}$ ,  $I_T = 3 \text{ nA}$ , where (a)  $6 \times 6 \text{ nm}^2$ , (b)  $5 \times 5 \text{ nm}^2$ , and (c)  $6 \times 6 \text{ nm}^2$ , represent structure S-I, S-II & S-III, respectively. The proposed models and the height profiles of key features in each structure and is represented alongside each STM image. ....49

Figure 5.1: Current-potential curve (black) of a Au(111) electrode in 0.2 M  $\text{CH}_3\text{COOH}$  at 20 °C. Scan rate:  $10 \text{ mV s}^{-1}$ .<sup>[52]</sup> Also shown is the measured potential *vs.* Pt pseudo-reference electrode (blue) and anodic charge density *vs.* potential curve (pink). The dashed (pink) line shows the estimation for double-layer charging. ....52

Figure 5.2: *in-situ* STM images of Au(111) in 0.2 M  $\text{CH}_3\text{COOH}$  showing the Au(111) (a) ( $\sqrt{3} \times 22$ ) surface reconstruction at potentials closer to the *pzc*:  $150 \times 150 \text{ nm}^2$ ,  $E = 0.15 \text{ V}$ ,  $U_T = 0.3 \text{ V}$ ,  $I_T = 2 \text{ nA}$ , (b) (1 $\times$ 1) surface after lifting of reconstruction, before phase transition:  $80 \times 80 \text{ nm}^2$ ,  $E = 0.85 \text{ V}$ ,  $U_T = 0.3 \text{ V}$ ,  $I_T = 2 \text{ nA}$ , (c) surface reconstruction after stepping back to a negative potential away from the *pzc*:  $100 \times 100 \text{ nm}^2$ ,  $E = -0.1 \text{ V}$ ,  $U_T = 0.2 \text{ V}$ ,  $I_T = 2 \text{ nA}$  and (d) initial formation of acetate structure positive of the phase transition peak:  $14 \times 14 \text{ nm}^2$ ,  $E = 0.95 \text{ V}$ ,  $U_T = 0.4 \text{ V}$ ,  $I_T = 2 \text{ nA}$ .<sup>[52]</sup> .....54

Figure 5.3: *in-situ* STM images of Au(111) in 0.2 M  $\text{CH}_3\text{COOH}$  showing the time dependence on the appearance of two different acetate structures A-I and A-II:  $30 \times 30 \text{ nm}^2$ ,  $E = 0.95 \text{ V}$ ,  $U_T = 0.6 \text{ V}$ ,  $I_T = 5 \text{ nA}$ . Structure A-II is highlighted in red. The scan direction is from top to bottom (a-d). The time specifications indicate completion of the individual STM images after stepping the potential to 0.95 V.<sup>[52]</sup> .....56

Figure 5.4: Plot of the coverage of structure A-I (blue symbols) and structure A-II (pink symbols) of acetate on the Au(111) terrace *vs.* time. The blue line represents an empirical fit with an exponential function whose exponent is a 2<sup>nd</sup> order polynomial. The sum of coverages of the blue and the pink lines give a total of 0.95, since around 5 % of the surface is covered with monoatomic high Au islands, on top of which no structure was imaged.<sup>[52]</sup> .....57

Figure 5.5: *in-situ* STM images of Au(111) in 0.2 M CH<sub>3</sub>COOH indicating (a) two distinct acetate structures, first (b) structure A-I: 2×2 nm<sup>2</sup>,  $E = 0.95$  V,  $U_T = 0.6$  V,  $I_T = 5$  nA, where (c) is the height profile of key features along the solid and the dotted lines in (b). Second, (d) structure A-II: 2×2 nm<sup>2</sup>,  $E = 0.95$  V,  $U_T = 0.6$  V,  $I_T = 5$  nA, where (e) is the height profile of key features along the solid and the dotted lines in (d).<sup>[52]</sup> .....58

Figure 5.6: Model for structures A-I and A-II of acetate on a Au(111) surface in 0.2 M CH<sub>3</sub>COOH. Structures A-I and A-II are represented by a  $(\sqrt{19} \times \sqrt{19})R23.4^\circ$  and a (2×2) arrangement of anions with respects to the underlying Au(111) surface, respectively. The structures are stabilized by coadsorbed H<sub>2</sub>O molecules.<sup>[52]</sup> .....61

Figure 5.7: Current-potential curve (black) of a Au(111) electrode in 0.2 M HCOOH + 0.1 M HClO<sub>4</sub> at 20 °C. Scan rate: 10 mV s<sup>-1</sup>. Also shown, is the measured potential *vs.* Pt pseudo-reference electrode (blue) and cathodic charge density *vs.* potential curve (pink). The dashed (pink) line corresponds to the estimated double-layer charge. ....63

Figure 5.8: (a-b) *in-situ* STM images of Au(111) in 0.2 M HCOOH, indicating the structure F-I of formate, first (a) 10×10 nm<sup>2</sup>,  $E = 0.95$  V,  $U_T = 0.65$  V,  $I_T = 8$  nA, where (b) is a crop out and 2D-FFT of (a), and (c) is the height profile of key features along the solid and the dotted lines in (a). (d) Model for structure F-I of adsorbed formate on Au(111) represented by a  $(3 \times 2\sqrt{3})$  arrangement of anions.....67

Figure 5.9: *in-situ* STM images of Au(111) in 0.2 M HCOOH + 0.1 M HClO<sub>4</sub> indicating two formate structures, first (a) negative of the phase transition, structure F-II: 86×86 nm<sup>2</sup>,  $E = 0.80$  V,  $U_T = 0.6$  V,  $I_T = 9$  nA, where (b) is a crop out and 2D-FFT of (a) and, (c) is the height profile of key features along the solid and the dotted lines in (b), and second (d) positive of the phase transition, structure F-III: 22×22 nm<sup>2</sup>,  $E = 0.95$  V,  $U_T = 0.65$  V,  $I_T = 3$  nA, where (e) is a crop out and 2D-FFT of (d) and, (f) is the height profile of key features along the solid and the dotted lines in (e). ....69

Figure 5.10: Model of structures F-II and F-III of adsorbed formate on a Au(111) surface in 0.2 M HCOOH + 0.1 M HClO <sub>4</sub> . Structures F-II and F-III are represented by a $(2\sqrt{7} \times 9)$ and a $(\sqrt{7} \times 3)$ arrangement of anions with respects to the underlying Au(111) surface, respectively. ....	70
Figure 6.1: Current-potential curves of a freshly prepared Au(111) electrode in 0.2 M sodium phosphate buffer solutions at pH 7.6, pH 9.0 and pH 11.5 at 20 °C. Scan rate: 10 mV s <sup>-1</sup> . ....	74
Figure 6.2: Current-potential curve (black) of a Au(111) electrode in in 0.185 M Na <sub>2</sub> HPO <sub>4</sub> + 0.015 M NaH <sub>2</sub> PO <sub>4</sub> at pH 7.6 and at 20 °C. Scan rate: 10 mV s <sup>-1</sup> . Also shown, is the measured potential <i>vs.</i> Pt pseudo-reference electrode (blue) and anodic charge density <i>vs.</i> potential curve (pink). The dashed (pink) line corresponds to the estimated double-layer charge. ....	75
Figure 6.3: (a) Current-potential curve of a Au(111) electrode in 0.185 M Na <sub>2</sub> HPO <sub>4</sub> + 0.015 M NaH <sub>2</sub> PO <sub>4</sub> at pH 7.6, displaying the U-shaped ‘pit’ in the positive-going scan. Scan rate: 10 mV s <sup>-1</sup> . (b-d) A series of 2D-FFT <i>in-situ</i> STM images of Au(111) showing ordered structures of adsorbed phosphate at different potentials within the so-called ‘pit’, where (b) $7 \times 7$ nm <sup>2</sup> , $E = 0.25$ V, $U_T = 0.1$ V, $I_T = 2.5$ nA and (c) $7 \times 7$ nm <sup>2</sup> , $E = 0.35$ V, $U_T = 0.2$ V, $I_T = 2$ nA and (d) $7 \times 7$ nm <sup>2</sup> , $E = 0.4$ V, $U_T = 0.23$ V, $I_T = 2$ nA. ....	77
Figure 6.4: (a) Current-potential curve of a Au(111) electrode in 0.185 M Na <sub>2</sub> HPO <sub>4</sub> + 0.015 M NaH <sub>2</sub> PO <sub>4</sub> at pH 7.6, displaying the U-shaped ‘pit’ in the positive-going scan. Scan rate: 10 mV s <sup>-1</sup> , in addition to the potential dependence on total $\theta_{\text{phosphate}}$ coverage and (b) on the phosphate-phosphate distances along ( $d_1$ ) and between ( $d_2$ ) the rows, as well as (c) on the measured enclosing angles ( $\alpha$ ) obtained from <i>in-situ</i> STM images. ....	78
Figure 6.5: (a) Current-potential curve of a Au(111) electrode in 0.185 M Na <sub>2</sub> HPO <sub>4</sub> + 0.015 M NaH <sub>2</sub> PO <sub>4</sub> at pH 7.6, displaying the second current spike attributed to a phase transition in the positive-going scan. Scan rate 10 mV s <sup>-1</sup> . (b-d) A series of <i>in-situ</i> STM images indicating ordered structures of adsorbed phosphate at different areas on the surface (white box) where, (b) $29 \times 29$ nm <sup>2</sup> , $E = 0.49$ V, $U_T = 0.32$ V, $I_T = 4$ nA. (c) $29 \times 29$ nm <sup>2</sup> , $E = 0.32$ V, $U_T = 0.15$ V, $I_T = 4$ nA. (d) $29 \times 29$ nm <sup>2</sup> , $E = 0.49$ V, $U_T = 0.32$ V, $I_T = 4$ nA. ....	82

Figure 6.6: *in-situ* STM images of Au(111) in 0.185 M Na<sub>2</sub>HPO<sub>4</sub> + 0.015 M NaH<sub>2</sub>PO<sub>4</sub> at pH 7.6 indicating ordered structures of adsorbed phosphate (a) on top of a monoatomic high Au island: 14×14 nm<sup>2</sup>,  $E = 0.48$  V,  $U_T = 0.24$  V,  $I_T = 2$  nA where (b) is a crop out and 2D-FFT of the *in-situ* STM image in (a): 3×3 nm<sup>2</sup>, and (c) at step edges: 10×10 nm<sup>2</sup>,  $E = 0.48$  V,  $U_T = 0.32$  V,  $I_T = 4$  nA where (d) is a crop out and 2D-FFT of the *in-situ* STM image in (c). .....83

Figure 6.7: Model for structures P-I and P-II of adsorbed phosphate on a Au(111) surface in 0.185 M Na<sub>2</sub>HPO<sub>4</sub> + 0.015 M NaH<sub>2</sub>PO<sub>4</sub> at pH 7.6. Structures P-I and P-II are represented by a  $(2\sqrt{3} \times \sqrt{7})$  and a  $(\sqrt{3} \times \sqrt{7})$  arrangement of anions with respects to the underlying Au(111) surface, respectively. The structures are stabilized by coadsorbed Na<sup>+</sup> ions. ....84

Figure 6.8: Current-potential curve for a Au(111) electrode in 0.04 M Na<sub>2</sub>HPO<sub>4</sub> + 0.16 M NaH<sub>2</sub>PO<sub>4</sub> at pH 7.3. Scan rate 10 mV s<sup>-1</sup>. A series of *in-situ* STM images representing ordered structures of adsorbed phosphate that are (a) on a terrace: 5×5 nm<sup>2</sup> (2D-FFT),  $E = 0.25$  V,  $U_T = -0.11$  V,  $I_T = 3$  nA, (b): 10×10 nm<sup>2</sup> (2D-FFT),  $E = 0.3$  V,  $U_T = -0.16$  V,  $I_T = 2.5$  nA, (c) on Au islands: 40×40 nm<sup>2</sup>,  $E = 0.46$  V,  $U_T = -0.19$  V,  $I_T = 4$  nA, where the inset is a zoom in of the structure: 4.45×4.45 nm<sup>2</sup>, and (d) is a 2D-FFT of the ‘zoom in’ in (c). .....86

Figure 6.9: Current-potential curve for a Au(111) electrode in 0.1 M H<sub>3</sub>PO<sub>4</sub> + 0.18 M LiOH at pH 7.3. Scan rate 10 mVs<sup>-1</sup>. Courtesy of Johannes. M. Hermann. A series of *in-situ* STM images of a Au(111) electrode in 0.1 M H<sub>3</sub>PO<sub>4</sub> + 0.18 M LiOH representing structures of adsorbed phosphate that are (a) ordered: 10×10 nm<sup>2</sup>,  $E = 0.34$  V,  $U_T = -0.11$  V,  $I_T = 2$  nA, (b) ordered: 20×20 nm<sup>2</sup>,  $E = 0.34$  V,  $U_T = -0.11$  V,  $I_T = 5$  nA. (c) semi-ordered: 19×19 nm<sup>2</sup>,  $E = 0.59$  V,  $U_T = 0.26$  V,  $I_T = 7$  nA (Scan angle: 30°), (d) semi-ordered: 20×20 nm<sup>2</sup>,  $E = 0.48$  V,  $U_T = 0.15$  V,  $I_T = 7$  nA. ....89

# List of Tables

Table 3.1: List of the used chemicals. ....	40
Table 3.2: List of the used materials. ....	41
Table 4.1: Averaged sulfate-sulfate distances along ( $d_1$ ) and between ( $d_2$ ) the rows, as well as the measured enclosing angles ( $\alpha$ ) and total $\theta_{\text{sulfate}}$ coverages obtained from <i>in-situ</i> STM images of a Au(111) electrode in 0.1 M H <sub>2</sub> SO <sub>4</sub> of structures S-I, S-II and S-III of adsorbed sulfate. ....	48
Table 6.1: Averaged phosphate-phosphate distances along ( $d_1$ ) and between ( $d_2$ ) the rows, as well as the measured enclosing angles ( $\alpha$ ) and total $\theta_{\text{phosphate}}$ coverages obtained from <i>in-situ</i> STM images of a Au(111) electrode in 0.185 M Na <sub>2</sub> HPO <sub>4</sub> + 0.015 M NaH <sub>2</sub> PO <sub>4</sub> at pH 7.6 of structure P-I of adsorbed phosphate at different potentials. ....	79
Table 6.2: Averaged phosphate-phosphate distances along ( $d_1$ ) and between ( $d_2$ ) the rows, as well as the measured enclosing angles ( $\alpha$ ) and total $\theta_{\text{phosphate}}$ coverages obtained from <i>in-situ</i> STM images of a Au(111) electrode in 0.04 M Na <sub>2</sub> HPO <sub>4</sub> + 0.16 M NaH <sub>2</sub> PO <sub>4</sub> at pH 7.3 of structures P-I and P-II of adsorbed phosphate at different potentials. ....	85





## Publications

- [1] A. Abdelrahman, J. M. Hermann, T. Jacob, L. A. Kibler, First High Resolution *in-situ* STM Study of the Adsorption of Formate on Gold, (*in preparation*).
- [2] J. M. Hermann, A. Abdelrahman, T. Jacob, L. A. Kibler, Probing Structural Changes by HER - Kinetics of the Reconstruction of an Au(111) electrode surface, *Electrochim. Acta.* **2019**, (*to be submitted*).
- [3] A. V. Rudnev, M. R. Ehrenburg, E. B. Molodkina, A. Abdelrahman, M. Arenz, P. Broekmann, T. Jacob, Structural changes of Au(111) single crystal electrode surface in ionic liquids, *ChemElectroChem* **2019** (*submitted*).
- [4] A. Abdelrahman, J. M. Hermann, T. Jacob, L. A. Kibler, Adsorption of Acetate on Au(111): An *in-situ* STM Study and Implications on Formic Acid Electrooxidation, *ChemPhysChem* **2019**, *20*, 1-9.
- [5] L. A. Kibler, J. M. Hermann, A. Abdelrahman, A. A. El-Aziz, T. Jacob, New insights on hydrogen evolution at Au single-crystal electrodes, *Curr. Opin. Electrochem.* **2018**, *9*, 265–270.
- [6] A. Abdelrahman, J. M. Hermann, L. A. Kibler, Electrocatalytic Oxidation of Formate and Formic Acid on Platinum and Gold: Study of pH Dependence with Phosphate Buffers, *Electrocatalysis* **2017**, *8*, 509–517.



# Curriculum Vitae

---

## Personal Information

Name	Areeg Abdelrahman
Address	Ulm
Year of Birth	1990
Place of Birth	Saudi Arabia

---

## Education & Academic Experience

11/2018 – Today	Group Leader of <i>in-situ</i> Surface Characterization Techniques Institute of Electrochemistry, Ulm University   89081 Ulm
10/2014 – 12/2019	PhD Candidate Institute of Electrochemistry, Ulm University   89081 Ulm
05/2014	M.Sc. in Engineering and Material Science German University in Cairo (GUC)   Cairo, Egypt <ul style="list-style-type: none"><li>▪ Thesis Title: ‘Dependence of pH on the Electrocatalytic Oxidation of Formic Acid on Platinum and Gold Electrodes’</li><li>▪ Thesis GPA : 1.3 (Excellent)</li><li>▪ Cumulative GPA: 1.2 (Excellent with Highest Honors)</li></ul>
08/2013 – 09/2014	Research Assistant/Master’s Thesis Student in Electrochemistry Institute of Electrochemistry, Ulm University   89081 Ulm
08/2012 – 07/2013	Teaching Assistant in ‘Engineering and Material Science’ German University in Cairo (GUC)   Cairo, Egypt

- 07/2012                      B.Sc. in Engineering and Material Science  
German University in Cairo (GUC) | Cairo, Egypt
- Thesis Title: ‘Evaluation of Austenitic Stainless Steel for High Temperature Components’
  - Thesis GPA : 0.7 (Excellent)
  - Cumulative GPA: 1.65 (Very Good with Honors)
- 09/2011 – 01/2012      Junior Teaching Assistant in ‘Engineering and Material Science’  
German University in Cairo (GUC) | Cairo, Egypt
- 03/2011 – 08/2011      Internship/Bachelor’s Thesis Student in ‘Lifetime Concepts, Thermomechanics’  
Fraunhofer Institute of Mechanics of Materials IWM | 79108 Freiburg im Breisgau
- 07/2007                      High School Degree  
American Diploma from College Board USA | Riyadh, Saudi Arabia
- SAT I Grade: 1420/1600
  - SAT II Grade: 1400/1600
  - American Cumulative GPA: 4.0 (Excellent)

